ROLES OF SURFACE INTERACTION ON CRYPTOSPORIDIUM PARVUM OOCYST TRANSPORT IN SUBSURFACE ENVIRONMENT

BY

YUANYUAN LIU

DISSERTATION

Submitted in partial fulfillment of the requirements
for the degree of Doctor of Philosophy in Environmental Engineering in Civil Engineering
in the Graduate College of the
University of Illinois at Urbana-Champaign, 2012

Urbana, Illinois

Doctoral Committee:

Assistant Professor Thanh H. Nguyen, Chair, Director of Research
Professor Charles J. Werth
Professor Benito J. Mariñas
Associate Professor Aaron I. Packman, Northwestern University

ABSTRACT

The influence of *Cryptosporidium* (*C.*) *parvum* oocyst and collector surface properties on transport of *C. parvum* oocysts and microspheres was studied with a radial stagnation point flow (RSPF) cell and 2-dimensional (2-D) micromodels. The quartz or natural organic matter coated quartz surfaces were used as collector in the RSPF cell. The cylindrical silica collectors or silica collectors coated with 0, 10, 20, 50 and, 100% Fe_2O_3 patches were firstly fabricated in micromodels. Real time transport of oocyst in RSPF cell and micromodel in electrolyte solutions with systematically varied composition was monitored. Surface polarity and chemical heterogeneity of oocysts surface were characterized by liquid chromatography/nanoelectrospray ionization tandem mass spectrometry (LC-MS/MS), microbial adhesion to hydrocarbon test (MATH), contact angle, and Fourier transform Infrared Spectroscopic (FT-IR) imaging.

The most important fundings of this research are the followings: 1) this research developed a method to precisely design complicated yet well-controlled collector properties of porous media and showed the importance of spatial distribution of charged heterogeneous patches on collectors; 2) the results illustrated that the composition and conformation of oocyst surface macromolecules determined oocyst transport by controlling the surface interactions and complexations between oocyst and quartz, NOM, Fe_2O_3 and charged heterogeneous mineral surfaces. Especially, this research firstly revealed that the electrophoretic softness of oocyst surface macromolecules was essential to van der Waals interaction and steric repulsion between oocyst and quartz surfaces.

RSPF experiments illustrated that steric repulsion caused by oocyst surface macromolecules prevented oocyst deposition at higher ionic strength where the Derjaguin–Landau–Verwey–Overbeek (DLVO) theory predicted maximum deposition. Charge heterogeneity was responsible for oocyst deposition on natural organic matter (NOM) surfaces and at lower ionic strength where the DLVO theory predicted zero deposition. To study the role of oocyst surface macromolecules, deposition of untreated oocysts and oocysts modified by proteinase K in RSPF cell were compared. The proteinase K modification resulted in 10 times higher electrophoretic softness and 100 times lower van der Waals interaction of proteinase K modified oocysts than untreated oocysts. Though oocysts modified by proteinase K were less negatively charged, the change of composition and conformation of oocyst surface macromolecules led to significantly low deposition rate compared to that of untreated oocysts.

The results indicated that oocyst surface macromolecules determined oocyst deposition mechanisms by controlling van der Waals interaction and steric repulsion. In addition, oocysts were directly observed to be entrapped in the DLVO secondary minimum energy well. The results illustrated that attachment in secondary minimum energy well was reversible and oocysts were either resuspended due to hydrodynamic forces or transferred to more stable primary minimum energy well.

Distribution of oocyst attachment on collectors within a micromodel was correlated with local flow rate. Only a small portion of oocysts attached on collectors in micromodels were released when pumping in oocysts free electrolyte solution with low ionic strength. The results confirmed the previous observation that oocysts entrapped in secondary minimum energy well would either be transferred to primary minimum energy well or be resuspended. Significant numbers of attached oocysts were released when pumping in oocysts free electrolyte solution with pH 11. Since positively charged functional groups will be deprotonated at pH 11, the release of oocysts was contributed to surface charge heterogeneity. An attempt to characterize oocyst surface chemical heterogeneity was made using FT-IR imaging. FT-IR spectra varied with location on a layer of oocysts. Though the resolution of this technique is not high enough to quantify oocyst surface chemical heterogeneity so far, great efforts are made to improve its resolution. Recently, the resolution of FT-IR imaging is improved from 1.6 μm to 1.0 μm. Therefore, FT-IR imaging is promising in characterizing surface chemical heterogeneity. Each silica collector in the micromodel was periodically coated with Fe_2O_3 patches to create charged heterogeneous collectors. Oocyst average single collector removal efficiency (η) on Fe_2O_3 patches was 2-3 times higher than on collector coated with 100% Fe_2O_3, which implied the importance of periodic electrostatic interactions caused by alternating charged heterogeneous patches. In addition, oocyst attached more on Fe_2O_3 surface at pH 8.1, where DLVO predicted energy barrier, than at pH 5.8, where DLVO predicted no energy barrier. This indicated different complexations formed between oocyst carboxylate groups and Fe metal centers on Fe_2O_3 surfaces at different pH conditions.

ACKNOWLEDGMENTS

I would like to sincerely express my gratitude to my advisor, Dr. Thanh H. (Helen) Nguyen, for her dedicated mentoring, valuable advices, constant support, and immense patience during my Ph.D. study. I especially want to thank her for her guidance over the years and the opportunities and resources she provided me to explore the new technologies and unknown territories. I appreciate Dr. Mark S. Kuhlenschmidt and Theresa K Kuhlenschmidt for providing me perspectives on knowledge of microbiology and Dr. Changyong Zhang for showing me a broad scope of microscopic techniques to enrich my study. I also thank them for helpful advice on being a professional and all that they have done for me during the past five years. I would like to thank the committee members, Dr. Charlie J. Werth and Dr. Benito J. Mariñas, for their insights and inputs in the field of transport. It is my great pleasure and privilege to communicate with them in both research and classes. I am very grateful to Dr. Aaron I. Packman for his dedication to serving on my committee, for his insightful comments and suggestions, and for his scientific and critical thinking that helped me improving this dissertation.

I acknowledge National Science Foundation (NSF), The Center of Advanced Materials for the Purification of Water with Systems under the National Science Foundation (Water CAMPWS), NSF Career Grant, Illinois Water Resources Center (IWRS), and Environmental Molecular Sciences Laboratory (EMSL) sponsored by the DOE, Office of Biological and Environmental Research and located at PNNL. Never enough thank you for Nugyen group members: Ian Bradley, Qinwei Chow, Shengkun Dong, Nickolas Easter, Heather E. Goetsch, Jayanthi Gopal, Leonardo Gutierrez, Dao Janjaroen, Ruiqing Lu, Nanxi Lv, Mai Pham, Ofelia C. Remoro, Sahid Rosado, Yun Shen, Anthony P. Staub, Annia Vargas, Hanting Wang, Chia-Cheng Wei, and Baoling Yuan. I will forever cherish the time that we spend together in the lab as well as celebrating each achievements. I greatly thank Rohit Bhargava, Markus Hilpert, Dehong Hu, Rong Kang, Jinyong Liu, Steven E. Mylon, and Peter Yau for many helpful discussions in the research. I want to express my deep gratitude to Dr. Vern L. and Jeannie M. Snoeyink, who have always been there to share with me great wisdom and pleasure. I appreciate Dr. Shaoying Qi, our lab manager, for his dutifully maintenance of the lab. I thank all the fellows in the Department of Civil and Environmental Engineering who made my study here a wonderful experience. I thank all my friends who shared my life, my hobbies and encouraging me moving

forward. I want to especially thank all, whom I could not name here, who patiently helped me whenever I needed, and who shared with me their precious time.

Finally, I give my deepest gratitude to my parents, Qiangjia Liu and Guangzu Yuan, my boyfriend, Xiaohang Sun, and my families for their love, understanding and supports. I could not have made this without them.

TABLE OF CONTENTS

CHAPTER 1

INTRODUCTION

1.1 Background

Cryptosporidium (*C.*) is a protozoan pathogen capable of infecting a wide range of mammals. Some species infect humans. An infected animal or human suffers from cryptosporidiosis, a severe diarrheal disease, which lasts 1 to 2 weeks for immunocompetent individuals, but could be fatal for infants and immunosuppressed people since there is no effective therapy. *C.* oocysts, the resistant stage of this pathogen, were found in surface water, ground water, soil, livestock, fish, amphibians, reptiles, birds, zoo and wild mammals, and food production. Outbreaks of cryptosporidiosis occur throughout the year.[1] More than 1000 reports of human cryptosporidiosis over almost 100 countries have been documented since 1976, the first documented human cryptosporidiosis.[2]

C. oocysts in surface and ground water are one of the leading causes of impaired drinking water sources and have been a serious public health concern.[3-5] The occurrence of *Cryptosporidium* in surface water was reported from 39% to 100% positive in large scale investigations.[6-8] In a groundwater survey, 11% of 463 samples from 23 states were *Cryptosporidium* positive.[9] *Cryptosporidium* was detected in 15% and 26.8% of treated drinking water samples from two studies which examined 82 and 100 water treatment plants.[10, 11] *Cryptosporidium* level varied from 0.001 to 484 oocysts/L in surface water,[6-8] 0.003 to 45 oocysts/L in groundwater [6, 9] and 0.001 to 0.8 oocysts/L in treated drinking water.[10, 11]

Micrometer size *C.* oocysts are very resistant to traditional disinfection processes, such as chlorine-based disinfection,[12, 13] but can be effectively removed by granular filtration.[14] US EPA (Environmental Protection Agency) requires TT (treatment technique) of disinfection and filtration, and MCLG (maximum contaminate level goal) of zero for *C.* oocysts. Thus, unfiltered systems are required to include *C.* oocysts in the watershed control provisions. However, the identification of *C.* oocysts in environmental samples is expensive, time consuming and expertise

demanding. As shown in the previous paragraph, due to the methods and expertise of analysts, the recorded occurrence and levels of *Cryptosporidium* in raw and treated drinking water in United States varied significantly.[2] Therefore, it is of great interests to assessment *C.* oocysts transport and fate in both natural watershed and engineered filtration system. Great efforts have been put in the last two decades to study *C.* oocysts transport.

Though there are many species in *Cryptosporidium* genus, *C. parvum* is most used in lab investigation for many reasons.[2] First of all, *C. parvum* is capable of infecting a wide range of mammals including human. In 1993, 400,000 individuals were infected with *C. parvum* in Milwaukee, WI. More than 50 deaths among persons with AIDS were associated to Milwaukee's cryptosporidiosis outbreak in the next two years.[15] Corso et al.[3] estimated that the 1993 outbreak in Milwaukee caused the loss of $31.6 million in medical care costs and $46.5 million in productivity loss. Even though the contamination sources have never been identified conclusively, this outbreak was associated with the failure of a filtration system at a Milwaukee water treatment plant due to unusually high spring run-off.[11, 16] Secondly, routine in vivo propagation of *C. parvum* in neonatal livestock is well established. Thus, most of the studies choose *C. parvum* as model pathogen. In addition, polystyrene microspheres,[17, 18] algae[19], spores[20] and inactivated oocysts[21] were used as surrogates for viable *C. parvum* oocysts to study *C. parvum* oocyst transport. Microspheres generally were more mobile than *C. parvum* oocysts.[22]

Attachment and transport of *C. parvum* oocysts have been studied at different scales ranging from atomic force microscopy (AFM),[23-26] to radial stagnation point flow (RSPF) cell,[14, 27-29] to single layer packed glass beads,[30] to laboratory packed sand/glass beads column,[22, 23, 31-54] to laboratory flume,[55] and to field study.[17-19, 56-58] In all these studies, the influence of ionic strength, pH, [34, 36, 52] Ca^{2+},[29] oocyst surface protein,[27, 28] natural organic matter or biofilm,[37] surface charge heterogeneity,[52] suspended particles,[35, 55] porous media microspore,[49, 56] flow rate, [40, 49, 59] and straining[36, 40, 49, 60] on *C. parvum* oocyst attachment and transport was intensively studied. In brief, low ionic strength, high pH, larger porous media microspore, and high flow rate enhances *C. parvum* oocyst mobility. The presence of Ca^{2+}, oocyst surface protein, natural organic matter or biofilm, surface charge heterogeneity, suspended particle, and straining resulted in *C. parvum* oocyst attachment. Electrostatic interaction, van der Waals interactions, steric repulsion and cation bridging in the presence of Ca^{2+} were identified as the predominate mechanisms governing *C. parvum* oocyst behavior under those conditions.[14, 23, 27-29, 61] Note that

electrostatic interaction and van der Waals interaction are able to be quantified and included in Derjaguin–Landau–Verwey–Overbeek (DLVO) theory, which is often used to interpret colloid-colloid and colloid-collector surface interactions.[14, 62]

Even though the studies mentioned above shed light on *C. parvum* oocyst attachment and transport, mathematical models to predict *C.* oocysts transport in granular porous media are insufficient due to lack of thoroughly understanding of *C.* oocysts transport mechanisms. For example, many studies showed that *C. parvum* oocysts from different sources had different attachment rate in RSPF experiments. This indicated the importance of surface properties in *C. parvum* oocyst transport.[14, 27, 28] A few studies have made great effort to relate *C. parvum* oocyst and collector surface properties to *C. parvum* oocyst transport mechanisms.[27-29, 52] Nevertheless, the relationship between surface properties, *C. parvum* oocyst-collector interactions and transport mechanisms was not fully understood and need to be investigated. For example, it was suggested that oocyst surface protein prevented oocyst attachment by increasing steric repulsion.[27] However, oocyst surface macromolecule could also influence other oocyst-collector interactions such as van der Waals interactions. Though, both colloid and collector surface charge heterogeneities was thought to be responsible for higher colloid attachment. There is no effective technique to characterize colloid surface charge heterogeneity and the patchwise geochemical charged heterogeneous model doesn't fit well with the experimental data.[52]

1.2 Objectives

The overall objective of this research was to relate oocyst and collector surface properties to oocyst-collector interactions, and to elucidate the influence of oocyst-collector interactions on oocyst transport. Specifically, this research focused on the influence of surface potential, electrophoretic softness, surface polarity as well as charge heterogeneity on oocyst-collector interaction and oocyst transport mechanisms. This knowledge can provide insight to water safety risk assessment, removal of microorganism with filtration, and developing mathematical transport model. In addition, this research aimed to develop a micromodel that can manipulate collector properties and conduct real time observation of colloid transport. The specific objectives of the following chapters are:

1. To determine the attachment mechanisms of oocyst on quartz and NOM surfaces in a RSPF cell and identify the major factors that made oocyst deposition deviate from DLVO theory.
2. To understand the effect of oocyst surface properties on oocyst-collector interaction and attachment mechanisms. Oocyst surface macromolecules released by proteinase digestion was characterized and surface properties (such as oocyst surface potential, electrophoretic softness and surface polarity) of untreated and proteinases modified oocysts were investigated, and those properties were related to oocyst-collector interaction and attachment mechanisms.
3. To conduct real time observation of oocyst attachment and detachment on collectors in a 2-dimensional micromodel. Oocyst attachment was studied from clean collectors until collectors are ripened. Detachment of oocysts at lower ionic strength or higher pH after attachment experiments was investigated to study the influence of secondary minimum energy well and oocyst surface charge heterogeneity on oocyst transport.
4. To understand the influence of collector surface charge heterogeneity on oocyst attachment mechanisms using patchwise charged heterogeneous micromodels developed by partially coating silica collectors with Fe_2O_3 patches.

1.3 Experimental Approach

A multiscale study, including a radial stagnation point flow (RSPF) cell and a 2-dimensional (2-D) microscopic pore structure micromodel, was conducted to investigate the role of oocyst and collector surface properties on oocyst transport mechanisms on inorganic and organic surfaces of granular porous media. Both RSPF cell and micromodel provide real time observation of oocyst transport (Figure 1.1). On one hand, RSPF cell allows systematic and cost effective study of oocyst-collector interactions under well-defined hydrodynamic conditions near the collector forward stagnation point. On the other hand, micromodel allows flexible and well-controlled design of porous media in a multi-collector pore network. The hydrodynamic condition of RSPF cell and micromodel was analyzed in Chapter 2 and 4, respectively.

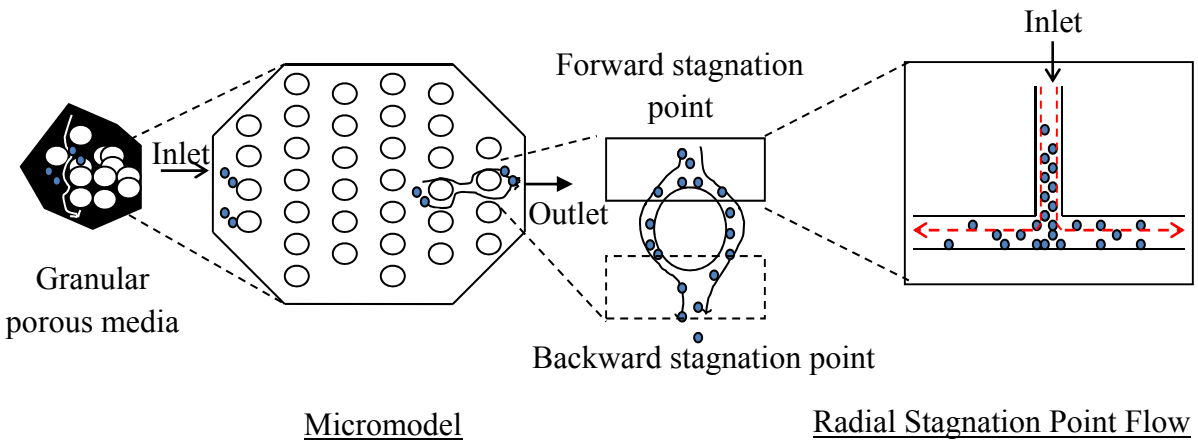

Figure 1.1 Multiscale experimental techniques used in this study

Viable *C. parvum* oocysts isolated from infected male Holstein calves were used in attachment and transport experiments. Some of the results were compared to transport of synthesized microspheres in the same experimental conditions to investigate the attachment mechanisms. Pepsin, proteinase K, and mixed glycosidases were used to modify oocyst surface macromolecules to investigate the composition and conformation of oocyst surface macromolecules and their role in oocyst-quartz interactions.

The collector surface used in this research included quartz, silica, Fe_2O_3, NOM, poly-L-lysine (PLL) and silica/Fe_2O_3 charged heterogeneous surfaces. Experiments were conducted in a range of monovalent ion electrolytes at different pH, from pH 2.5 to 8.0, for different purposes.

1.4 Dissertation Organization

In Chapter 2, titled "Deposition of *Cryptosporidium parvum* Oocysts on Natural Organic Matter Surfaces: Microscopic Evidence for Secondary Minimum Deposition in a Radial Stagnation Point Flow Cell", 1) the hydrodynamic condition of RSPF cell was analyzed, 2) the surface electrophoretic properties of oocysts, carboxylate modified latex (CML) particles, quartz, NOM and PLL surfaces were characterized with Ohshima's theory, and 3) the deposition of oocysts and CML particles on quartz or NOM surfaces were systematically compared to study oocyst attachment mechanisms and identify the major factors that made oocyst deposition deviated from DLVO theory.

The results indicated that oocysts and NOM surfaces had a layer of ion-penetrable surface polyelectrolytes which consisted charged polymer segments exerting frictional forces on the liquid flowing in the polyelectrolyte layer. This "soft" layer prevented oocyst deposition at high ionic strength where no DLVO energy barrier existed.

The electrostatic interaction and van der Walls interaction controlled oocyst deposition at different ionic strength. Deposition at low ionic strength, where DLVO energy barrier existed, was contributed to oocyst surface charge heterogeneity. In addition, microscopic evidence for oocyst entrapped in DLVO secondary minimum at 10 mM ionic strength was observed.

In Chapter 3, titled "Composition and Conformation of *Cryptosporidium parvum* Oocyst Wall Surface Macromolecules and Their Effect on Adhesion Kinetics of Oocysts on Quartz Surface", the "soft" ion-penetrable surface polyelectrolytes layer we characterized in Chapter 2 was intensively studied. 1) Peptides and carbohydrates released from oocyst surface by proteinase digestion were analyzed, 2) electrophoretic softness of untreated and proteinases modified oocysts were studied to reveal the conformation of the "soft" ion-penetrable surface polyelectrolytes layer, 3) Hamaker constants of untreated and proteinase K modified oocysts were calculated from contact angle to investigate the influence of surface macromolecules on oocyst-collector van der Waals interactions, and 4) deposition of untreated, pepsin modified, proteinase K modified, and mixed glycosidases modified oocysts on quartz surface in RSPF cell were compared to reveal the role of surface macromolecules on oocyst deposition.

The results indicated that the composition and conformation of oocyst surface macromolecules determined the electrophoretic properties, i.e. surface potential and electrophoretic softness, of the "soft" layer. In addition, the composition and conformation of surface macromolecules was critical for van der Waals interaction between oocyst and quartz surface. With proteinase K modification, oocyst surface electrophoretic softness increased 10 times and van der Waals interaction between oocyst and quartz surface decreased 100 times. This change of surface properties made oocyst barely deposited on quartz surface under the ionic strength we studied, i.e. 3 mM to 200 mM NaCl.

In Chapter 4, titled "Transport of *Cryptosporidium parvum* Oocysts in a Silicon Micromodel", we developed a method to conduct real time observation of oocyst transport in 2-D porous media of a micromodel. Hydrodynamic condition in micromodel was simulated and local flow velocity was related to oocyst attachment on local collectors. The attachment of

oocysts on single collector was studied from the clean bed until the collector was ripened. Detachment of oocysts at lower ionic strength or higher pH after attachment experiments showed that particles entrapment in secondary minimum was not stable and charge heterogeneity was important for oocyst attachment. oocyst attachment efficiencies measured with micromodel and RSPF cell were compared. The results illustrated that micromodel could be a powerful tool to study colloids transport.

In Chapter 5, titled "Role of Collector Alternating Charged Patches on Transport of *Cryptosporidium parvum* Oocysts in a Micromodel", a technique that was capable of precisely coating silica collector with alternating Fe_2O_3 patches in a micromodel was developed and the influence of collector charge heterogeneity on oocyst transport was studied. Fourier transform Infrared Spectroscopic (FT-IR) imaging indicated a degree of oocyst surface chemical heterogeneity. However, the resolution was not high enough to quantify oocyst surface heterogeneity. Therefore, the influence of collector charge heterogeneity on oocyst transport was studied instead. The results indicated a unique effect of periodic electrostatic interactions caused by alternating charged heterogeneous patches and showed the importance of surface complexations between oocyst and Fe_2O_3 surfaces.

The main finding and contribution of this research are summarized in the last chapter, Chapter 6. The work in Chapter 2, 3 and 4 have been published and the recent work in Chapter 5 will be submitted to Environmental Science & Technology later. The published papers were listed below:

1. Liu, Y.; Janjaroen, D.; Kuhlenschmidt, M. S.; Kuhlenschmidt, T. B.; Nguyen, T. H. Deposition of *Cryptosporidium parvum* Oocysts on Natural Organic Matter Surfaces: Microscopic Evidence for Secondary Minimum Deposition in a Radial Stagnation Point Flow Cell, *Langmuir*, 25, 1594-1605.
2. Liu, Y.; Kuhlenschmidt, M. S.; Kuhlenschmidt, T. B.; Nguyen, T. H. Composition and Conformation of *Cryptosporidium parvum* Oocyst Wall Surface Macromolecules and Their Effect on Adhesion Kinetics of Oocysts on Quartz Surface, *Biomacromolecules*, 11, 2109-2115.
3. Liu, Y.; Zhang, C.; Hilpert, M.; Kuhlenschmidt, M. S.; Kuhlenschmidt, T. B.; Nguyen, T. H. Transport of *Cryptosporidium parvum* Oocysts in a Silicon Micromodel, *Environmental Science & Technology*, 46, 1471-1479.

1.5 References

1. Hlavsa, M. C.; Watson, J. C.; Beach, M. J. Cryptosporidiosis surveillance --- United States 1999--2002. *Morbility and mortality weekly report* **2005,** *54* (SS01), 1-8.

2. Fayer, R.; Xiao, L., *Cryptosporidium and Cryptosporidiosis. , .* 2nd ed.; CRC Press, New York: 2007.

3. Corso, P. S.; Kramer, M. H.; Blair, K. A.; Addiss, D. G.; Davis, J. P.; Haddix, A. C. Cost of illness in the 1993 waterborne *Cryptosporidium* outbreak, Milwaukee, Wisconsin. *Emerging Infectious Diseases* **2003,** *9* (4), 426-431.

4. Fong, T. T.; Mansfield, L. S.; Wilson, D. L.; Schwab, D. J.; Molloy, S. L.; Rose, J. B. Massive microbiological groundwater contamination associated with a waterborne outbreak in Lake Erie, South Bass Island, Ohio. *Environmental Health Perspectives* **2007,** *115* (6), 856-864.

5. Gallay, A.; De Valk, H.; Cournot, M.; Ladeuil, B.; Hemery, C.; Castor, C.; Bon, F.; Megraud, F.; Le Cann, P.; Desenclos, J. C. A large multi-pathogen waterborne community outbreak linked to faecal contamination of a groundwater system, France, 2000. *Clinical Microbiology and Infection* **2006,** *12* (6), 561-570.

6. Rose, J. B.; Gerba, C. P.; Jakubowski, W. Survey of potable water supplies for *Cryptosporidium* and *Giardia*. *Environmental Science & Technology* **1991,** *25* (8), 1393-1400.

7. LeChevallier, M. W.; Norton, W. D.; Lee, R. G., Occurrence of *Giardia* and *Cryptosporidium* spp. in surface water supplies. In 1991; Vol. 57, pp 2610-2616.

8. LeChevallier, M. W.; Norton, W. D.; Siegel, J. E.; Abbaszadegan, M., Evaluation of the immunofluorescence procedure for detection of *Giardia* cysts and *Cryptosporidium* oocysts in water. In 1995; Vol. 61, pp 690-697.

9. Hancock, C. M.; Rose, J. B.; Callahan, M. Crypto and *Giardia* in U.S. groundwater. *Journal of the American Water Works Association* **1998,** *90*, 58-61.

10. LeChevallier, M. W.; Norton, W. D.; Lee, R. G., *Giardia* and *Cryptosporidium* spp. in filtered drinking water supplies. In 1991; Vol. 57, pp 2617-2621.

11. Mackenzie, W. R.; Schell, W. L.; Blair, K. A.; Addiss, D. G.; Peterson, D. E.; Hoxie, N. J.; Kazmierczak, J. J.; Davis, J. P. Massive outbreak of waterborne *Cryptosporidium* infection in Milwaukee, Wisconsin - Recurrence of illness and risk of secondary transmission. *Clinical Infectious Diseases* **1995,** *21* (1), 57-62.

12. Carey, C. M.; Lee, H.; Trevors, J. T. Biology, persistence and detection of *Cryptosporidium parvum* and *Cryptosporidium hominis* oocyst. *Water Research* **2004,** *38* (4), 818-862.

13. Rose, J. B.; Huffman, D. E.; Gennaccaro, A. Risk and control of waterborne cryptosporidiosis. *Fems Microbiology Reviews* **2002,** *26* (2), 113-123.

14. Kuznar, Z. A.; Elimelech, M. Adhesion kinetics of viable *Cryptosporidium parvum* oocysts to quartz surfaces. *Environmental Science & Technology* **2004,** *38* (24), 6839-6845.

15. Hoxie, N. J.; Davis, J. P.; Vergeront, J. M.; Nashold, R. D.; Blair, K. A. Cryptosporidiosis-associated mortality following a massive waterborne outbreak in Milwaukee, Wisconsin. *American Journal of Public Health* **1997,** *87* (12), 2032-2035.

16. Fox, K. R.; Lytle, D. A. Milwaukee's crypto outbreak: Investigation and recommendations. *Journal of the American Water Works Association* **1996,** *88* (9), 87-94.

17. Emelko, M. B.; Huck, P. M. Microspheres as surrogates for *Cryptosporidium* filatration. *Journal of the American Water Works Association* **2004,** *96* (3), 94-105.

18. Amburgey, J. E.; Amirtharajah, A.; York, M. T.; Brouckaert, B. M.; Spivey, N. C.; Arrowood, M. J. Comparision of conventional and biological filter performance for *Cryptosporidium* and microsphere removal. *Journal of the American Water Works Association* **2005,** *97* (12), 77-91.

19. Akiba, M.; Kunikane, S.; Kim, H. N.; Kitazawa, H. Algae as surrogate indices for the removal of *Cryptosporidium* oocysts by direct filtration. *Water Science and Technology* **2002,** *2* (3), 73-80.

20. Rice, E. W.; Fox, K. R.; Miltner, R. J.; Lytle, D. A.; Johnson, C. H. Evaluating plant performance with endospores. *Journal of the American Water Works Association* **1996,** *88* (9), 122-130.

21. Swertfeger, J.; Metz, D. H.; Demarco, J.; Braghetta, A.; Jacangelo, J. G. Effect of filter meida on cyst and oocyst removal. *Journal of the American Water Works Association* **1999,** *91* (9), 90-100.

22. Dai, X. J.; Hozalski, R. M. Evaluation of microspheres as surrogates for *Cryptosporidium parvum* oocysts in filtration experiments. *Environmental Science & Technology* **2003,** *37* (5), 1037-1042.

23. Byrd, T. L.; Walz, J. Y. Interaction force profiles between *Cryptosporidium parvum* oocysts and silica surfaces. *Environmental Science & Technology* **2005,** *39* (24), 9574-9582.
24. Considine, R. F.; Dixon, D. R.; Drummond, C. J. Laterally-resolved force microscopy of biological microspheres-oocysts of *Cryptosporidium parvum*. *Langmuir* **2000,** *16* (3), 1323-1330.
25. Considine, R. F.; Dixon, D. R.; Drummond, C. J. Oocysts of *Cryptosporidium parvum* and model sand surfaces in aqueous solutions: an atomic force microscope (AFM) study. *Water Research* **2002,** *36* (14), 3421-3428.
26. Considine, R. F.; Drummond, C. J.; Dixon, D. R. Force of interaction between a biocolloid and an inorganic oxide: Complexity of surface deformation, roughness, and brushlike behavior. *Langmuir* **2001,** *17* (20), 6325-6335.
27. Kuznar, Z. A.; Elimelech, M. Role of surface proteins in the deposition kinetics of *Cryptosporidium parvum* oocysts. *Langmuir* **2005,** *21* (2), 710-716.
28. Kuznar, Z. A.; Elimelech, M. *Cryptosporidium* oocyst surface macromolecules significantly hinder oocyst attachment. *Environmental Science & Technology* **2006,** *40* (6), 1837-1842.
29. Janjaroen, D.; Liu, Y.; Kuhlenschmidt, M. S.; Kuhlenschmidt, T. B.; Nguyen, T. H. Role of divalent cations on deposition of *Cryptosporidium parvum* oocysts on natural organic matter surfaces. *Environmental Science & Technology* **2010,** *44* (12), 4519-4524.
30. Kuznar, Z. A.; Elimelech, M. Direct microscopic observation of particle deposition in porous media: Role of the secondary energy minimum. *Colloids and Surfaces a-Physicochemical and Engineering Aspects* **2007,** *294* (1-3), 156-162.
31. Tufenkji, N.; Dixon, D. R.; Considine, R.; Drummond, C. J. Multi-scale *Cryptosporidium*/sand interactions in water treatment. *Water Research* **2006,** *40* (18), 3315-3331.
32. Hijnen, W. A. M.; Brouwer-Hanzens, A. J.; Charles, K. J.; Medema, G. J. Transport of MS2 phage, *Escherichia coli*, *Clostridium perfringens*, *Cryptosporidium parvum* and *Giardia intestinalis* in a gravel and a sandy soil. *Environmental Science & Technology* **2005,** *39* (20), 7860-7868.
33. Characklis, G. W.; Dilts, M. J.; Simmons, O. D.; Likirdopulos, C. A.; Krometis, L. A. H.; Sobsey, M. D. Microbial partitioning to settleable particles in stormwater. *Water Research* **2005,** *39* (9), 1773-1782.

34. Tufenkji, N.; Elimelech, M. Spatial distributions of *Cryptosporidium oocysts* in porous media: Evidence for dual mode deposition. *Environmental Science & Technology* **2005,** *39* (10), 3620-3629.

35. Searcy, K. E.; Packman, A. I.; Atwill, E. R.; Harter, T. Association of *Cryptosporidium parvum* with suspended particles: Impact on oocyst sedimentation. *Applied and Environmental Microbiology* **2005,** *71* (2), 1072-1078.

36. Tufenkji, N.; Miller, G. F.; Ryan, J. N.; Harvey, R. W.; Elimelech, M. Transport of *Cryptosporidium oocysts* in porous media: Role of straining and physicochemical filtration. *Environmental Science & Technology* **2004,** *38* (22), 5932-5938.

37. Dai, X. J.; Hozalski, R. M. Effect of NOM and biofilm on the removal of *Cryptosporidium parvum* oocysts in rapid filters. *Water Research* **2002,** *36* (14), 3523-3532.

38. Marly, X.; Chevalier, S.; Bues, M.; Schwartzbrod, J.; Estevenon, O. Experimental investigations and numerical modelling of *Cryptosporidium parvum* transport behaviour in aquifers. *Water Science and Technology* **2001,** *43* (12), 109-116.

39. Shaw, K.; Walker, S.; Koopman, B. Improving filtration of *Cryptosporidium*. *Journal of the American Water Works Association* **2000,** *92* (11), 103-+.

40. Harter, T.; Wagner, S.; Atwill, E. R. Colloid transport and filtration of *Cryptosporidium parvum* in sandy soils and aquifer sediments. *Environmental Science & Technology* **2000,** *34* (1), 62-70.

41. Bradford, S. A.; Tadassa, Y. E.; Pachepsky, Y. Transport of *Giardia* and manure suspensions in saturated porous media. *Journal of Environmental Quality* **2006,** *35* (3), 749-757.

42. Ramirez, N. E.; Sreevatsan, S. Development of a sensitive detection system for *Cryptosporidium* in environmental samples. *Veterinary Parasitology* **2006,** *136* (3-4), 201-213.

43. Brusseau, M. L.; Oleen, J. K.; Santamaria, J.; Cheng, L.; Orosz-Coghlan, P.; Chetochine, A. S.; Blanford, W. J.; Rykwalder, P.; Gerba, C. P. Transport of microsporidium *Encephalitozoon* intestinales spores in sandy porous media. *Water Research* **2005,** *39* (15), 3636-3642.

44. Bradford, S. A.; Bettahar, M. Straining, attachment, and detachment of *Cryptosporidium oocysts* in saturated porous media. *Journal of Environmental Quality* **2005,** *34* (2), 469-478.

45. Darnault, C. J. G.; Steenhuis, T. S.; Garnier, P.; Kim, Y. J.; Jenkins, M. B.; Ghiorse, W. C.; Baveye, P. C.; Parlange, J. Y. Preferential flow and transport of *Cryptosporidium parvum*

oocysts through the vadose zone: Experiments and modeling. *Vadose Zone Journal* **2004,** *3* (1), 262-270.

46. Kim, S. B.; Corapcioglu, M. Y. Analysis of *Cryptosporidium parvum* oocyst transport in porous media. *Hydrological Processes* **2004,** *18* (11), 1999-2009.

47. Darnault, C. J. G.; Garnier, P.; Kim, Y. J.; Oveson, K. L.; Steenhuis, T. S.; Parlange, J. Y.; Jenkins, M.; Ghiorse, W. C.; Baveye, P. Preferential transport of *Cryptosporidium parvum* oocysts in variably saturated subsurface environments. *Water Environment Research* **2003,** *75* (2), 113-120.

48. McGechan, M. B.; Lewis, D. R. Transport of particulate and colloid-sorbed contaminants through soil, part 1: General principles. *Biosystems Engineering* **2002,** *83* (3), 255-273.

49. Logan, A. J.; Stevik, T. K.; Siegrist, R. L.; Ronn, R. M. Transport and fate of *Cryptosporidium parvum* oocysts in intermittent sand filters. *Water Research* **2001,** *35* (18), 4359-4369.

50. Brush, C. F.; Ghiorse, W. C.; Anguish, L. J.; Parlange, J. Y.; Grimes, H. G. Transport of *Cryptosporidium parvum* oocysts through saturated columns. *Journal of Environmental Quality* **1999,** *28* (3), 809-815.

51. Brookes, J. D.; Antenucci, J.; Hipsey, M.; Burch, M. D.; Ashbolt, N. J.; Ferguson, C. Fate and transport of pathogens in lakes and reservoirs. *Environment International* **2004,** *30* (5), 741-759.

52. Abudalo, R. A.; Bogatsu, Y. G.; Ryan, J. N.; Harvey, R. W.; Metge, D. W.; Elimelech, M. Effect of ferric oxyhydroxide grain coatings on the transport of bacteriophage PRD1 and *Cryptosporidium parvum* oocysts in saturated porous media. *Environmental Science & Technology* **2005,** *39* (17), 6412-6419.

53. Byrd, T. L.; Walz, J. Y. Investigation of the interaction force between *Cryptosporidium parvum* oocysts and solid surfaces. *Langmuir* **2007,** *23* (14), 7475-7483.

54. Hsu, B. M.; Huang, C. P.; Pan, J. R. Filtration behaviors of *Giardia* and *Cryptosporidium* - Ionic strength and pH effects. *Water Research* **2001,** *35* (16), 3777-3782.

55. Searcy, K. E.; Packman, A. L.; Atwill, E. R.; Harter, T. Deposition of *Cryptosporidium* oocysts in streambeds. *Applied and Environmental Microbiology* **2006,** *72* (3), 1810-1816.

56. Harter, T.; Atwill, E. R.; Hou, L.; Karle, B. M.; Tate, K. W. Developing risk models of *Cryptosporidium* transport in soils from vegetated, tilted soilbox experiments. *Journal of Environmental Quality* **2008,** *37* (1), 245-258.

57. Edzwald, J. K.; Kelley, M. B. Control of *Cryptosporidium*: from reservoirs to clarifiers to filters. *Water Science and Technology* **1998,** *37* (2), 1-8.

58. Nieminski, E. C.; Ongerth, J. E. Removing *Giardia* and *Cryptosporidium* by conventional treatment and direct filatration. *Journal of the American Water Works Association* **1995,** *87* (9), 96-106.

59. Kim, H. N.; Walker, S. L.; Bradford, S. A. Coupled factors influencing the transport and retention of *Cryptosporidium parvum* oocysts in saturated porous media. *Water Research* **2010,** *44* (4), 1213-1223.

60. Bradford, S. A.; Simunek, J.; Bettahar, M.; van Genuchten, M. T.; Yates, S. R. Significance of straining in colloid deposition: Evidence and implications. *Water Resources Research* **2006,** *42* (12).

61. Liu, Y.; Janjaroen, D.; Kuhlenschmidt, M. S.; Kuhlenschmidt, T. B.; Nguyen, T. H. Deposition of *Cryptosporidium parvum* oocysts on natural organic matter surfaces: microscopic evidence for secondary minimum deposition in a radial stagnation point flow cell. *Langmuir* **2009,** *25* (3), 1594-1605.

62. Hogg, R.; Healy, T. W.; Fuerstenau, D. W. Mutual coagulation of colloidal dispersions. *Transactions of the Faraday Society* **1965,** *62*, 1638-1651.

CHAPTER 2

DEPOSITION OF *CRYPTOSPORIDIUM PARVUM* OOCYSTS ON NATURAL ORGANIC MATTER SURFACES: MICROSCOPIC EVIDENCE FOR SECONDARY MINIMUM DEPOSITION IN A RADIAL STAGNATION POINT FLOW CELL

Published in *Langmuir*, 2009

Liu, Y.; Janjaroen, D.; Kuhlenschmidt, M. S.; Kuhlenschmidt, T. B.; Nguyen, T. H. Deposition of *Cryptosporidium parvum* Oocysts on Natural Organic Matter Surfaces: Microscopic Evidence for Secondary Minimum Deposition in a Radial Stagnation Point Flow Cell, *Langmuir*, 25, 1594-1605.

2.1 Abstract

A radial stagnation point flow (RSPF) system combined with a microscope was used to determine the deposition kinetics of *Cryptosporidium parvum* oocysts on quartz surfaces and silica surfaces coated with Suwannee River natural organic matter (SRNOM) in solutions with different ionic strengths. Microscopic evidence of *C. parvum* oocysts entrapped in the secondary minimum energy well was presented to show that among the entrapped *C. parvum* oocysts, some were washed away by the radial flow and some were able to transfer to deep primary minima and become irreversibly deposited. Experimental data were compared with simulation results obtained by the convective-diffusion equation and Derjaguin-Landau-Verwey-Overbeek (DLVO) theory. The experimental results suggested that surface charge heterogeneity led to higher attachment efficiency at low ionic strength. In addition, maximum attachment efficiency was less than 1 at high ionic strength due to steric interaction.

2.2 Introduction

Cryptosporidium parvum is a protozoan pathogen capable of infecting a wide range of mammals, including humans. An infected animal or human suffers from cryptosporidiosis, a severe diarrheal disease, which lasts 1 to 2 weeks for immunocompetent individuals, but could

be fatal for infants and immunosuppressed people. Because *C. parvum* oocysts are very resistant to water treatment processes, including chlorine-based disinfection,[1, 2] outbreaks of cryptosporidiosis occur throughout the year.[3] For example, 400,000 individuals in Milwaukee, WI were infected with *C. parvum* in 1993. Corso et al.[4] estimated that the 1993 outbreak in Milwaukee caused the loss of $31.6 million in medical care costs and $46.5 million in productivity loss. Even though the contamination sources have never been identified conclusively, this outbreak was associated with the failure of a filtration system at a Milwaukee water treatment plant, which used raw water from Lake Michigan, and an increase in the number of *Cryptosporidium* oocysts that had occurred that year due to unusually high spring run-off.[5, 6]

The transport and survivability of *C. parvum* oocysts in the sub-surface environment is of great concern for water quality. Attachment of *C. parvum* oocysts to silica or sand surfaces has been studied extensively at scales ranging from nanometer to laboratory bench to field studies.[7-20] Packed columns have been used to study transport and removal of *C. parvum* oocysts in porous granular media.[7-9, 13, 15, 20-38] Natural soils,[21, 27] quartz sand[9] and uniform glass beads[24, 39, 40] are used as granular media or surrogates for granular media. The influence of ionic strength and pH on *C. parvum* oocysts transport suggests that a combination of electrostatic and specific interactions controls *C. parvum* oocysts deposition.[8, 9, 36] Results of studies using the column technique demonstrate the important role of secondary minimum deposition for the transport of *C. parvum* oocysts and other microorganisms in porous media.[8, 9, 41, 42]

Atomic force microscopy (AFM) and the radial stagnation point flow (RSPF) system are techniques used to study the interactions between microorganisms and collector surfaces. AFM studies illustrate that *C. parvum* oocyst wall macromolecules control the interactions between the *C. parvum* oocysts and a silica surface.[10-12, 37] A RSPF system with well-defined hydrodynamic conditions is used to conduct real time observation of deposition of microorganisms onto bare quartz surfaces or conditioning films at the forward stagnation point of granular media.[17-19] A number of physical and chemical factors that control the surface properties of microorganisms and the collector surface have been identified. Specifically, these factors include the influence of solution chemistry on deposition, including ionic strength, pH, divalent ions and the presence of nutrients.[17-19, 43] In addition, a number of studies have shown the influence of surface properties of microorganisms and conditioning film on deposition,[44, 45] such as surface macromolecules, pathogen growth phase and reduced surface complexity.[18, 19, 44, 46, 47] Those results also

emphasize the importance of electrostatic and specific interactions on deposition of microorganisms.

Even though the above-mentioned studies shed light on the mobility of microorganisms in the aquatic environment, our understanding of the fate and transport of *C. parvum* oocysts is not complete. Limited studies[24, 48, 49] have shown that significant numbers of oocysts can be retained by biofilm. Specifically, Dai and Hozalski[24] studied the effect of natural organic matter (NOM) and biofilm on the removal of *C. parvum* oocysts in columns. In sub-surface environmental systems, ferric and aluminum oxyhydroxides and clay minerals cover 3-4% of quartz and feldspar surfaces.[50, 51] Ferric and aluminum oxyhydroxides and clay minerals are positively charged at near-neutral pH values. Subsequently, these positively charged components can be covered by negatively charged macromolecules, such as NOM, polysaccharides, or proteins, which are the products of microbial activity. While quartz surface has been used extensively as a representative negatively charged surface for colloids deposition and transport study, mineral surfaces covered with NOM are abundant in soil environments and have significant effect on deposition and transport of colloids and biocolloids. For example, NOM blocks surface adsorption sites for bacteriophages in soil columns.[52] A recent study has shown that deposition of bacteriophage MS2 on NOM-coated surface is significant lower than on clean quartz surface.[53] Accurate models to predict *C. parvum* oocyst transport in natural environmental systems require a thorough understanding of interactions between *C. parvum* oocysts and surfaces coated with biomacromolecules. The RSPF system is a powerful technique to perform real time observation of particle-surface interaction. Nevertheless, all of the RSPF studies that involve *C. parvum* oocysts are conducted on quartz surface. It is vital to expand our knowledge of the interaction between *C. parvum* oocysts and surfaces coated with biomacromolecules.

The Derjaguin-Landau-Verwey-Overbeek (DLVO) theory is commonly used to interpret colloidal particle-collector surface interaction. However, the results of both column and RSPF experiments disagree with the theoretical expectations predicted by DLVO theory.[44, 54] One explanation for this discrepancy is that oocysts deposited in the shallow secondary minimum energy well may transfer to the deep primary minimum energy well and deposition consequently increases at low ionic strength.[36, 44, 55] De Kerchove et. al[44] recently developed a microscopic technique for direct observation of the secondary minimum deposition of bacteria on alginate conditioning film.

Our objective was to study the factors that influence the deposition of *C. parvum* oocysts onto quartz and NOM-coated silica surface. We hypothesize that electrostatic interactions combined with surface charge heterogeneity and steric interaction control the deposition of *C. parvum* oocysts onto NOM-coated silica surface. We compared the experimental deposition results of *C. parvum* oocysts and CML particles onto quartz and NOM-coated silica surfaces with deposition results predicted by classic DLVO theory. The microscopic technique developed recently by de Kerchove et al.[44] was used to demonstrate the evidence of *C. parvum* oocysts and CML particles deposited onto both quartz and NOM-coated silica surfaces at the secondary minimum energy well. Our results indicated that deposition at the secondary minimum energy well increased attachment efficiency at low ionic strength, charge heterogeneity led to higher attachment efficiency at low ionic strength, and steric repulsion prevented deposition of oocysts on the collector surface.

2.3 Materials and Methods

***C. parvum* Oocyst, CML Particles.** Viable *C. parvum* oocysts (4-5 μm in diameter) were isolated from the feces of male Holstein calves (IACUC protocol # 04070) using a method described in our previous work.[56] The final *C. parvum* oocysts were washed through centrifugation in Tris-ethylenediamine-tetraacetic acid (Tris-EDTA, 50 mM Tris, 10 mM EDTA) and stored at 4 °C in a solution of 50% Hanks' balanced salt solution (HBSS, GIBCO, Grand Island, New York) and 50% antibiotic-antimycotic solution (0.6% penicillin, 1% streptomycin, 0.0025% amphotericin, and 0.85% NaCl in sterile water). Carboxylate modified latex (CML) particles were used as well-characterized particles with homogenous charge distribution. CML particles were purchased from Invitrogen (4 μm in diameter, 4% w/v). The size of *C. parvum* oocysts and CML particles is slightly different. However, small difference in size of *C. parvum* oocysts and CML particles does not influence our data interpretation. According to the work by Elimelech et al.[57] the slope of the stability curve (i.e. attachment efficiency vs. ionic strength) does not depend on particle size. In addition, we mainly compared the deposition trend of both materials because the CML particles were more charge homogeneous than oocysts. All solutions were made with deionized (DI) water filtered through a 0.22 μm filter.

Before the experiments, *C. parvum* oocysts or CML particles were washed by centrifugation twice at 13,000 rpm for 1 min (Eppendorf centrifuge 5415D) and resuspended in DI water. The desired concentration of *C. parvum* oocysts or CML particles was prepared by suspending the clean particles in the NaCl solution (1 to 300 mM) at ambient pH (pH 5.6-5.8). For each experiment, the number concentration of *C. parvum* oocysts or CML particles was determined by counting with a Hemocytometer (Hausser Scientific, Cat. No. 3100).

Preparation of Substrates. Glass bottom Petri dishes (14 mm in diameter and 0.1 mm thick, MatTek Corporation) were used as frames to hold the RSPF system on the motorized microscope stage. As the Petri dish has a hole at the bottom, a cover slip was glued to the outside of the dish bottom to cover the hole. A custom-made RSPF cell was glued to the Petri dish with the capillary inlet at the center of the dish, as shown in Figure 2.1.

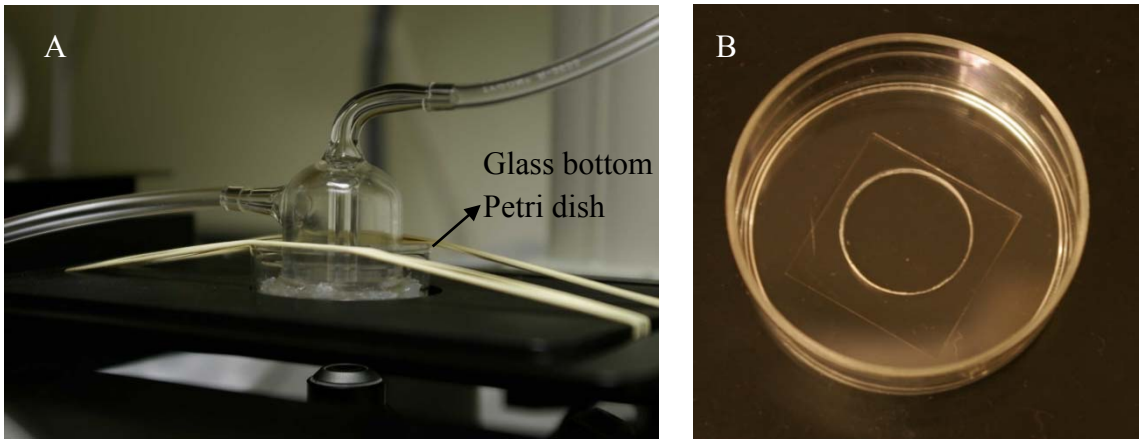

Figure 2.1 A Radial stagnation point flow system (A) with a glass bottom Petri dish (B)

For experiments on quartz surface, we replaced the glass cover slip of the glass bottom Petri dish with a quartz cover slip (25 mm in diameter and 0.1 mm thick, Electron Microscopy Sciences), as shown in Figure 2.2. This quartz cover slip was soaked in 2% Hellmanex II (Hellma GmbH & Co. KG) solution overnight, and then soaked in Nochromix bath (Nochromix reagent, Fisher Cat. No. 04-345-20, in sulfuric acid, Fisher Cat. No. A300-212) overnight. The quartz cover slip was thoroughly rinsed with DI water until the water was neutral. After being dried with ultrahigh-purity N_2, the quartz cover slip was treated in an ozone/UV chamber for 30 min and used for deposition experiments.

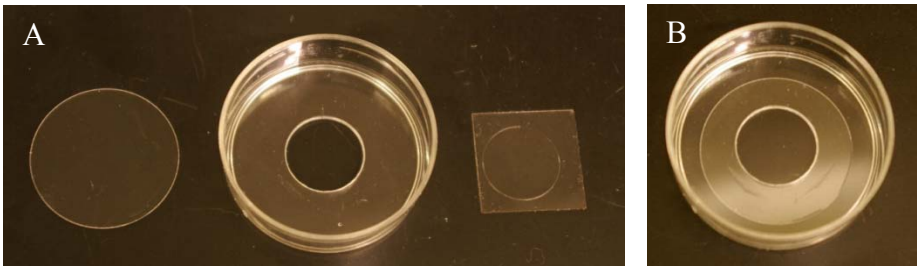

Figure 2.2 Replaced the glass bottom of the Petri dish (A) with quartz cover slip (B)

For experiments on poly-L-lysine (PLL, average molecular weight of 150,000, Sigma) coated silica surface, we used a method similar to that employed in previous work[44, 58, 59] to adsorb a layer of poly-L-lysine hydrobromide onto the glass bottom of the Petri dish. 300 µL of a filtered solution containing 0.125 g/L PLL in 10 mM HEPES and 100 mM NaCl buffer was added to cover the glass bottom for 24 hours at 4 °C and then rinsed with DI water. The Petri dishes were dried in a desiccator at room temperature until use. The PLL-coated silica surfaces were used for deposition experiments under non-repulsive conditions and for subsequent coating with NOM.

For experiments on NOM-coated silica surfaces, we further coated the PLL-coated glass bottoms of the Petri dishes with NOM. Suwannee River natural organic matter (SRNOM, Suwannee River, RO isolation, 1R101N) was selected as a representative aquatic NOM. This material was obtained from the International Humic Substances Society (IHSS) Standard collection. ICP-MS analysis showed that 560 mg/L SRNOM (240 mg/L TOC) contained 66 µg/L Mg, 3 µg/L Sr, 0.9 µg/L Ba and 540 µg/L Al. To prepare the SRNOM solution, 56.2 mg of SRNOM were added to 100 mL DI water. The solution was stirred for 24 hours using a magnetic stirrer. After stirring, the solution was filtered using a 0.22 µm millipore filter. SRNOM-coated surface was formed by adding 300 µL SRNOM to cover the PLL-coated glass bottom Petri dishes for 24 hours at 4 °C, after which time the supernatant was removed. The Petri dishes were dried and particle deposition experiments were performed over a range of ionic strengths (1 to 300 mM NaCl) at ambient pH (pH 5.6-5.8). In the presence of 1 mM NaCl, essentially no particles deposited onto a SRNOM surface. This means that the positively charged PLL layer was completely covered by a layer of SRNOM. Otherwise, negatively charged *C. parvum* oocysts or CML particles would have deposited onto the regions of the uncovered positively

charged PLL layer and substantially higher deposition would have been observed. Thus, this coating method was proven to be sufficient.

Surface Potentials. The electrophoretic mobilities of *C. parvum* oocysts, CML particles, quartz surface and PLL- and SRNOM-coated silica surfaces were determined under a range of ionic strengths (1 to 200 mM NaCl) at ambient pH (pH 5.6-5.8) at 25 °C using a Zetasizer Nano analyzer (Malvern Instruments Ltd). The quality of the measurement was judged by the Dispersion Technology Software 5.03 supplied by the manufacturer. The bases of judgment include signal strengths and repeatability of the measurements. Preliminary experiments were conducted to determine the concentration of *C. parvum* oocysts and CML particles for the electrophoretic mobility experiments. These concentrations were 2.5×10^6 oocysts/mL and 1.2×10^6 CML/mL, respectively. Medrzycha[60] suggested that zeta potential is independent of particle concentration if the ratio of the number of bulk ions to particle number is not lower than 1.6×10^6 for particles of diameter of 1.6 μm and not lower than 1.0×10^7 for particles of diameter of 3 μm. The lowest ionic strength used in this study was 1 mM NaCl. Converted to number of bulk ions, there were at least 1.2×10^{18} ions/mL. The particle concentration used in electrophoretic mobility experiment was no more than 1.2×10^6 particles/mL. The ration of the number of bulk ions to particle number was safely within the range suggested by Medrzycha where zeta potential (proportional to electrophoretic mobility) is independent of particle concentration.

PLL-coated and SRNOM-coated silica particles were used as surrogates for the surface-modified glass bottom of the Petri dishes. The commercial silica particles (1.6 μm in diameter) were obtained from Bangs Laboratories, Inc. (Cat. No. SS04N-6950). Silica particles were rinsed by centrifugation in DI water. The clean bare silica particles were used for subsequent coating with PLL and SRNOM. We coated the silica particles with a layer of PLL by successively dispersing 1.2×10^8 clean bare silica particles in 1 mL PLL/HEPES solution for 24 hours. The coated particles were then removed from the PLL/HEPES solution by centrifugation and rinsed with DI water. The PLL-coated silica particles were used for electrophoretic mobility measurements or for subsequent coating with SRNOM. For coating with SRNOM, 1.2×10^8 PLL-coated silica particles were dispersed in 1 mL SRNOM solution for 24 hours. The SRNOM-coated particles were removed from the SRNOM solution by centrifugation and rinsed with DI water. The SRNOM-coated silica particles were used for electrophoretic mobility experiments.

The particles from pulverized quartz cover slip (approximately 2 μm) were used as surrogates for the quartz surface and are further referred to as quartz particles for electrophoretic mobility measurement. To prepare the quartz particles, we pulverized the quartz cover slip into small particles with an agate mortar. The small particles were suspended in solutions with ionic strengths ranging from 1 mM to 200 mM and the solutions were sonicated for one hour. Aliquots (3 mL) of the supernatant containing quartz particles were used for electrophoretic mobility measurements.

The surface potential of particles was derived from the measured electrophoretic mobility to zeta potential using the classic Smoluchowski equation or to outer surface potential using Ohshima's[61] approach. The zeta potential of a particle loses its physical meaning when the particle surface has a layer of macromolecules. Ohshima's theory assumes that such particle is composed of a hard core and an ion-penetrable surface layer of polyelectrolytes. Ohshima's model has been used to describe the behavior of viruses, bacteria and protozoan oocysts.[62] According to Ohshima's model,[61] particles with radius *a* are assumed to be covered by an ion-penetrable polyelectrolyte layer with thickness *d*. In the polyelectrolyte layer, the ionized polymer segments of valence *Z* are assumed to be uniformly distributed with a density of *N*. In addition, the polymer segments in the polyelectrolyte layer are assumed to be uniformly distributed with a density of N_p and yield frictional force on the liquid in the polyelectrolyte layer. The frictional coefficient (υ) of these polymer segments is:

$$\upsilon = 6\pi\eta a_p N_p \tag{2.1}$$

where a_p is the equivalent sphere radius of the polymer segment and η is the solution viscosity.

Based on these assumptions, under conditions where $a >> d$, $\kappa a >> 1$ and $\lambda a >> 1$, the electrophoretic mobility can be expressed as:

$$\mu = \frac{2\varepsilon_r \varepsilon_0}{3\eta} \frac{\psi_0 / \kappa_m + \psi_{DON} / \lambda}{1/\kappa_m + 1/\lambda} + \frac{ZeN}{\eta\lambda^2} \tag{2.2}$$

with

$$\psi_0 = \frac{kT}{ze}\left(\ln\left[\frac{ZN}{2zn} + \left\{ \left(\frac{ZN}{2zn} \right)^2 + 1 \right\}^{1/2} \right] + \frac{2zn}{ZN}\left[1 - \left\{ \left(\frac{ZN}{2zn} \right)^2 + 1 \right\}^{1/2} \right] \right) \tag{2.3}$$

$$\psi_{DON} = \frac{kT}{ze}\left(\ln\left[\frac{ZN}{2zn} + \left\{\left(\frac{ZN}{2zn}\right)^2 + 1\right\}^{1/2}\right]\right) \tag{2.4}$$

$$\kappa_m = \kappa\left[1 + \left(\frac{ZN}{2zn}\right)^2\right]^{1/4} \tag{2.5}$$

where μ is the electrophoretic mobility, ε_0 is the permittivity of a vacuum, ε_r is the relative permittivity of the solution, η is the viscosity of the solution, ψ_0 is the outer surface potential at the boundary between the polyelectrolyte layer and the surrounding electrolyte solution, ψ_{DON} is the Donnan potential, e is the elementary electric charge, k is the Boltzmann constant, T is absolute temperature, M is the number of ion species, z is the valence of each symmetrical surrounding electrolyte species, n is the bulk concentration of the surrounding electrolyte species, κ is Debye-Hückel parameter, and $1/\lambda$ is the electrophoretic softness, which has inverse dependence with the frictional forces exerted on the liquid flow by the polymer segments in the polyelectrolyte layer and is related to the equivalent sphere radius of the polymer segment (a_p) and the density (N_p) of the polymer segment in this surface layer,

$$\lambda = \left(\frac{\upsilon}{\eta}\right)^{1/2} = \left(6\pi a_p N_p\right)^{1/2} \tag{2.6}$$

At equilibrium, the electric force on the ionized groups of the polyelectrolyte should be equal to the frictional force yielded by polymer segments[61]. Consequently, the electrophoretic mobility of soft particles tends to approach a non-zero limiting value, which is given by Equ. 2 as $\kappa \rightarrow \infty$,

$$\mu \rightarrow \mu^{\infty} = \frac{ZeN}{\eta\lambda^2} \tag{2.7}$$

First, the experimental electrophoretic mobility data were fitted to Ohshima's equations to get the value of ZN and $1/\lambda$. Since the non-zero limiting electrophoretic mobility at high ionic strength is sensitive to the value of ZN and $1/\lambda$, the experimental electrophoretic mobilities were fitted at ionic strengths above 30 or 40 mM NaCl. Subsequently, these values of ZN and $1/\lambda$ were used to calculate the outer surface potential for all ionic strength ranges according to Equation 2.3.[61, 63]

Kinetics of *C. parvum* Oocyst Deposition in a RSPF System. Deposition kinetics of *C. parvum* oocysts and CML particles on quartz, PLL-coated and SRNOM-coated surfaces were studied in a RSPF system at 25 °C. The RSPF system used in our experiments had an injection

capillary radius, R, of 1 mm and a distance, h, between the capillary outlet and the collector surface of 0.7 mm. A constant flow of 1 mL/min was induced by a syringe pump (Series 74900, Cole-Parmer). Particle deposition kinetics experiments were performed over a range of ionic strengths (1 to 300 mM NaCl) at ambient pH (pH 5.6-5.8).

For deposition experiments, the solution concentrations of *C. parvum* oocysts and CML particles were 2.5×10^6 oocysts/mL and 1.5×10^6 CML/mL, respectively, at ionic strengths up to 30 mM. At ionic strengths higher than 60 mM, the solution concentrations were reduced to 1.5×10^6 oocysts/mL and 1.0×10^6 CML/mL to avoid aggregation. First, we pumped the electrolyte solution with a flow rate of 1 mL/min for about 5 min until the flow cell was full of solution. Then we switched to an electrolyte solution containing particles with the same flow rate for 30 min. After that deposition period, we switched to a particle-free electrolyte solution of 1 mM NaCl for 15 min. All deposition experiments were repeated at least twice. Deposited particles were observed and counted in a rectangular viewing area every 1 or 15 seconds for 30 minutes using an electronic inverted microscope equipped with a phase filter at bright field. We used an Eclipse Nikon TS 100 with a viewing area of 250 × 190 μm for *C. parvum* oocysts deposition experiments and a Leica DMI5000M with a viewing area of 296 × 222 μm for CML particles deposition experiments. For *C. parvum* oocysts, the microscope images were recorded using a Photometrics CoolSNAP ES from Roper Scientific Photometrics, and analyzed with MetaMorph 6.3r7 software. For CML particles, the microscope images were recorded using the QIMAGING RETIGA 2000R Fast 1394, and analyzed with Image-Pro 6.2 software. The deposition rate coefficient, k_d, corresponds to particle deposition flux (number of deposited particles per viewing area per time) normalized by the initial particle concentration. Deposition kinetics is represented as attachment efficiency, α, which is calculated as the ratio between particle deposition rate coefficients under repulsive conditions (such as onto quartz or SRNOM-coated silica surfaces) and particle deposition rate coefficients under non-repulsive conditions (onto PLL-coated silica surface) at a given ionic strength:

$$\alpha = \frac{k_{d,SRNOM}}{k_{d,PLL}} \tag{2.8}$$

Direct Observation of Secondary Minimum Deposition. Microscopic observation of secondary minimum deposition was recorded every second or 15 seconds over a course of 30 min. The links to the movies are provided via internet. The images shown later in the paper were

composite images generated by superimposing successive pictures taken over time. This method developed by de Kerchove et al.[44] allows us to trace the movement of a single oocyst from the moment it enters the microscopic observation field until it deposits or exits the observation field.

DLVO Energy Profiles. The total interaction energy between charged particle and plate surface was calculated as the sum (ϕ_T) of electrostatic (ϕ_{EDL}) and van der Waals (ϕ_{VDW}) interactions using the Hogg et al. expression:[17, 64]

$$\Phi_{EDL} = \pi\varepsilon_0\varepsilon_r a\left\{2\psi_p\psi_c \ln[\frac{1+\exp(-\kappa H)}{1-\exp(-\kappa H)}] + (\psi_p^2+\psi_c^2)\ln[1-\exp(-2\kappa H)]\right\} \quad (2.9)$$

where H is the separation distance between particle and the collector surface, and ψ_p and ψ_c are the surface potentials of the particle and collector surface. The retarded van der Waals attractive interaction energy was calculated using:[65]

$$\Phi_{VDW} = -\frac{Aa}{6H}\left(\frac{1}{1+14H/\lambda'}\right) \quad (2.10)$$

where λ' is the characteristic wavelength of the dielectric (assumed to be 100 nm) and A is the Hamaker constant of the interacting medium. We used a Hamaker constant of 6.5×10^{-21} J for *C. parvum* oocyst deposition and 1×10^{-20} J for CML particle deposition, as suggested by Kuznar et al.[17] and de Kerchove et al.[44], respectively.

Predict Attachment Efficiency in RSPF System with DLVO Theory. The attachment efficiency was calculated using the method described by Weronski et al. and de Kerchove et al.[44, 66] Briefly, this method numerically solved the convective-diffusion equation for particle deposition flux at the primary minimum in a particular RSPF system:

$$\nabla\cdot(uC) = \nabla\cdot(D\cdot\nabla C) - \nabla\cdot\left(\frac{D\cdot F}{kT}C\right) \quad (2.11)$$

where *u* is the particle velocity, *C* is the particle concentration, *D* is the particle diffusion coefficient, and *F* is the summation of external forces that include gravity force, buoyancy force and colloidal force. The total DLVO interaction potential that includes electrostatic (ϕ_{EDL}) and van der Waals (ϕ_{VDW}) interactions is used to derive colloidal force. The hydrodynamics of the flow cell used for the convective-diffusion equation were obtained by numerically solving the Navier-Stokes equation for the flow cell. Specifically, the flow field can be characterized by the flow intensity parameter α_s which depends on the geometry of the system and the Reynolds

number (*Re*). In the region close to the stagnation point, the flow field can be presented in terms of the cylindrical coordinates r and z:[67]

$$v_r = \alpha_s z r \tag{2.12}$$

where v_r is the radial velocity of the fluid. The Navier-Stokes equation was numerically solved in the region of the stagnation point with Comsol 3.3 to get the value of v_r changing with r. Then, the value of α_s was calculated at the stagnation point with z equal to the average diameter of *C. parvum* oocysts.[44]

A dimensionless form of the flow intensity parameter, α_s^*, is used to characterize the flow field of the RSPF system:

$$\alpha_s^* = \alpha_s \frac{Re\upsilon}{R^3} \tag{2.13}$$

where υ is the kinematic viscosity.

2.4 Results and Discussion

Surface Potentials. It is common in colloid deposition and transport literature to use zeta potential for surface charge potential and to interpret deposition data. The outer surface potential concept was developed as an alternative for soft particles with penetrable polyelectrolyte surface layer[61, 68] to the zeta potential approach, which was developed originally for hard particles. Thus, for soft particles such as *C. parvum* oocysts, the use of zeta potential is not adequate and we explore the use of Ohshima's approach to characterize surface charge potential. The electrophoretic mobility was measured to characterize the surface potential of the particles and collectors (open symbols in Figure 2.3 and Figure 2.4). Electrophoretic mobilities fitted by Ohshima's theory were shown as solid lines in Figure 2.3 and Figure 2.4. For each type of surface, zeta potential (overlapped open symbols in Figure 2.3 and Figure 2.4) and outer surface potential (dashed lines in Figure 2.3 and Figure 2.4) were derived and compared.

1) Electrophoretic Mobility of *C. parvum* Oocysts, CML particles and substrate surfaces. As shown in Figure 2.3, the electrophoretic mobility of *C. parvum* oocysts (open triangle) increased from -1.13 μmcm/Vs at 1 mM NaCl to -0.34 μmcm/Vs at 200 mM NaCl. When converted from the electrophoretic mobility, the zeta potential of *C. parvum* oocysts (overlapped open triangle) increased from -14.43 mV at 1 mM NaCl to -4.38 mV at 200 mM NaCl. The

complex property of the *C. parvum* oocyst wall surface leads to variation in zeta potential for *C. parvum* oocysts from different sources. Previous studies[17, 19, 69] have shown that the zeta potential of *C. parvum* oocysts varies from -7 mV to -36 mV at pH 5.5-5.7 in 1 mM KCl electrolyte solution, and from -1 mV to -8 mV at pH 5.5-5.7 in 100 mM KCl electrolyte solution. The zeta potential of *C. parvum* oocysts used in our work was -14 mV in 1 mM NaCl and -5 mV in 100 mM NaCl and is, therefore, in the range of the published data.

The electrophoretic mobility of CML particles (open circle) increased from -6.83 μmcm/Vs at 3 mM NaCl to -1.90 μmcm/Vs at 200 mM NaCl. De Kerchove et al.[44] reported that the electrophoretic mobilities of CML particles increased from -7 μmcm/Vs in 3 mM KCl electrolyte solution to -2 μmcm/Vs in 200 mM KCl electrolyte solution at pH 5.5-5.7. The electrophoretic mobilities of CML particles in our work, therefore, were comparable to the published data.

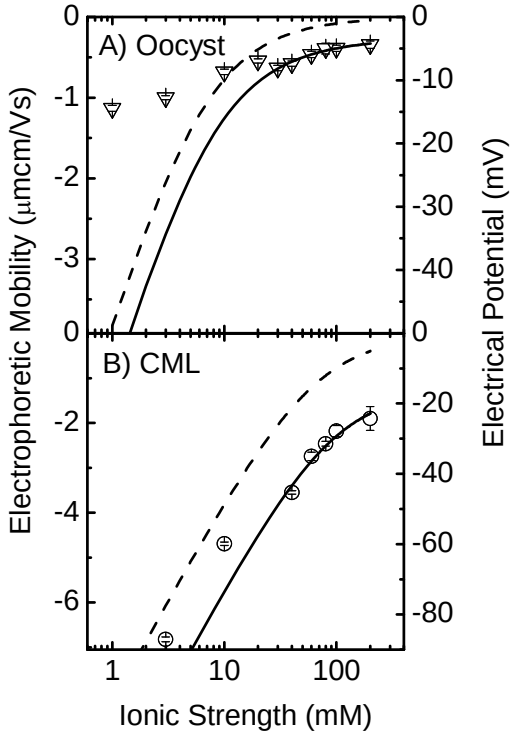

Figure 2.3 Experimental electrophoretic mobility (open symbols), fitted electrophoretic mobility by Ohshima's theory (solid lines), zeta potential calculated by the Smoluchowski equation (open symbols overlapped with that of experimental electrophoretic mobility because zeta potential is proportionate to electrophoretic mobility) and outer surface potential calculated by Ohshima's theory (dashed lines) for (A) *C. parvum* oocysts and (B) CML particles as a function of ionic strength. Experiments were carried out at ambient pH (pH 5.6 – 5.8) and a temperature of 25 ºC.

As shown in Figure 2.4, electrophoretic mobility of PLL-coated particles (open square) was positive and became less positive with increasing ionic strength (from +6.3 μmcm/Vs at 1 mM NaCl to +1.7 μmcm/Vs at 200 mM NaCl). Electrophoretic mobilities of quartz (open circle) and SRNOM-coated particles (open triangle) were negative and became less negative with increasing ionic strength. Specifically, electrophoretic mobilities of quartz particles and SRNOM-coated silica particles respectively increased from -2.53 and -3.21 μmcm/Vs at 1 mM NaCl to -0.18 and -1.00 μmcm/Vs at 200 mM NaCl.

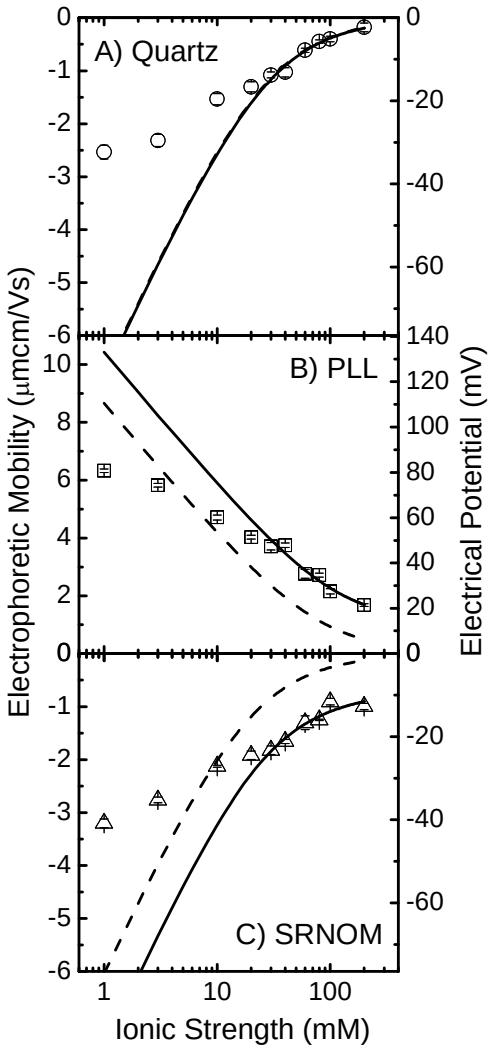

Figure 2.4 Experimental electrophoretic mobility (open symbols), fitted electrophoretic mobility by Ohshima's theory (solid lines), zeta potential calculated by the Smoluchowski equation (overlapped open symbols) and outer surface potential calculated by Ohshima's theory (dashed lines) for (A) quartz particles, (B) PLL-coated silica particles and (C) SRNOM-coated silica particles as a function of ionic strength. Experiments were carried out at ambient pH (pH 5.6 – 5.8) and a temperature of 25 ºC.

It can be seen in Figure 2.3 and Figure 2.4 that the experimental electrophoretic mobility for all surfaces (except the surface of the CML particles) was generally more neutral than Ohshima's model suggested at low ionic strength. The deviation was mainly caused by the failure to fulfill the assumption of Ohshima's model that ionized groups and polymer segments were uniformly distributed inside the surface layer.[61] It is suggested that the deviation is attributed to either the non-uniform distribution of ionized groups and polymer segments[70] or lack of surface polyelectrolyte layer.[44] For the same reason, the deviation between experimental and Ohshima's model fitted electrophoretic mobility was less severe for commercial CML particles since they are expected to be more uniformly charged. The better fitting for CML particles has been documented in a number of studies.[44, 63] Moreover, the discrepancy between Ohshima's model and experimental observation was less severe at high ionic strength because the surrounding counter ions neutralized the charge in the surface layer and compressed the surface layer at high ionic strength.

Electrophoretic mobility of quartz particles was consistently approaching zero in a solution of high ionic strength (Figure 2.4, A). This observation was expected because of the lack of surface macromolecules on the quartz particles. Without surface macromolecules, the surface charge could be completely shielded by solution ions at high ionic strength.[61] In contrast, in the presence of soft surfaces, electrophoretic mobilities of *C. parvum* oocysts, CML particles (Figure 2.3), and PLL- and SRNOM-coated silica particles (Figure 2.4) tended to approach a non-zero limitation. This non-zero limiting value of electrophoretic mobility ($ZeN/\eta\lambda^2$) was expected, as shown in Equations 2.2 and 2.7.

2) Surface Potentials and Surface Softness of *C. parvum* Oocysts, CML Particles and Substrate Surfaces. With the presence of a soft electrolyte layer, zeta potential lost its meaning to some extent. On the contrary, outer surface potential shed light on the soft layer properties of the particles. Electrophoretic softness reflects the equivalent sphere radius of the polymer segment (a_p) and the density (N_p) of the polymer segment in the polyelectrolyte layer on the particle surface. The fitted value of the uniform charge density ZN and the particle electrophoretic softness $1/\lambda$ within the polyelectrolyte layer for Ohshima's theory are shown in Table 2.1. As shown in Table 2.1, *C. parvum* oocysts had the highest particle electrophoretic softness ($1/\lambda$=1.23 nm) because the surface of the *C. parvum* oocyst wall was characterized by a layer of polysaccharide and protein filamentous material.[71, 72] The SRNOM-coated silica particle

had the second largest particle electrophoretic softness (λ=1.10 nm), which was consistent with its heterogeneous layer of carboxylate and phenolic functional groups.[73] As NOM is broken-down organic matter, the NOM macromolecules were expected to be less complex compared to those found on the surface of viable *C. parvum* oocysts. CML particles had the third largest particle electrophoretic softness (λ=0.82 nm) due to these particles' layer of polyelectrolyte carboxyl groups. PLL-coated silica particles had the fourth largest particle electrophoretic softness (λ=0.67 nm). The polymer PLL is composed of homogeneous polyethylene glycol chains. As typical hard particles, quartz particles had the least particle electrophoretic softness (λ=0.03 nm). The fitted values of particle electrophoretic softness were in good agreement with the physical characteristics of the particle surfaces.

Table 2.1 Fitted value of the uniform charge density *ZN* and the particle electrophoretic softness $1/\lambda$ within the polyelectrolyte layer determined by Ohshima's theory

Particle	*ZN* (mM)	$1/\lambda$ (nm)	Illustrations
CML	-161	0.82	
Oocysts	-16	1.23	
Quartz	-75	0.03	
PLL-coated	199	0.67	
SRNOM-coated	-53	1.10	

Using the fitting value of *ZN* and $1/\lambda$, we calculated the outer surface potential over the entire range of ionic strength (Figure 2.3 and Figure 2.4, dashed lines). The calculated outer surface potential of quartz particles was similar to the zeta potential and seemed to approach zero at high ionic strength. This was in good agreement with the characteristic of the quartz surface, regarding its lack of surface macromolecules. The calculated outer surface potential of other surfaces was more neutral than the zeta potential and seemed to approach zero at high ionic strength. Outer surface potential is sensitive to the shielding effects of surrounding electrolytes, and is expected to approach zero as the electrolyte concentration increases.[61] Both zeta potential and outer surface potential were used to calculate DLVO profiles except for quartz particles as shown below. Only zeta potential was used for quartz particles because of the particles' lack of surface polyelectrolyte layers.

Characterization of Flow Field in the RSPF Cell. The numerical solution of the convective-diffusion equation was compared with experimental data for deposition of *C. parvum*

oocysts or CML particles on either quartz surfaces or NOM-coated surfaces. This numerical solution developed by Weronski and Elimelech[66] for a RSPF system requires the input of parameter α_s^*, which represents the hydrodynamic conditions of the RSPF.

To verify our numerical solution for the Navier-Stokes equation, we studied the dependence of α_s^* as a function of Reynolds number with respect to *h/R* values equal to 0.7, 1.0 and 1.7 as shown in Figure 2.5. Our solutions for *h/R* of 1.0 (Figure 2.5, open square) and 1.7 (Figure 2.5, open triangle) are compared to the solutions published by Dabros and van de Ven [67] for *h/R* of 1.0 (Figure 2.5, dashed line) and 1.7 (Figure 2.5, solid line). As shown in Figure 2.5, our solutions for *h/R* of 1.0 and 1.7 were consistent with the solution published by Dabros and van de Ven, and the calculation for our RSPF cell with *h*/*R* of 0.7 was parallel to those for *h/R* of 1.0 and 1.7. This observation confirmed our calculation. The numerical flow field is shown in Figure 2.6. Our RSPF cell had a *Re* of 5.29 and the corresponding α_s^* of 9.4 with *h*/*R* of 0.7 and a flow rate of 1 mL/min.

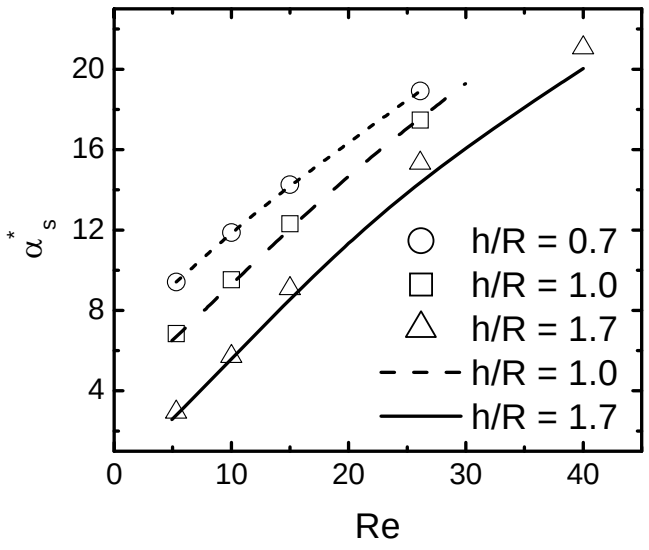

Figure 2.5 Numerical solution of the dimensionless flow intensity parameter, α_s^*, for h/R of 0.7, 1.0 and 1.7. The open circle represents our solution for the RSPF system that we used in the experiment (h/R = 0.7). The open square and triangle represent our solutions for h/R = 1.0 and h/R = 1.7 respectively; the dashed and solid lines indicate the solution of the same geometry published by Dabros and van de Ven.[67]

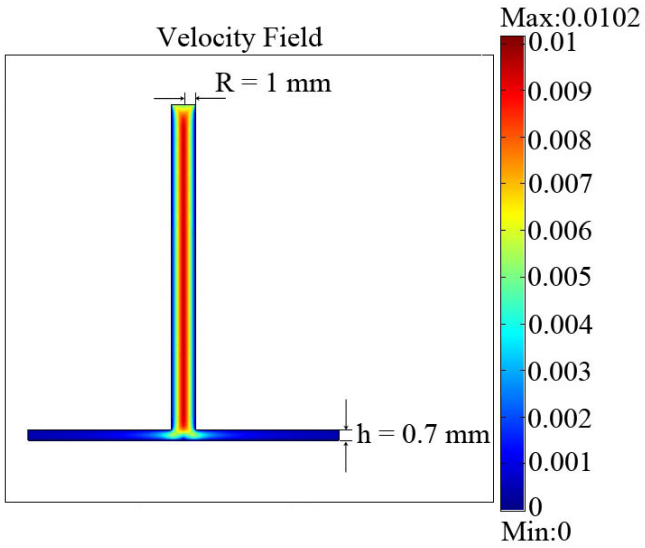

Figure 2.6 Numerical solution for the flow field of the radial stagnation point flow system. Drawing is to scale.

In addition, Dabros et al.[67] defines stagnation point area as being where the wall vorticity $\omega_s = \alpha_s r$ varies less than 3 to 4% from the wall vorticity at $r = 0$. Based on the numerical solution[44], the wall vorticity in the view area varied less than 1%, which shows that the view area was within the stagnation point flow field.

DLVO Energy Profile. The factors influencing the interactions between particles and collector surfaces include van der Waals attraction,[17, 44] electrostatic double layer interaction,[17, 44] surface roughness,[74, 75] surface charge heterogeneity,[76, 77] and steric interaction (e.g. osmotic repulsion, elastic-steric repulsion) .[18, 78, 79] DLVO theory is commonly used to predict the interaction of particles on a flat surface based only on van der Waals attraction and electrostatic double layer interaction.

DLVO interaction energy profiles between a particle and a collector surface under unfavorable conditions were calculated using either zeta potential or outer surface potential. Figure 2.7 shows the interaction energy profile between a *C. parvum* oocyst and a SRNOM-coated surface calculated using zeta potential as a function of ionic strength. It can be seen in Figure 2.7A that the energy barrier between *C. parvum* oocysts and SRNOM-coated surface decreased from 980 kT at 1 mM NaCl to zero at ionic strengths above 30 mM (the so-called critical deposition concentration, CDC). Since no energy barrier exists above CDC, the attachment efficiency would be expected to reach unity. Furthermore, we can see from Figure 2.7A that a deep primary minimum energy well formed when a *C. parvum* oocyst was very close

to the SRNOM-coated surface (within 2 nm distance) at all ranges of ionic strength. Particle deposition in the primary minimum energy well was irreversible. In addition to the primary minimum energy well, the interaction of decreasing electrostatic force and constant van der Waals force produced a secondary minimum energy well with a depth ranging from 0.3 to 29 kT and distance ranging from 100 to 7 nm at ionic strengths ranging from 1 to 30 mM. Particles entrapped in the secondary minimum energy well were reversibly deposited. If the particles can overcome the energy barrier and transfer to the primary minimum energy well, they can deposit irreversibly. In addition, as shown in Eq. 4, the electrostatic force decreased exponentially with separating distance. Thus, as ionic strength increases, the decreasing of electrostatic force at larger distances is more severe than that at smaller distances. Consequently, the distance of the secondary minimum energy well shifted to lower distance.

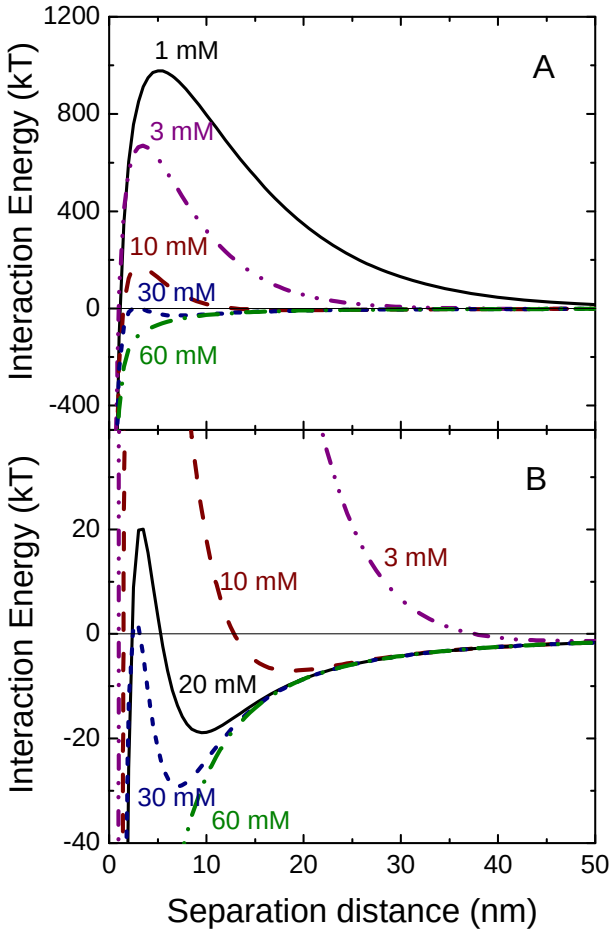

Figure 2.7 Calculated DLVO interaction energy profiles between *C. parvum* oocysts and SRNOM-coated surfaces using zeta potential as a function of ionic strength. The zeta potential was experimentally determined.

Table 2.2 Values of energy barriers, the secondary minimum energy well depth and distance of the secondary minimum energy well for *C. parvum* oocysts and CML particles deposited onto SRNOM-coated silica surface

C. parvum oocysts							
Zeta potential				Outer surface potential			
Ionic strength (mM)	Energy barrier (kT)	Secondary minimum depth (kT)	Distance of secondary minimum (nm)	Ionic strength (mM)	Energy barrier (kT)	Secondary minimum depth (kT)	Distance of secondary minimum (nm)
1	980	-0.3	100	1	10000	-0.2	120
3	670	-1.4	50	3	3000	-1.0	60
10	180	-7.0	20	10	220	-6.8	20
20	20	-19	10	15	10	-15	10
30	2	-29	7	20	NONE	NONE	NONE
60	NONE	NONE	NONE	30	NONE	NONE	NONE
CML particles							
Zeta potential				Outer surface potential			
Ionic strength (mM)	Energy barrier (kT)	Secondary minimum depth (kT)	Distance of secondary minimum (nm)	Ionic strength (mM)	Energy barrier (kT)	Secondary minimum depth (kT)	Distance of secondary minimum (nm)
10	2300	-5.4	26	10	1800	-5.7	25
20	1700	-12	16	20	350	-17	12
30	1400	-19	12	30	NONE	NONE	NONE
60	170	-54	6	60	NONE	NONE	NONE
100	NONE	NONE	NONE	100	NONE	NONE	NONE

Table 2.3 Values of energy barriers, the secondary minimum energy well depth and distance of the secondary minimum energy well for *C. parvum* oocysts and CML particles deposited onto quartz surface

C. parvum oocysts							
Zeta potential for both oocysts and quartz				Zeta potential for oocysts outer surface potential for quartz			
Ionic strength (mM)	Energy barrier (kT)	Secondary minimum depth (kT)	Distance of secondary minimum (nm)	Ionic strength (mM)	Energy barrier (kT)	Secondary minimum depth (kT)	Distance of secondary minimum (nm)
10	100	-8.0	17	10	150	-7.6	18
20	NONE	NONE	NONE	20	NONE	NONE	NONE
CML particles							
Zeta potential for both oocysts and quartz				Zeta potential for CML particles outer surface potential for quartz			
Ionic strength (mM)	Energy barrier (kT)	Secondary minimum depth (kT)	Distance of secondary minimum (nm)	Ionic strength (mM)	Energy barrier (kT)	Secondary minimum depth (kT)	Distance of secondary minimum (nm)
20	800	-13.4	15	20	430	-16.4	13
30	400	-23	10	30	90	-32	8
60	NONE	NONE	NONE	60	NONE	NONE	NONE

In Table 2.2 and 2.3, we list the values of energy barrier, the secondary minimum energy well depth and distance of the secondary minimum energy well for *C. parvum* oocysts and CML particles deposited on either SRNOM-coated silica surface or quartz surface calculated by DLVO theory using either zeta potential or outer surface potential. As shown in Table 2.2, the energy barrier between *C. parvum* oocysts and SRNOM-coated surface disappeared above 30 mM NaCl or 15 mM NaCl when zeta potential or outer surface potential was used; the energy barrier between CML particles and SRNOM-coated surface disappeared above 60 mM NaCl or 20 mM NaCl when zeta potential or outer surface potential was used. In Table 2.3, the energy barrier between *C. parvum* oocysts and quartz surface disappeared above 10 mM NaCl when either zeta potential or outer surface potential was used; the energy barrier between CML particles and SRNOM-coated surface disappeared above 30 mM NaCl when either zeta potential or outer surface potential was used. It is illustrated that the predicted CDC for both *C. parvum* oocysts and CML particles interacting with SRNOM-coated surface would be lower if we applied outer surface potential from Eq. 11 to calculate the energy files. But the predicted CDC for these two types of particles interacting with quartz surface was very similar when either zeta potential or outer surface potential was used. That was due to the fact that we used only zeta potential for quartz surface. It illustrates the importance of the collector surface, which we will discuss in the following sections.

Deposition Kinetics of *C. parvum* Oocysts and CML Particles. The experimental deposition rate coefficients, k_d, of *C. parvum* oocysts and CML particles onto quartz and PLL- and SRNOM-coated silica surfaces are shown in Figure 2.8. Attachment efficiencies, α, were calculated accordingly and are shown in Figure 2.9, as well as the attachment efficiencies predicted by DLVO theory.

1) Deposition Kinetics of *C. parvum* Oocysts and CML Particles Under Non-repulsive Conditions: Role of Surface Roughness. As shown in Figure 2.8, k_d of *C. parvum* oocysts onto PLL-coated silica surface decreased with ionic strength from 3.4×10^{-7} m/s at 1 mM NaCl to 1.9×10^{-7} m/s at 200 mM NaCl. In contrast, k_d of CML particles onto PLL-coated silica surface was quite stable, varying from 2.1×10^{-7} m/s to 2.9×10^{-7} m/s within 1 to 300 mM NaCl.

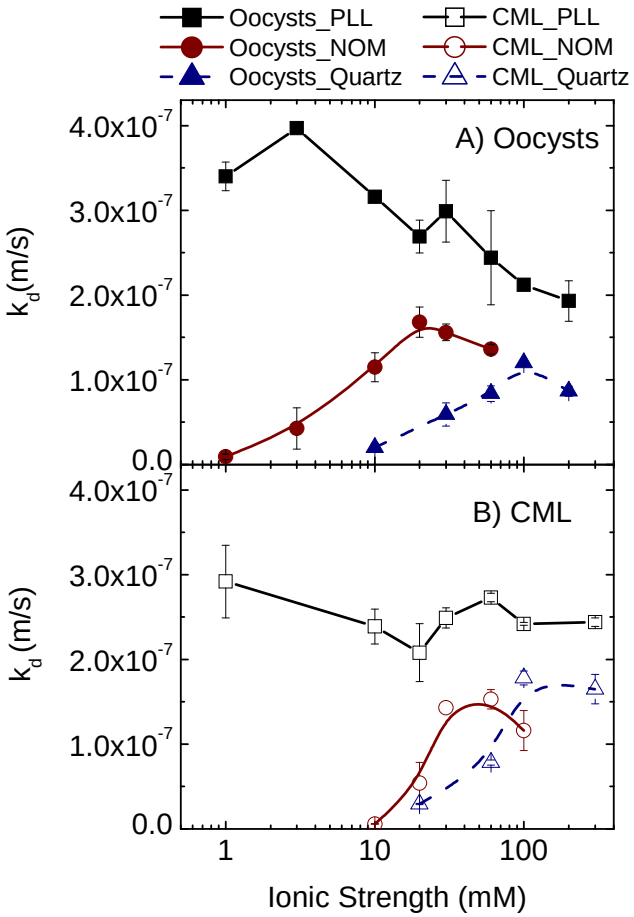

Figure 2.8 The deposition rate coefficient (k_d) for *C. parvum* oocysts and CML particles onto PLL-coated silica, SRNOM-coated silica and quartz surface. Experimental conditions were as follows: capillary flow rate of 1 mL/min (average velocity = 0.0053 m/s with Re = 5.29), pH 5.6 - 5.8, and temperature of 25 ºC.

According to DLVO theory, when there is no energy barrier between particles and collector surface under favorable conditions, the deposition rate should be stable or slightly decrease with ionic strength as a result of a shorter range of attractive electric double layer force at high ionic strength compared to that at low ionic strength due to the compression of the electric double layer.[78] As expected, k_d of CML particles onto PLL-coated surface was quite stable across the entire range of ionic strengths. However, a significant decrease in k_d is observed for *C. parvum* oocysts deposited onto PLL-coated surface, which could indicate the importance of a specific surface property of *C. parvum* oocysts—surface roughness. Suresh et al.[75] studied the effect of roughness on interaction energy between a rough sphere and a smooth plate surface, and developed a modified DLVO energy profile for this system. They showed that the range of

both attractive and repulsive forces between rough particles and the smooth plate was larger than that between smooth particles and the smooth plate. Under non-repulsive conditions, the larger range of attractive electric double layer force enhanced the possibility of particles coming close to the surface. As a consequence, the deposition of particles with rough surfaces increased. With increasing ionic strength, the ionized groups of the surface were compressed, causing the surface to have less roughness. Consequently, the effect of roughness decreased with ionic strength and, as a result, fewer oocysts come to the collector surface. Karaman et al.[69] and Considine et al.[12] showed that *C. parvum* oocysts were quite rough. This rough surface allowed an increase in deposition at low ionic strength. It can be seen in Figure 2.8 that the deposition of *C. parvum* oocysts onto PLL-coated surface decreased with ionic strength because of the decrease of the effect of surface roughness, while the deposition of CML particles onto PLL-coated surface was quite stable because of the lack of effect of surface roughness.

2) Deposition Kinetics of *C. parvum* Oocysts and CML Particles Under repulsive Conditions. It can be seen from Figure 2.8 that k_d for *C. parvum* oocysts onto SRNOM increased with ionic strength from 1 mM to 20 mM NaCl, and then stabilized. For *C. parvum* oocysts on quartz surface, k_d also increased with ionic strength, but did not stabilize until 100 mM NaCl. Similarly, k_d for CML particles onto SRNOM increased with ionic strength from 10 mM to 30 mM NaCl, and then reached the limitation of the deposition rate coefficient. And k_d for CML particles on quartz surface increased with ionic strength from 20 mM to 100 mM NaCl, and then reached the limitation of the deposition rate coefficient.

As shown in Figure 2.9A, the attachment efficiency of *C. parvum* oocysts onto SRNOM-coated silica surface increased with ionic strength from 0.03 at 1 mM NaCl to 0.62 at 20 mM NaCl, and reached stabilization (CDC was between 10-20 mM). The attachment efficiency of *C. parvum* oocysts onto quartz surface (Figure 2.9C) increased with ionic strength from 0.06 at 10 mM NaCl to 0.57 at 100 mM NaCl (CDC was between 60-100 mM, which was higher than that onto SRNOM-coated silica surface). The attachment efficiencies of CML particles onto SRNOM-coated silica surface (Figure 2.9B) increased with ionic strength from 0.03 at 10 mM NaCl to 0.58 at 30 mM NaCl (CDC was between 20-30 mM). The attachment efficiencies of CML particles onto quartz surface (Figure 2.9D) increased with ionic strength from 0.14 at 20 mM NaCl to 0.73 at 100 mM NaCl (CDC was between 60-100 mM NaCl).

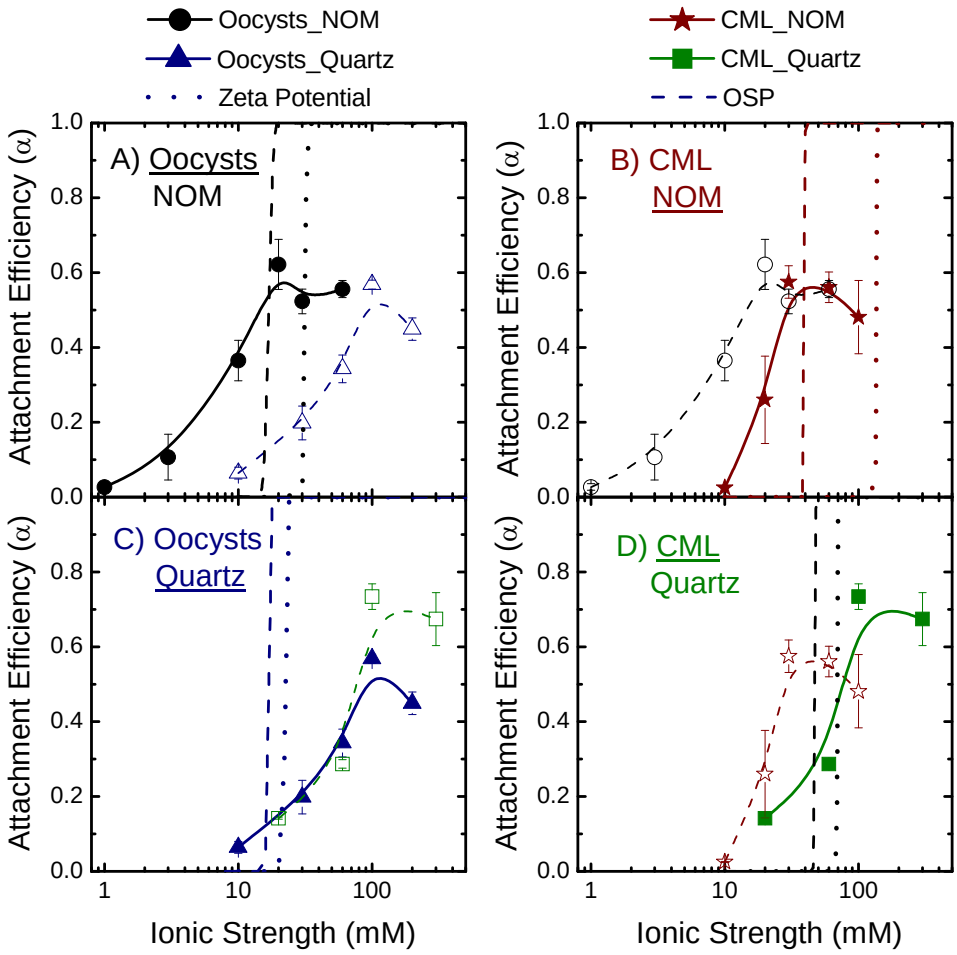

Figure 2.9 Experimental and DLVO-predicted attachment efficiencies for *C. parvum* oocysts and CML particles onto SRNOM-coated silica and quartz surfaces. Open symbols represent the same particle-collector system with solid symbols. They were repeated for comparison between different systems. We used only zeta potential for quartz surface and either zeta potential (dotted lines) or outer surface potential (dashed lines) for other surfaces. Experimental conditions were as follows: capillary flow rate of 1 mL/min (average velocity = 0.0053 m/s with Re = 5.29), pH 5.6 - 5.8, and temperature of 25 ºC.

Deposition Mechanisms of *C. parvum* Oocysts in the RSPF System. The knowledge of particle-collector interactions based on DLVO theory and of the hydrodynamic conditions of the RSPF system allows us to obtain the numerical solution for a convective-diffusion equation describing particle deposition at primary minima in the RSPF system. Particle deposition was shown in terms of the attachment efficiency (α). The numerical solution gave the theoretical values of the attachment efficiency (α) based on DLVO theory for particle-collector interactions. DLVO theory was applied to predict deposition kinetics of *C. parvum* oocysts and CML particles.

The predicted results were compared to experimental data and shed light on the factors influencing the interactions between particles and collector surfaces.

1) Compare Experimental and Predicted Deposition Kinetics of *C. parvum* Oocysts and CML Particles. We compared theoretical attachment efficiency predicted by DLVO theory (dotted lines when zeta potential was used and dashed lines when outer surface potential was used) to experimental attachment efficiency (solid lines) in Figure 2.9. As shown in Figure 2.9A and 2.9B, the DLVO-predicted CDCs of *C. parvum* oocysts and CML particles onto SRNOM-coated surface are 35 and 150 mM NaCl when zeta potential is used and 20 and 40 mM NaCl when outer surface potential is used. Compared to our experimental CDCs (10-20 mM NaCl for *C. parvum* oocysts deposited onto SRNOM-coated surface and 20-30 mM NaCl for CML particles deposited onto SRNOM-coated surface), using outer surface potential resulted in better CDC predictions than zeta potential for oocyst or CML particle deposition on SRNOM-coated surface. The zeta potential theory was developed for hard surfaces, while the Ohshima model was developed for soft surfaces with a penetrable polyelectrolyte surface layer.[61, 68] Thus for deposition on softer collector such as SRNOM-coated surface, the use of zeta potential may not be adequate.

Nevertheless, the DLVO-predicted CDCs of *C. parvum* oocysts and CML particles onto quartz surface (Figure 2.9C and 2.9D) were significantly under-predicted regardless of whether zeta potential or outer surface potential was used. As shown in Figure 2.9C and 2.9D, DLVO-predicted CDCs were 15 or 20 mM for oocyst deposition and 45 or 70 mM for CML particle deposition when outer surface potential or zeta potential was used. However, the experimental CDCs were 100 mM for oocyst deposition and 100 mM for CML particle deposition. Similar results[44, 62] have reported that the DLVO-predicted CDC is usually much lower than experimental values for many particle varieties on quartz surface.

As shown in the experimental deposition curves in Figure 2.9, the attachment efficiency increased gradually within a large range of ionic strength (*C. parvum* oocysts-SRNOM system: 1 to 30 mM NaCl; *C. parvum* oocysts-quartz system: 10 to 100 mM NaCl; CML-SRNOM system: 10 to 20 mM NaCl and CML-quartz system: 20 to 100 mM NaCl). In contrast, the DLVO-predicted attachment efficiency increased rapidly to deposition limitation within a significant short range of ionic strength. The deposition was under-predicted at low ionic strength. The

reason for under-prediction was that the theoretical solution did not account for deposition at secondary minima and surface charge heterogeneity.

Moreover, as shown in Figure 2.9, the highest values of experimental attachment efficiency varied from 0.6 to 0.7, while the expected values based on DLVO-predicted deposition were 1. The deposition was over-predicted at high ionic strength, probably because of steric interactions between particles and collectors. In Chapter 3, oocyst surface macromolecules will be modified with proteinases to study the influence of steric interactions.

The deviation between experimental and theoretically predicted deposition kinetics suggested that DLVO theory, which considers only electrostatic interactions and van der Waals interactions and assumes charge heterogeneity, is not accurate. In the following sections, we will systematically consider the role of deposition at secondary minima, surface charge heterogeneity and steric interaction.

2) Role of Secondary Minima and Microscopic Evidence for Deposition at Secondary Minima. Figure 2.9 shows the deviation between gradually increased experimental attachment efficiency (Figure 2.9, solid symbols) and rapidly increased DLVO-predicted attachment efficiency (Figure 2.9, dashed or dotted lines). Because the theoretical simulation did not include deposition at secondary minima, this deviation suggests the role of secondary minima at low ionic strength. According to the DLVO energy profile, deposition in the primary minimum energy well is irreversible because the attractive interaction between the particle and the surface is strong and a large energy barrier prevents the particles from releasing from the primary minimum energy well. The DLVO energy profile also predicts the presence of the secondary minimum energy wells at larger separation distances. In addition to deposition in primary minima, a large portion of particles can deposit in secondary minima,[41] which increases the attachment efficiency at low ionic strength.

We traced transport and deposition of 24 *C. parvum* oocysts onto SRNOM-coated surface at an ionic strength of 10 mM following the method developed by de Kerchove et al.[44] Deposition of 4 representative oocysts is shown in Figure 2.10. Oocysts, which we traced, deposited onto SRNOM surface and are shown as single dark points marked with numbers. The paths of oocysts are shown as aligned light points linked to the oocysts marked with numbers. Oocyst #1 was deposited with relatively higher velocity, with an average velocity of 15.38 μm/s. Oocyst #2 was deposited, released, deposited again and washed away by the radial flow

eventually. Oocyst #3 was deposited, released and eventually deposited. Oocyst #4 was deposited with relatively lower velocity with an average velocity of 2.16 μm/s. Movies that show the deposition of these *C. parvum* oocysts are provided via internet.

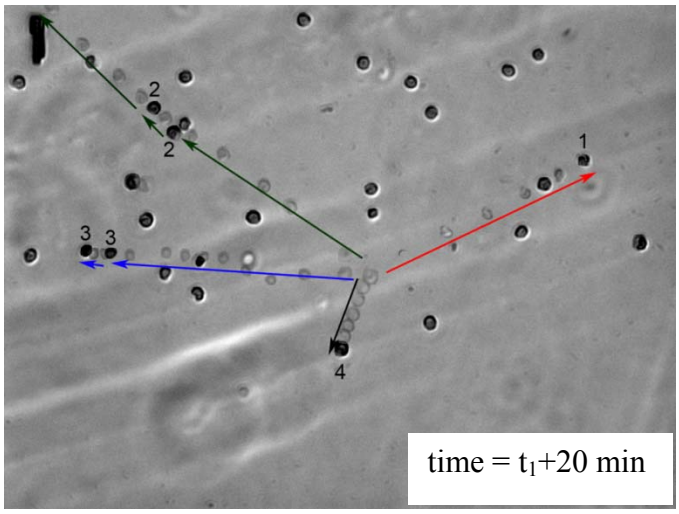

Figure 2.10 Microscopic observation of *C. parvum* oocyst deposition on SRNOM-coated surface in secondary minima at 10 mM ionic strength. The image shown is a composite image generated by superimposing successive pictures taken over 20 min. Pictures were taken every second over the course of 30 min. Not all pictures were superimposed for clarity. *C. parvum* oocysts, which we traced, deposited onto SRNOM surface and appear as single dark points marked with numbers. The paths of traced *C. parvum* oocysts are shown as light aligned points linked to the *C. parvum* oocysts marked with numbers. *C. parvum* oocyst #1 deposited with relatively higher velocity, with an average velocity of 15.38 μm/s (it traveled 76.9 μm within 5 seconds); the dark point on its pathway is an oocyst that had already deposited on the SRNOM surface before *C. parvum* oocyst #1 appeared in the view area. *C. parvum* oocyst #2 was deposited 10 seconds after it appeared in the view area (traveling a distance of 90.1 μm), was released after 30 seconds, and deposited again 6 seconds later (traveling a distance of 12.5 μm); eventually it was washed away by the radial flow after 95 seconds. *C. parvum* oocyst #3 was deposited 14 seconds after it appeared in the view area (traveling a distance of 97.4 μm), was released after 93 seconds, and eventually deposited 3 seconds later (traveling a distance of 10.2 μm). *C. parvum* oocyst #4 deposited with relatively lower velocity with an average velocity of 2.16 μm/s (it traveled 30.2 μm within 14 seconds). Experiments were carried out at ambient pH (around pH 5.6-5.8) and a temperature of 25 ºC.

Our observation, shown in Figure 2.10, suggests that *C. parvum* oocysts irreversibly deposited with relatively higher velocity (i.e. similar to oocyst #1) were possibly deposited under primary minimum conditions. Since they were not entrapped in secondary minima, they were likely to maintain high travel speed. *C. parvum* oocysts that deposited and subsequently released (i.e. similar to oocysts #2 and #3) were likely to experience secondary minimum energy conditions for deposition. Because the energy well was shallow, deposition in secondary minima

was reversible. Therefore, *C. parvum* oocysts deposited in secondary minima could be released. In addition, *C. parvum* oocysts deposited in secondary minima could transfer to primary minima and deposit irreversibly (i.e. similar to oocyst #3) as suggested by de Kerchove and Elimelech[44, 55] This transfer from secondary minima to primary minima explains our observation that oocyst #3 was not released when we decreased the ionic strength after the deposition experiment. For those *C. parvum* oocysts that irreversibly deposited with relatively lower velocity (i.e. similar to oocyst #4), we could not differentiate whether they were deposited in primary minima or had first deposited in secondary minima and then transferred to primary minima.

In Figure 2.11 (movie 11), we show *C. parvum* oocysts entrapped in secondary minima on quartz surface at ionic strengths of 10 mM (Figure 2.11A) and 30 mM NaCl (Figure 2.11B). In Figure 2.12 (movie 12), we show CML particles entrapped in secondary minima on SRNOM-coated surface at an ionic strength of 20 mM NaCl (Figure 2.12A) and on quartz surface at an ionic strength of 100 mM NaCl (Figure 2.12B). Pictures were taken every 5 or 15 seconds over 30 min. As shown in Figure 2.11A and Figure 2.12A and 2.12B, *C. parvum* oocysts or CML particles deposited, released and were eventually washed away by the radial flow. In Figure 2.11B we show one *C. parvum* oocyst deposited, released and then eventually deposited. Movies showing the deposition of these particles are provided via internet.

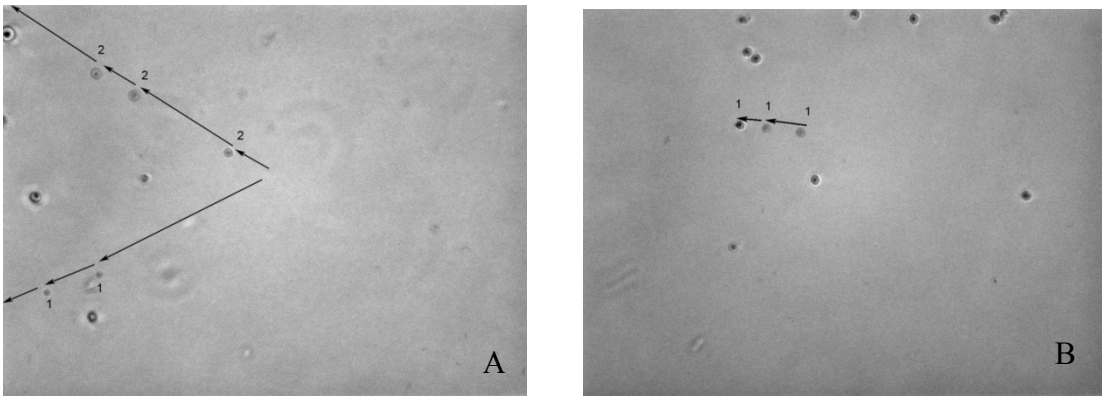

Figure 2.11 Microscopic observation of *C. parvum* oocyst deposition on quartz surface in secondary minima at 10 mM ionic strength over 9 min (A) or at 30 mM ionic strength over 4 min (B). Pictures were taken every 15 seconds over 30 min. Not all pictures were superimposed for clarity. (A) At 10 mM ionic strength, *C. parvum* oocysts were deposited, released, and then deposited and released again before eventually being wiped away by the radial flow. (B) At 30 mM ionic strength, the *C. parvum* oocyst was deposited, released, and then deposited and released again before eventually being deposited one final time. Experiments were carried out at unadjusted pH (5.6-5.8) and a temperature of 25 ºC.

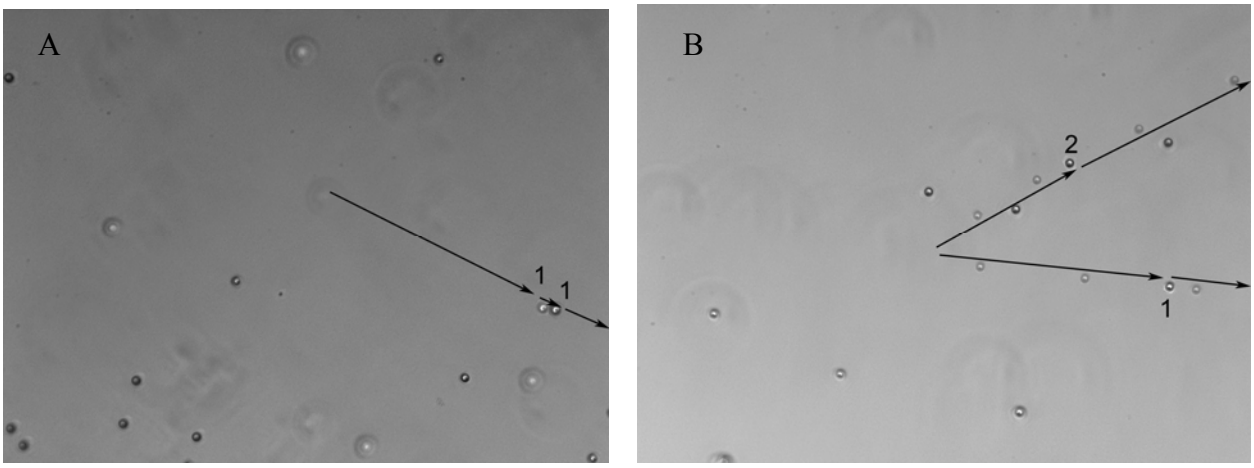

Figure 2.12 Microscopic observation of CML particle deposition on SRNOM-coated surface in secondary minima at 20 mM ionic strength over 2 min (A) and on quartz surface at 100 mM ionic strength over 15 min (B). Pictures were taken every 15 seconds (A) or 5 seconds (B) over 30 min. Not all pictures were superimposed for clarity. (A) At 20 mM ionic strength, the CML particle was deposited, released, and then deposited and released again, until eventually, it was washed away by the radial flow. (B) At 100 mM ionic strength, CML particles were deposited, released, and then eventually wiped away by the radial flow. Experiments were carried out at unadjusted pH (5.6-5.8) and a temperature of 25 ºC.

De Kerchove et al. [44] reported irreversible deposition of CML particles in secondary minima on alginate film, but the lack of this phenomenon on quartz surface. They contributed the irreversible deposition in secondary minima to conditioning film. However, we observed and showed evidence of CML particles deposited in secondary minima on both SRNOM-coated and quartz surfaces. This indicates that conditioning film is not the key to irreversible deposition in secondary minima, although it does help to increase the possibility that particles deposited in secondary minima may transfer to primary minima. The difference between their experiments and ours is probably due to the fact that they worked at a higher flow rate of 4.93 mL/min, while we worked at 1 mL/min. Particles entrapped in secondary minima might not bear the high flow rate, which explains why they did not observe deposition at secondary minima on quartz surface.

We observed a significant number of *C. parvum* oocysts depositing and releasing (i.e. similar to oocysts #2 and #3) at ionic strengths ranging from 3 to 20 mM onto SRNOM-coated surfaces and from 10 to 60 mM onto quartz surfaces. The same phenomena were observed when CML particles deposited at ionic strengths up to 20 mM onto SRNOM-coated surfaces and 300 mM onto quartz surfaces. After the deposition experiment, we shut off the flow of *C. parvum* oocysts or CML particles and pumped in 1 mM NaCl electrolyte. Very few *C. parvum* oocysts and no CML particles were released and washed away by 1 mM NaCl electrolyte from SRNOM-

coated surface at ionic strengths lower than 10 mM NaCl and from quartz surface at ionic strengths lower than 60 mM NaCl. That most of the deposited *C. parvum* oocysts and CML particles were not released as we decreased the ionic strength, indicates that most of the particles deposited in the secondary minimum energy wells had transferred to and irreversibly deposited in the primary minimum energy wells.[8, 42] As shown in Figure 2.7, DLVO theory predicted secondary minimum deposition at ionic strengths lower than CDC. We observed secondary minima for *C. parvum* oocysts onto SRNOM-coated and quartz surface at ionic strengths lower than 20 and 60 mM, and secondary minima for CML onto SRNOM-coated and quartz surface at ionic strengths lower than 20 and 300 mM. This was comparable to experimental CDC values shown in Figure 2.9. In summary, we obtained microscopic evidence for secondary minimum deposition for both *C. parvum* oocysts and CML particles on either quartz or SRNOM surfaces.

3) Role of Surface Charge Heterogeneity. In Figure 2.9, we compared attachment efficiency of *C. Parvum* Oocysts and CML particles onto SRNOM-coated silica and quartz surface. As can be seen in Figure 2.9A and 2.9D, the attachment efficiencies of *C. parvum* oocysts and CML particles onto SRNOM-coated surface were higher than that onto quartz surface at low ionic strength, although electrophoretic mobility of SRNOM-coated surface was more negative than that of quartz surface. This can be explained by surface charge heterogeneity. SRNOM-coated surface was composed of a heterogeneous layer of functional groups such as carboxylate and phenolic.[73] The presence of positively charged area on SRNOM-coated surface increased the chance of particles being deposited onto SRNOM surface.

4) Role of Steric Interaction. As shown in Figure 2.9, the highest values of experimental attachment efficiencies varied from 0.6 to 0.7, while the expected values based on DLVO-predicted deposition were 1. Moreover, as shown in Figure 2.9B and 2.9C, attachment efficiency of *C. parvum* oocysts reached the same deposition limitation ($\alpha = 0.6$) onto both SRNOM-coated and quartz surface at high ionic strength, while the deposition limitation of CML particles onto quartz surface ($\alpha = 0.7$) was higher than that onto SRNOM-coated surface ($\alpha = 0.6$). The energy barrier between CML particles and SRNOM-coated or quartz surface was much higher than that between *C. parvum* oocysts and SRNOM-coated or quartz surface; this prevents CML particle deposition to the surfaces. Thus, the attachment efficiencies of *C. parvum* oocysts on either collector surface should be higher than that of CML particles. It can be seen in Figure 2.9B and 2.9C that the attachment efficiency of *C. parvum* oocysts was higher than that of CML particles

onto SRNOM-coated surface at low ionic strength, which was within expectation. However, the attachment efficiencies of *C. parvum* oocysts and CML particles onto quartz surface were almost the same at low ionic strength, and the attachment efficiency of *C. parvum* oocysts was even lower than that of CML particles onto quartz surface at high ionic strength. This suggests the importance of steric interaction[18, 78] caused by the soft layer on *C. parvum* oocysts, CML particles and SRNOM-coated surface.

Under non-repulsive conditions, there was probably attractive steric interaction caused by bridging between counter-charged groups, while under repulsive conditions, there could be repulsive steric interaction.[79] At high ionic strength conditions, though there was no energy barrier, the effect of steric interaction can still increase or reduce the transport of particles towards the collector surface, which resulted in the attachment efficiency always being less than 1. As shown in Table 2.1, particle electrophoretic softness of *C. parvum* oocysts was 1.23, that of SRNOM-coated surface was 1.10 and that of CML particles was 0.82. Quartz had the least particle electrophoretic softness of 0.03. Because of the strong steric repulsion between *C. parvum* oocysts and SRNOM-coated surface, between *C. parvum* oocysts and quartz surface, and between CML particles and SRNOM-coated surface, the deposition limitations of those systems were only around 0.6. CML particles had less particle electrophoretic softness and quartz barely had any electrophoretic softness. Thus, steric repulsion between CML particles and quartz surface was the smallest and the deposition limitation was higher ($\alpha = 0.7$) than that of other systems. For the same reason, the steric repulsion between *C. parvum* oocysts and quartz surface was larger than that between CML particles and quartz surface, which decreased the deposition of *C. parvum* oocysts onto quartz surface.

However, it is hard to differentiate whether attractive or repulsive steric interaction dominates at high ionic strength when only given the fact that attachment efficiency is always less than 1. But a reasonable guess can be made from the experimental data. In Figure 2.9, we showed that the attachment efficiency of CML particles onto quartz surface was closer to 1 compared to other systems. As we discussed above, steric repulsion between CML particles and quartz surface was the smallest because of the lack in surface coating for quartz substrate and less significant electrophoretic softness of CML particles compared to that of oocysts. This means that when repulsive steric interaction became smaller, the attachment efficiency became closer to 1 and repulsive steric interaction dominated at high ionic strength. This was verified by

the work of de Kerchove et al.[62], which states that the attachment efficiency of silica beads onto quartz surface (system without steric interaction) was close to 1 (0.9 ± 0.07).

2.5 Conclusions

DLVO-predicted deposition kinetics for *C. parvum* oocysts and CML particles onto SRNOM-coated or quartz surface were compared to experimental deposition rates. The experimental CDCs of *C. parvum* oocysts and CML particles onto SRNOM-coated surface were in good agreement with DLVO-predicted CDCs when outer surface potential was used. But the DLVO-predicted CDCs of *C. parvum* oocysts and CML particles onto quartz surface were far off the experimental CDCs. In addition, DLVO under-predicted deposition at low ionic strength and over-predicted at high ionic strength. These discrepancies between DLVO-predicted deposition and experimental deposition were attributed to surface roughness, deposition at secondary minima, surface charge heterogeneity and steric interaction. Specifically, deposition at the secondary minimum energy well and charge heterogeneity led to higher attachment efficiency at low ionic strength, while steric repulsion prevented deposition of oocysts on the collector surface.

Acknowledgement. This work was partially supported by the WaterCAMPWS, The Center of Advanced Materials for the Purification of Water with Systems under the National Science Foundation agreement number CTS-0120978. We acknowledge the financial support of the Department of Civil and Environmental Engineering, University of Illinois, Royal Thai Government Fellowship. We acknowledge Dr. Sharon L. Walker and Dr. Alexis J. de Kerchove for helping us to develop the RSPF system. Deposition and characterization experiments for oocysts and CML particles were conducted by YL and DJ, respectively. Oocysts were purified by TBK. THN and MSK assisted with experimental planning, data interpretation and manuscript preparation.

2.6 References

1. Carey, C. M.; Lee, H.; Trevors, J. T. Biology, persistence and detection of *Cryptosporidium parvum* and *Cryptosporidium hominis* oocyst. *Water Research* **2004,** *38* (4), 818-862.

2. Rose, J. B.; Huffman, D. E.; Gennaccaro, A. Risk and control of waterborne cryptosporidiosis. *Fems Microbiology Reviews* **2002,** *26* (2), 113-123.

3. Hlavsa, M. C.; Watson, J. C.; Beach, M. J. Cryptosporidiosis surveillance --- United States 1999--2002. *Morbility and mortality weekly report* **2005,** *54* (SS01), 1-8.

4. Corso, P. S.; Kramer, M. H.; Blair, K. A.; Addiss, D. G.; Davis, J. P.; Haddix, A. C. Cost of illness in the 1993 waterborne *Cryptosporidium* outbreak, Milwaukee, Wisconsin. *Emerging Infectious Diseases* **2003,** *9* (4), 426-431.

5. Mackenzie, W. R.; Schell, W. L.; Blair, K. A.; Addiss, D. G.; Peterson, D. E.; Hoxie, N. J.; Kazmierczak, J. J.; Davis, J. P. Massive outbreak of waterborne *Cryptosporidium* infection in Milwaukee, Wisconsin - Recurrence of illness and risk of secondary transmission. *Clinical Infectious Diseases* **1995,** *21* (1), 57-62.

6. Fox, K. R.; Lytle, D. A. Milwaukee's crypto outbreak: Investigation and recommendations. *Journal of the American Water Works Association* **1996,** *88* (9), 87-94.

7. Tufenkji, N.; Dixon, D. R.; Considine, R.; Drummond, C. J. Multi-scale *Cryptosporidium*/sand interactions in water treatment. *Water Research* **2006,** *40* (18), 3315-3331.

8. Tufenkji, N.; Elimelech, M. Spatial distributions of *Cryptosporidium oocysts* in porous media: Evidence for dual mode deposition. *Environmental Science & Technology* **2005,** *39* (10), 3620-3629.

9. Tufenkji, N.; Miller, G. F.; Ryan, J. N.; Harvey, R. W.; Elimelech, M. Transport of *Cryptosporidium oocysts* in porous media: Role of straining and physicochemical filtration. *Environmental Science & Technology* **2004,** *38* (22), 5932-5938.

10. Considine, R. F.; Dixon, D. R.; Drummond, C. J. Laterally-resolved force microscopy of biological microspheres-oocysts of *Cryptosporidium parvum*. *Langmuir* **2000,** *16* (3), 1323-1330.

11. Considine, R. F.; Dixon, D. R.; Drummond, C. J. Oocysts of *Cryptosporidium parvum* and model sand surfaces in aqueous solutions: an atomic force microscope (AFM) study. *Water Research* **2002,** *36* (14), 3421-3428.

12. Considine, R. F.; Drummond, C. J.; Dixon, D. R. Force of interaction between a biocolloid and an inorganic oxide: Complexity of surface deformation, roughness, and brushlike behavior. *Langmuir* **2001,** *17* (20), 6325-6335.

13. Bradford, S. A.; Bettahar, M. Straining, attachment, and detachment of *Cryptosporidium oocysts* in saturated porous media. *Journal of Environmental Quality* **2005,** *34* (2), 469-478.

14. Dai, X.; Boll, J.; Hayes, M. E.; Aston, D. E. Adhesion of *Cryptosporidium parvum* and *Giardia lamblia* to solid surfaces: the role of surface charge and hydrophobicity. *Colloids and Surfaces B-Biointerfaces* **2004,** *34* (4), 259-263.

15. Kim, S. B.; Corapcioglu, M. Y. Analysis of *Cryptosporidium parvum* oocyst transport in porous media. *Hydrological Processes* **2004,** *18* (11), 1999-2009.

16. Kuczynska, E.; Shelton, D. R.; Pachepsky, Y. Effect of bovine manure on *Cryptosporidium parvum* oocyst attachment to soil. *Applied and Environmental Microbiology* **2005,** *71* (10), 6394-6397.

17. Kuznar, Z. A.; Elimelech, M. Adhesion kinetics of viable *Cryptosporidium parvum* oocysts to quartz surfaces. *Environmental Science & Technology* **2004,** *38* (24), 6839-6845.

18. Kuznar, Z. A.; Elimelech, M. Role of surface proteins in the deposition kinetics of *Cryptosporidium parvum* oocysts. *Langmuir* **2005,** *21* (2), 710-716.

19. Kuznar, Z. A.; Elimelech, M. *Cryptosporidium* oocyst surface macromolecules significantly hinder oocyst attachment. *Environmental Science & Technology* **2006,** *40* (6), 1837-1842.

20. Logan, A. J.; Stevik, T. K.; Siegrist, R. L.; Ronn, R. M. Transport and fate of *Cryptosporidium parvum* oocysts in intermittent sand filters. *Water Research* **2001,** *35* (18), 4359-4369.

21. Hijnen, W. A. M.; Brouwer-Hanzens, A. J.; Charles, K. J.; Medema, G. J. Transport of MS2 phage, *Escherichia coli*, *Clostridium perfringens*, *Cryptosporidium parvum* and *Giardia intestinalis* in a gravel and a sandy soil. *Environmental Science & Technology* **2005,** *39* (20), 7860-7868.

22. Characklis, G. W.; Dilts, M. J.; Simmons, O. D.; Likirdopulos, C. A.; Krometis, L. A. H.; Sobsey, M. D. Microbial partitioning to settleable particles in stormwater. *Water Research* **2005,** *39* (9), 1773-1782.

23. Searcy, K. E.; Packman, A. I.; Atwill, E. R.; Harter, T. Association of *Cryptosporidium parvum* with suspended particles: Impact on oocyst sedimentation. *Applied and Environmental Microbiology* **2005,** *71* (2), 1072-1078.

24. Dai, X. J.; Hozalski, R. M. Effect of NOM and biofilm on the removal of *Cryptosporidium parvum* oocysts in rapid filters. *Water Research* **2002,** *36* (14), 3523-3532.

25. Marly, X.; Chevalier, S.; Bues, M.; Schwartzbrod, J.; Estevenon, O. Experimental investigations and numerical modelling of *Cryptosporidium parvum* transport behaviour in aquifers. *Water Science and Technology* **2001,** *43* (12), 109-116.

26. Shaw, K.; Walker, S.; Koopman, B. Improving filtration of *Cryptosporidium*. *Journal of the American Water Works Association* **2000,** *92* (11), 103-+.

27. Harter, T.; Wagner, S.; Atwill, E. R. Colloid transport and filtration of *Cryptosporidium parvum* in sandy soils and aquifer sediments. *Environmental Science & Technology* **2000,** *34* (1), 62-70.

28. Bradford, S. A.; Tadassa, Y. E.; Pachepsky, Y. Transport of *Giardia* and manure suspensions in saturated porous media. *Journal of Environmental Quality* **2006,** *35* (3), 749-757.

29. Ramirez, N. E.; Sreevatsan, S. Development of a sensitive detection system for *Cryptosporidium* in environmental samples. *Veterinary Parasitology* **2006,** *136* (3-4), 201-213.

30. Brusseau, M. L.; Oleen, J. K.; Santamaria, J.; Cheng, L.; Orosz-Coghlan, P.; Chetochine, A. S.; Blanford, W. J.; Rykwalder, P.; Gerba, C. P. Transport of microsporidium *Encephalitozoon* intestinales spores in sandy porous media. *Water Research* **2005,** *39* (15), 3636-3642.

31. Darnault, C. J. G.; Steenhuis, T. S.; Garnier, P.; Kim, Y. J.; Jenkins, M. B.; Ghiorse, W. C.; Baveye, P. C.; Parlange, J. Y. Preferential flow and transport of *Cryptosporidium parvum* oocysts through the vadose zone: Experiments and modeling. *Vadose Zone Journal* **2004,** *3* (1), 262-270.

32. Darnault, C. J. G.; Garnier, P.; Kim, Y. J.; Oveson, K. L.; Steenhuis, T. S.; Parlange, J. Y.; Jenkins, M.; Ghiorse, W. C.; Baveye, P. Preferential transport of *Cryptosporidium parvum* oocysts in variably saturated subsurface environments. *Water Environment Research* **2003,** *75* (2), 113-120.

33. McGechan, M. B.; Lewis, D. R. Transport of particulate and colloid-sorbed contaminants through soil, part 1: General principles. *Biosystems Engineering* **2002,** *83* (3), 255-273.

34. Brush, C. F.; Ghiorse, W. C.; Anguish, L. J.; Parlange, J. Y.; Grimes, H. G. Transport of *Cryptosporidium parvum* oocysts through saturated columns. *Journal of Environmental Quality* **1999,** *28* (3), 809-815.

35. Brookes, J. D.; Antenucci, J.; Hipsey, M.; Burch, M. D.; Ashbolt, N. J.; Ferguson, C. Fate and transport of pathogens in lakes and reservoirs. *Environment International* **2004,** *30* (5), 741-759.

36. Abudalo, R. A.; Bogatsu, Y. G.; Ryan, J. N.; Harvey, R. W.; Metge, D. W.; Elimelech, M. Effect of ferric oxyhydroxide grain coatings on the transport of bacteriophage PRD1 and *Cryptosporidium parvum* oocysts in saturated porous media. *Environmental Science & Technology* **2005,** *39* (17), 6412-6419.

37. Byrd, T. L.; Walz, J. Y. Interaction force profiles between *Cryptosporidium parvum* oocysts and silica surfaces. *Environmental Science & Technology* **2005,** *39* (24), 9574-9582.

38. Byrd, T. L.; Walz, J. Y. Investigation of the interaction force between *Cryptosporidium parvum* oocysts and solid surfaces. *Langmuir* **2007,** *23* (14), 7475-7483.

39. Hsu, B. M.; Huang, C. P.; Pan, J. R. Filtration behaviors of *Giardia* and *Cryptosporidium* - Ionic strength and pH effects. *Water Research* **2001,** *35* (16), 3777-3782.

40. Dai, X. J.; Hozalski, R. M. Evaluation of microspheres as surrogates for *Cryptosporidium parvum* oocysts in filtration experiments. *Environmental Science & Technology* **2003,** *37* (5), 1037-1042.

41. Hahn, M. W.; Abadzic, D.; O'Melia, C. R. Aquasols: On the role of secondary minima. *Environmental Science & Technology* **2004,** *38* (22), 5915-5924.

42. Redman, J. A.; Walker, S. L.; Elimelech, M. Bacterial adhesion and transport in porous media: Role of the secondary energy minimum. *Environmental Science & Technology* **2004,** *38* (6), 1777-1785.

43. Walker, S. L. The role of nutrient presence on the adhesion kinetics of *Burkholderia cepacia* G4g and ENV435g. *Colloids and Surfaces B: Biointerfaces* **2005,** *45* (3-4), 181-188.

44. de Kerchove, A. J.; Weronski, P.; Elimelech, M. Adhesion of nonmotile Pseudomonas aeruginosa on "soft" polyelectrolyte layer in a radial stagnation point flow system: Measurements and model predictions. *Langmuir* **2007,** *23* (24), 12301-12308.

45. Yang, J. L.; Bos, R.; Belder, G. F.; Engel, J.; Busscher, H. J. Deposition of oral bacteria and polystyrene particles to quartz and dental enamel in a parallel plate and stagnation point flow chamber. *J. Colloid Interface Sci.* **1999,** *220* (2), 410-418.

46. Walker, S. L.; Redman, J. A.; Elimelech, M. Role of cell surface lipopolysaccharides in *Escherichia coli* K12 adhesion and transport. *Langmuir* **2004,** *20* (18), 7736-7746.

47. Walker, S. L.; Hill, J. E.; Redman, J. A.; Elimelech, M. Influence of frowth phase on adhesion kinetics of *Escherichia coli* D21g. *Applied and Environmental Microbiology* **2005,** *71* (6), 3093-3099.

48. Searcy, K. E.; Packman, A. I.; Atwill, E. R.; Harter, T. Capture and retention of *Cryptosporidium parvum* oocysts by *Pseudomonas aeruginosa* biofilms. *Applied and Environmental Microbiology* **2006,** *72* (9), 6242-6247.

49. Angles, M. L.; Chandy, J. P.; Cox, P. T.; Fisher, I. H.; Warnecke, M. R. Implications of biofilm-associated waterborne *Cryptosporidium* oocysts for the water industry. *Trends in Parasitology* **2007,** *23* (8), 352-356.

50. Ryan, J. N.; Elimelech, M.; Ard, R. A.; Harvey, R. W.; Johnson, P. R. Bacteriophage PRD1 and silica colloid transport and recovery in an iron oxide-coated sand aquifer. *Environmental Science & Technology* **1999,** *33* (1), 63-73.

51. Ryan, J. N.; Harvey, R. W.; Metge, D.; Elimelech, M.; Navigato, T.; Pieper, A. P. Field and laboratory investigations of inactivation of viruses (PRD1 and MS2) attached to iron oxide-coated quartz sand. *Environmental Science & Technology* **2002,** *36* (11), 2403-2413.

52. Zhuang, J.; Jin, Y. Virus retention and transport as influenced by different forms of soil organic matter. *Journal of Environmental Quality* **2003,** *32* (3), 816-823.

53. Yuan, B.; Pham, M.; Nguyen, T. H. Deposition kinetics of bacteriophage MS2 on a silica surface coated with natural organic matter in a radial stagnation point flow cell. *Environmental Science & Technology* **2008,** *42* (20), 7628-7633.

54. Tufenkji, N.; Elimelech, M. Deviation from the classical colloid filtration theory in the presence of repulsive DLVO interactions. *Langmuir* **2004,** *20* (25), 10818-10828.

55. Kuznar, Z. A.; Elimelech, M. Direct microscopic observation of particle deposition in porous media: Role of the secondary energy minimum. *Colloids and Surfaces a-Physicochemical and Engineering Aspects* **2007,** *294* (1-3), 156-162.

56. Johnson, J. K.; Schmidt, J.; Gelberg, H. B.; Kuhlenschmidt, M. S. Microbial adhesion of *Cryptosporidium parvum* sporozoites: Purification of an inhibitory lipid from bovine mucosa. *Journal of Parasitology* **2004,** *90* (5), 980-990.

57. Elimelech, M.; O'Melia, C. R. Effect of particle size on collision efficiency in the deposition of Brownian particles with electrostatic energy barriers. *Langmuir* **1990,** *6* (6), 1153-1163.

58. Nguyen, T. H.; Chen, K. L. Role of divalent cations in plasmid DNA adsorption to natural organic matter-soated silica surface *Environmental Science & Technology* **2007,** *41*.
59. Nguyen, T. H.; Elimelech, M. Adsorption of plasmid DNA to a natural organic matter-coated silica surface: Kinetics, conformation, and reversibility. *Langmuir* **2007,** *23* (6), 3273-3279.
60. Medrzycka, K. B. The effect of particle concentration on zeta potential in extremely dilute solutions *Colloid & Polymer Science* **1991,** *269* (1), 85-90.
61. Ohshima, H. Electrokinetics of soft particles. *Colloid and Polymer Science* **2007,** *285* (13), 1411-1421.
62. de Kerchove, A. J.; Elimelech, M. Relevance of electrokinetic theory for "soft" particles to bacterial cells: Implications for bacterial adhesion. *Langmuir* **2005,** *21* (14), 6462-6472.
63. Ohshima, H. Electrophopretic mobility of soft particles. *Electrophoresis* **1995,** *16* (8), 1360-1363.
64. Hogg, R.; Healy, T. W.; Fuerstenau, D. W. Mutual coagulation of colloidal dispersions. *Transactions of the Faraday Society* **1965,** *62*, 1638-1651.
65. Gregory, J. Approximate expressions for retarded van der waals interaction. *J. Colloid Interface Sci.* **1981,** *83* (1), 138-145.
66. Weronski, P.; Elimelech, M. Novel numerical method for calculating initial flux of colloid particle adsorption through an energy barrier. *J. Colloid Interface Sci.* **2008,** *319* (2), 406-415.
67. Dabros, T.; van de Ven, T. G. M. A direct method for studying particle deposition onto solid surfaces *Colloid & Polymer Science* **1983,** *261* (8), 694-707.
68. Ohshima, H. Electrophoretic mobility of soft particles. *J. Colloid Interface Sci.* **1994,** *163* (2), 474-483.
69. Karaman, M. E.; Pashley, R. M.; Bustamante, H.; Shanker, S. R. Microelectrophoresis of *Cryptosporidium parvum* oocysts in aqueous solutions of inorganic and surfactant cations. *Colloids and Surfaces a-Physicochemical and Engineering Aspects* **1999,** *146* (1-3), 217-225.
70. Sonohara, R.; Muramatsu, N.; Ohshima, H.; Kondo, T. Difference in surface properties between *Escherichia coli* and *Staphylococcus aureus* as revealed by electrophoretic mobility measurements. *Biophysical Chemistry* **1995,** *55* (3), 273-277.

71. Nanduri, J.; Williams, S.; Aji, T.; Flanigan, T. P. Characterization of an immunogenic glycocalyx on the surfaces of *Cryptosporidium parvum* oocysts and sporozoites. *Infection and Immunity* **1999,** *67* (4), 2022-2024.

72. Harris, J. R.; Petry, F. *Cryptosporidium parvum*: Structural components of the oocyst wall. *Journal of Parasitology* **1999,** *85* (5), 839-849.

73. Graczyk, T. K.; Fayer, R.; Knight, R.; Mhangami-Ruwende, B.; Trout, J. M.; Da Silva, A. J.; Pieniazek, N. J. Mechanical transport and transmission of *Cryptosporidium parvum* oocysts by wild filth flies. *American Journal of Tropical Medicine and Hygiene* **2000,** *63* (3-4), 178-183.

74. Hoek, E. M. V.; Bhattacharjee, S.; Elimelech, M. Effect of membrane surface roughness on colloid-membrane DLVO interactions. *Langmuir* **2003,** *19* (11), 4836-4847.

75. Suresh, L.; Walz, J. Y. Effect of surface roughness on the interaction energy between a colloidal sphere and a flat plate. *J. Colloid Interface Sci.* **1996,** *183* (1), 199-213.

76. Adamczyk, Z.; Jaszczolt, K.; Michna, A.; Siwek, B.; Szyk-Warszynska, L.; Zembala, M. Irreversible adsorption of particles on heterogeneous surfaces. *Advances in Colloid and Interface Science* **2005,** *118* (1-3), 25-42.

77. Nazemifard, N.; Masliyah, J. H.; Bhattacharjee, S. Particle deposition onto charge heterogeneous surfaces: Convection-diffusion-migration model. *Langmuir* **2006,** *22* (24), 9879-9893.

78. Elimelech, M. Kinetics of capture of colloidal particles in packed-beds under attractive double-layer interactions. *J. Colloid Interface Sci.* **1991,** *146* (2), 337-352.

79. Rijnaarts, H. H. M.; Norde, W.; Lyklema, J.; Zehnder, A. J. B. DLVO and steric contributions to bacterial deposition in media of different ionic strengths. *Colloids and Surfaces B: Biointerfaces* **1999,** *14* (1-4), 179-195.

CHAPTER 3

COMPOSITION AND CONFORMATION OF *CRYPTOSPORIDIUM PARVUM* OOCYST WALL SURFACE MACROMOLECULES AND THEIR EFFECT ON ADHESION KINETICS OF OOCYSTS ON QUARTZ SURFACE

Published in *Biomacromolecules*, 2010

Liu, Y.; Kuhlenschmidt, M. S.; Kuhlenschmidt, T. B.; Nguyen, T. H. Composition and Conformation of *Cryptosporidium parvum* Oocyst Wall Surface Macromolecules and Their Effect on Adhesion Kinetics of Oocysts on Quartz Surface, *Biomacromolecules*, 11, 2109-2115.

3.1 Abstract

We characterized the composition and conformation of *Cryptosporidium parvum* oocyst wall surface macromolecules and studied their effect on interactions between *C. parvum* oocyst and quartz surface. Proteinase K and mixed glycosidases were used to modify *C. parvum* oocyst surface macromolecules. The peptides released by proteinase K and carbohydrates hydrolyzed by mixed glycosidases were respectively analyzed with liquid chromatography/nano-electrospray ionization tandem mass spectrometry (LC-MS/MS) and phenol-sulfuric acid assay to determine the composition of *C. parvum* oocyst wall surface macromolecules. Surface potential and polarity of the untreated and proteinases treated *C. parvum* oocysts revealed information about the conformation of oocyst wall surface macromolecules. The results illustrated that *C. parvum* oocyst wall is covered by a fluffy layer of glycoprotein. Adhesion kinetics of untreated and proteinase K treated *C. parvum* oocysts on quartz surface were studied in a radial stagnation point flow (RSPF) cell over a wide range of ionic strength (IS) to investigate the effect of *C. parvum* oocyst wall surface macromolecules on oocysts/quartz interactions. The adhesion rate coefficients of proteinase K treated *C. parvum* oocysts significantly decreased compared to that of untreated oocysts. This observation indicated that the fluffy layer on *C. parvum* oocysts wall leads to weaker van der Waals interaction and stronger steric repulsion.

3.2 Introduction

C. parvum is a protozoan pathogen that breaks out each year all over the world and causes cryptosporidiosis, a severe diarrhea, among mammals including humans. Cryptosporidiosis is life-threatening for infants and immunocompromised people because of the lack of effective therapy. Though *C. parvum* cannot achieve its life cycle without a host, the oocysts may survive in harsh environments for several months and are widely spreading in aquatic environments due to their protective wall. The oocyst wall plays a critical role on oocyst transport and survival in both intracellular and extracellular developing stages. The composition and conformation of oocyst wall macromolecules interfere with oocyst transport in the aquatic environment.[1, 2] Moreover, the knowledge about the composition of oocyst wall macromolecules is essential for developing biosensor for detection of *C. parvum* oocysts in water.[3] Therefore, it is of great value to identify the composition and conformation of *C. parvum* oocyst surface macromolecules and study the effect of surface macromolecules on oocyst interaction with solid surfaces.

Electron micrographs[4] revealed that *C. parvum* oocyst wall has a suture lined up to one-third to one-half of the wall which allows the release of sporozoites. The *C. parvum* oocyst wall is composed of four layers.[4] The inner layer is a filamentous glycoprotein layer of thickness of 20 nm. Outside the inner layer is a complex central layer of 10 nm glycolipid/lipoprotein. Outside the central layer is an electron-transparent layer of 5 nm thick. The outer layer is commonly acknowledged as a filamentous layer of carbohydrate rich glycocalyx.[4, 5]

Silicon is the second most abundant element on earth after oxygen and is most commonly found as sand or silica/quartz in nature. Interaction between *C. parvum* oocysts and silica surface has been widely studied at different scales ranging from atomic force microscopy (AFM)[6-10] to RSPF system[1, 2, 11, 12] to packed column.[13-16] These studies showed that interactions between oocyst and silica surface could be explained by steric interaction in addition to classic Derjaguin-Landau-Verwey-Overbeek (DLVO) interactions, i.e., electrostatic interaction and van der Waals interaction. These interactions were essentially controlled by oocyst wall surface macromolecules.[1, 2, 10, 11] Specifically, Kuznar et al.[1] treated oocysts with formalin, heat, or proteinase K and reported that surface macromolecules hindered deposition of *C. parvum* oocysts on quartz surface.

In this work, we aimed to characterize the composition and conformation of oocyst surface macromolecules and study the effect of oocyst surface macromolecuels on oocyst

deposition. Quartz surface was selected as a model surface because it is abundant in nature and widely used as substrate for biosensor. The information in this paper is expected to provide knowledge about the oocyst surface properties and a rough measurement of Hamaker constant of oocyst-water-quartz system which are critical in understanding oocyst life stage, developing biosensor and predicting oocysts transport in subsurface environment.

3.3 Materials and Methods

***C. parvum* Oocysts Preparation.** Male Holstein calves were repeatedly infected with *C. parvum* oocysts (4-5 μm in diameter). The feces were collected and used to isolate viable *C. parvum* oocysts. Prepared oocysts were soaked in a mixture of Hanks' balanced salt and antibiotic-antimycotic solution (HBSS) at 4 °C. Details of the protocol were given in our previous publication.[11, 17]

Before each experiment, the mixture of HBSS and antibiotic-antimycotic solution was removed by centrifugation (Eppendorf centrifuge 5415D) at 13,000 rpm for 2 min. Oocysts were resuspended in deionized water and then washed twice by centrifugation. The cleaned oocysts were then suspended in electrolyte according to the experiment conducted. A hemocytometer (Hausser Scientific, Cat. No. 3100) was used to count the number concentration of oocysts.

Modification of *C. parvum* Oocyst Surface Macromolecules. Pepsin (Sigma, P6887), proteinase K (Sigma, P2308) and mixed glycosidases (Glycosidases, Mixed, Turbo cornutus, USBiological, G8180-10 and Neuraminidase, Roche Applied Science, 10269611001) were used to modify oocyst surface macromolecules. Pepsin exclusively cleaves after the N-terminal of aromatic amino acids. Proteinase K is an unspecified aggressive enzyme[18] that is capable of cleaving the peptide bond adjacent to amino acids of which the alpha amino groups are blocked. Given time, the proteins will be degraded to free amino acids by proteinase K. Glycosidase is used to accelerate hydrolysis of glycosidic linkage and produce smaller carbohydrates. A mixture of different types of glycosidases that allowed an aggressive digestion was used in treatment.

Oocysts were separately treated by pepsin, proteinase K or mixed glycosidases and sequentially treated by proteinase K followed by mixed glycosidases. Oocysts were incubated at 260 rpm in buffers containing proteinases. The incubation conditions are listed in Table 3.1. Treated oocysts were pelleted and washed twice by deionized water to stop the modification. Then, discontinuous cesium chloride density centrifugation was applied to separate intact oocysts

from broken ones. The centrifugation protocol was slightly modified from established protocol published by Current.[19] The CsCl gradient solutions were with reflective indexes of 1.3500, 1.3465, and 1.3440. Oocysts were centrifuged at 20,537 G for 65 min at 4 °C using a pre-cooled ultracentrifuge (L8-M Ultracentrifuge, SW 55 3320, Beckman). The intact oocysts were collected and washed twice by deionized water for further study.

Table 3.1 Proteolysis Experimental Conditions

Proteinase	Oocysts concentration (#/mL)	Proteinase concentration	pH	T (°C)	Incubate time (hr)
Pepsin	2×10^8	2 mg/mL Pepsin	6	27	2.5
Mixed Glycosidases	2×10^8	100 mg/mL GMT, 0.1 U/mL Neuraminidase[1]	6	27	12
Proteinase K	2×10^8	1 mg/mL Proteinase K[2]	8	29	3
Proteinase K followed by Mixed Glycosidases	2×10^8	1 mg/mL Proteinase K[2]	8	29	3
	1×10^8	33.3 mg/mL GMT, 0.2 U/mL Neuraminidase[1]	6	27	16

[1]Glycosidases, Mixed, Turbo cornutus (GMT) and Neuraminidase in 0.25 mg/mL PBS buffer at pH 6
[2]Proteinase K in 10 mM Tris buffer and 1 mM $CaCl_2$ at pH 8

Red-fluorescent Nucleic Acid Stain. Propidium iodide (Invitrogen, P1304MP) stain was used to verify overall integrity of treated oocysts. Propidium iodide is a membrane impermeable fluorescent dye that is capable of staining DNA. Only damaged oocysts can be stained by propidium iodide and appear red under fluorescence microscope. 3×10^4 oocysts were incubated in the dark for 15 min in 30 μL solution with 0.012 mM propidium iodide, 0.06 % dimethyl sulfoxide (DMSO, Fisher, AA42780AK) and 30% PBS (Sigma, D5652). Then, 8 μL of the stained oocyst suspension was placed between a slide and an 18 mm square cover slip. Oocysts were observed under fluorescence microscope (ZEISS Axioskop) with wavelength of 490/635 nm. Fraction of broken oocysts was determined by counting the number of oocysts under fluorescence for every 100 oocysts under normal light.

LC-MS/MS Spectrometry. We used a mild digestion recipe to prepare the peptide samples for LC-MS/MS analysis to prevent the release of sporozoite peptides and the degradation of peptides to free amino acids. Oocysts with concentration of 2×10^8 oocysts/mL were incubated in 1 mL 20 μg/mL proteinase K (Roche Applied Science, 3115836001) at 37 °C

for 1 hr. After incubation, peptides in the supernatant were purified and concentrated by Perfect-FOCUS^{TM} kit (Gbiosciences, 786-124T) following the manufacturer's instruction. The final products were dissolved in 50 μL of 5% acetonitrile with 0.1% formic acid. The sample was analyzed with high-performance liquid chromatography/nano-electrospray ionization tandem mass spectrometry (LC-MS/MS, Waters nanoAcquity UPLC apparatus and Waters Q-ToF mass spectrometer) and filtering was set to eliminate proteinase K spectra. The spectra were identified with MASCOT.

Phenol-Sulfuric Acid Assay. Supernatant of proteinase incubation solution was used for phenol-sulfuric acid assay. Before the assay, TCA (trichloroacetic acid, Fisher, BP555-250) protein precipitation was conducted to remove protein and peptides from the sample. Briefly, 15 μL TCA was added to 60 μL sample. The samples were then incubated at 1-4 ºC for 10 min and spun for 5 min. 50 μL of the supernatant were taken out and the amount of disassociated carbohydrates in the supernatant were detected by phenol-sulfuric acid assay modified from Masuko's method.[20] Glucose was used to plot the standard curve. The samples were measured at 490 nm with a plate reader (Molecular Devices, SpectraMax Plus384) following Masuko's method. To calculate the amount of carbohydrates disassociated from oocysts surface, the amount of carbohydrates from the sample containing only proteinases were subtracted from the amount of carbohydrates from the sample containing both proteinases and oocysts.

Microbial Adhesion to Hydrocarbon Test (MATH). Partitioning of oocysts or bacterial cells between water and dodecane has been used to characterize oocyst and bacterial cell surface hydrophobicity.[1, 21-24] Dodecane, a 12-carbon alkane, is a non-polar hydrocarbon solvent, while water is a polar solvent. Thus, partitioning of oocysts between these two solvents gives an estimate of oocyst surface polarity. 1 mL dodecane was added to 4 mL 30 mM NaCl containing oocysts with a concentration of 2×10^6 #/mL. The sample was vortexed for 2 min and sat still for 15 min to allow phase separation. Then, 1 mL of the aqueous phase was taken out and the number of oocysts was counted by hemocytometer. Each experiment was repeated 3 times. The polarity of oocysts was estimated by the fraction of oocysts in dodecane.

Static Sessile Drop Contact Angle Measurement and Surface Energy. Contact angle of diiodomethane on the quartz, PLL, or oocyst surface was measured to calculate the Lifshitz-van der Waals (LW) component of surface energy (γ^{LW}).[25, 26] A 5 μL diiodomethane droplet was placed on a layer of quartz, PLL, or oocysts surface and contact angle was measured by a sessile

drop method using a Goniometer (KSV Instruments, CAM 200). Each surface was measured 12 times. The average is calculated after eliminating the maximum and the minimum measurements. The oocyst layer was prepared by a method modified from Wan and Wilson.[27] A few drops of highly concentrated oocysts were placed on a glass slide. A layer of dried oocysts was formed after 1 hour in highly ventilated clean room. Contact angle was measured immediately before the oocysts layer began to crack.

γ^{LW} was deduced from the contact angle with following equation:[25, 26]

$$\left(1+\cos\theta\right)\gamma_{di}^{TOT} = 2\sqrt{\gamma_s^{LW}\gamma_{di}^{LW}} \tag{3.1}$$

where θ is contact angel, γ_s^{LW} is γ^{LW} of quartz, PLL or oocyst surface, γ_{di}^{LW} is γ^{LW} of diiodomethane and γ_{di}^{TOT} is total surface energy of diiodomethane. LW component of free energy of adhesion (ΔG_{y0}^{LW}) between oocyst and quartz or PLL surface in the presence of water was calculated from γ^{LW} :

$$\Delta G_{y0}^{LW} = 2\left(\gamma_l^{LW} - \gamma_s^{LW}\right)\left(\gamma_c^{LW} - \gamma_l^{LW}\right) \tag{3.2}$$

where γ_c^{LW} is γ^{LW} of oocyst, γ_l^{LW} is γ^{LW} of water and γ_s^{LW} is γ^{LW} of quartz or PLL. Then Hamaker constant (A), a critical parameter to calculate van der Waals interaction, was determined:

$$A = -12\pi y_0^2 \Delta G_{y0}^{LW} \tag{3.3}$$

where y_0 is minimum equilibrium cut-off distance[25] which is usually assigned a value of 0.157 nm.

Surface Potentials. A Zetasizer Nano analyzer (Malvern Instruments Ltd) was used to determine the electrophoretic mobilities of oocysts, quartz, and PLL-coated silica surfaces under a range of ionic strengths (1 to 200 mM NaCl) at ambient pH (pH 5.6-5.8) at 25 °C. Untreated or treated oocysts were suspended in desirable NaCl solution with the particle concentration of 2×10^6 #/mL. Pulverized quartz cover slip particles were suspended in desirable NaCl solutions and sonicated for 1 h. Then 3 mL of the supernatant containing quartz particles was used to measure electrophoretic mobilities. PLL-coated silica particles were prepared by soaking 1.2×10^8 clean commercial silica particles (1.6 μm in diameter, Bangslab, SS04N-6950) in 1 mL of PLL/HEPES solution for 24 h. The coated silica particles were removed from the PLL/HEPES

solution by centrifugation and rinsed with deionized water. Prepared PLL-coated silica particles were suspended in desirable NaCl solution with concentration of 2×10^6 particles/mL and used to measure electrophoretic mobility. The quality of the measurement was controlled based on the measurement repeatability.

Kinetics of *C. parvum* Oocyst Adhesion. A RSPF system was used to check the effect of proteinase modification on oocysts adhesion and to study the adhesion kinetics of untreated and treated oocysts on quartz and PLL surfaces over a range of ionic strengths (1 to 200 mM NaCl) at ambient pH (pH 5.6-5.8) at 25 °C. A square quartz cover slip (19×19×0.5 mm, TED PELLA) was used as the unfavorable collector surface of the RSPF system. Glass-bottom Petri dishes coated with Poly-L-lysine (PLL, average molecular weight of 150 000, Sigma, P1274) was used as the favorable collector surface of the RSPF system. The preparation of collector surface was followed the method described in our previous publication.[11] The oocysts concentration used in the deposition experiment was 2×10^6 oocysts/mL. A constant flow of 1 mL/min was induced by a syringe pump (Series 74900, Cole-Parmer). Details of the RSPF system, adhesion experiment process, image analysis, and adhesion rate coefficient (k_d) calculation were described in our previous work.[11] Adhesion efficiency (α) was determined as the ratio between k_d under unfavorable conditions and k_d under favorable condition at a given ionic strength.

The attachment efficiency was also simulated by numerically solving the convective-diffusion equation for particle deposition flux using the method described by Weronski and Elimelech and de Kerchove et al.[28, 29] The interaction force used in the convective-diffusion equation was calculated by DLVO theory, the sum of electrostatic interaction and van der Waals interaction, following Hogg et al.[30] expression and retarded van der Waals interaction for particle-plate model.[31]

3.4 Results and Discussion

Integrity and Shape of Untreated and Proteinase Treated *C. parvum* Oocysts. Red-fluorescent nucleic acid stain showed that 50-70% oocysts were damaged by proteolysis. Specifically, only 40-50% oocysts remained intact after proteinase K treatment and 30% oocysts remained intact after sequential treatment by proteinase K and mixed glycosidases. Discontinuous cesium chloride density centrifugation was applied to remove damaged oocysts

after proteinase treatment, and after purification 95% oocysts were intact. In addition, as shown in Figure 3.1, intact oocysts remained roughly spherical before and after proteinase K treatment.

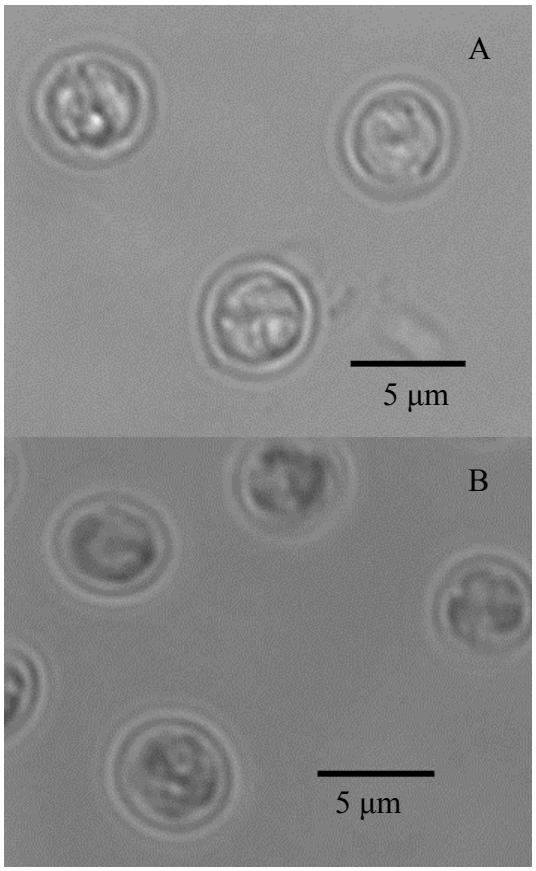

Figure 3.1 Intact *C. parvum* oocysts before (A) and after (B) proteinase K treatment. Images were taken with microscope (ZEISS Axioskop) under magnitude of 40× under visible light.

Surface Composition of *C. parvum* Oocysts. The surface composition of *C. parvum* oocyst wall was studied by analyzing disassociated peptides and carbohydrate released during proteinase K and mixed glycosidases treatments.

LC-MS/MS analysis showed sf-assembling; low complexity protein associated with *C. parvum* Iowa II was detected in the supernatant of proteinase K treated oocyst suspension with a MASCOT score of 19. Other nine proteins associated with *C. parvum* including glycoprotein and extracellular membrane associated protein were matched with lower MASCOT scores. Peptides, which either had a MASCOT score[32] of at least 10 or represented known mitochondrial proteins,[33] were chosen to further estimate the polarity of the peptides. The polarity and charge

of the side chain of each amino acid were reported by Cooper et al.[34] Of all the side chains of the amino acids of the chosen peptides, 53% was polar and 47% was non-polar.

Phenol-sulfuric acid assay was used to detect the disassociated carbohydrate at each step when conducting sequential treatment by proteinase K and mixed glycosidases. The carbohydrate released from oocysts was 7.5×10^{-8} μg/oocyst during proteinase K treatment and 9.7×10^{-6} μg/oocyst during glycosidase treatment. Nanduri et al.[5] reported a similar yield of carbohydrates from *C. parvum* oocyst surface treated with phenol (40 μg/2×10^{7} oocysts).

Surface Polarity of *C. parvum* Oocysts and Other Substrata. MATH test was used to roughly estimate the change in polarity of *C. parvum* oocyst surface after each step of sequential treatment by proteinase K and mixed glycosidases. Particles with higher surface polarity inclined to partition into polar solvent. Specifically, 39% of the untreated oocysts and 22% of the proteinase K treated oocysts were distributed in dodecane, a non-polar solvent, over 30 mM NaCl as shown in Figure 3.2. Similar percentages of untreated *C. parvum* oocysts (39%) and proteinase K treated *C. parvum* oocysts (21%) in dodecane were reported by Kuznar et al.[1] It is further shown in Figure 3.2 that the distribution of oocysts in dodecane decreased after each proteinase treatment step. Thus, the MATH test results showed that the oocyst surface became more polar after each digestion step.

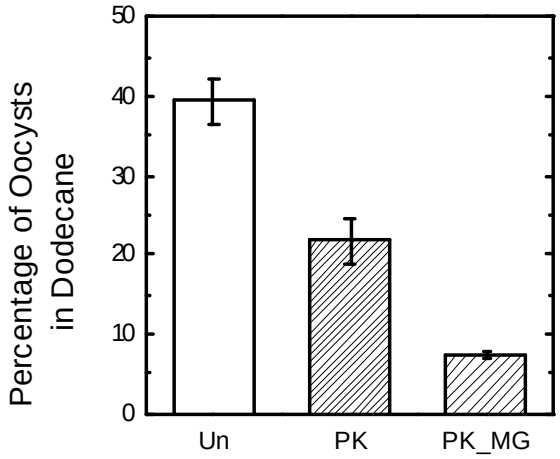

Figure 3.2 Percentage of oocysts distributed in dodecane over water with 30 mM NaCl. Oocysts concentration is 2×10^{-6} #/mL. Dodecane and water ratio is 1:4. Un: untreated oocysts, PK: proteinase K treated oocysts and PK_MG: oocysts sequentially treated by proteinase K and mixed glycosidases.

Besides the MATH test, contact angles were measured to further investigate polarity of the *C. parvum* oocysts and other substrata surfaces. The averaged contact angle of diiodomethane, a non-polar solvent, on the surface of quartz, PLL, untreated oocysts, and proteinase K treated oocysts were shown in Table 3.2. The contact angle of diiodomethane on proteinase K treated oocysts surface (71.8°) was larger than that of the untreated oocysts surface (63.0°). Thus, oocyst surface became more polar after proteinase K digestion. The contact angle results agreed with our observation of the MATH test.

Table 3.2 Contact angle, surface energy and Hamaker constant of the surfaces at 20℃

	$\theta_{diiodomethane}$	$\gamma^{LW}/\Delta G_{y0}{}^{LW}$ (mJ/m^2)	A(J)
Water	-	21.8 [a,b]	4.1×10^{-20} [c]
Diiodomethane	-	50.8 [a,b,d]	9.4×10^{-20} [c]
Quartz	47.7±3.3	35.6 [b]	6.9×10^{-20} [c]
PLL	57.9±2.0	29.8 [b]	5.8×10^{-20} [c]
Untreated oocysts	63.0±2.3	26.9 [b]	5.2×10^{-20} [c]
Proteinase K treated oocysts	71.8±2.6	21.9 [b]	4.3×10^{-20} [c]
Untreated oocyst-water-quartz	-	-1.33 [e]	1.2×10^{-21} [f]
Proteinase K treated oocyst-water-quartz	-	-0.02 [e]	2.3×10^{-23} [f]
Untreated oocyst-water-PLL	-	-0.81 [e]	7.5×10^{-22} [f]
Proteinase K treated oocyst-water-PLL	-	-0.01 [e]	1.4×10^{-23} [f]

[a] Data was from van Oss[25]
[b] γ^{LW}: LW component of surface tension
[c] Hamaker constant across vacuum
[d] $\gamma^{TOT} = \gamma^{LW} = 50.8$ mJ/m^2 for diiodomethane
[e] $\Delta G_{y0}{}^{LW}$: LW component of free energy of adhesion per unit area
[f] Hamaker constant in the presence of water

Surface Electrophoretic Mobility Properties of *C. parvum* Oocysts and Other Substrata. Figure 3.3A and 3.3B showed electrophoretic mobility (EM) and zeta potential (ζ) of quartz surfaces and oocysts at ambient condition (25ºC and pH 5.8-6.0) under ionic strength (IS) ranging from 1 to 200 mM NaCl. Oocysts are negatively charged due to dissociation of surface functional groups at ambient pH condition. ζ of untreated oocysts was -13.0 mV in 1 mM NaCl and -5.3 mV in 100 mM NaCl (Figure 3.3B). Those were within the range of ζ of *C. parvum* oocysts previously reported: between -6 to -42 mV in 1 mM NaCl,[11, 35] -5 mV in 100 mM NaCl[11] and between -1 to -8 mV in 100 mM KCl.[1, 12] ζ of oocysts became less negative after each modification step when oocysts were sequentially treated by proteinase K and mixed glycosidases (Figure 3.3B). The decrease of the absolute value of ζ implied the removal of

functional groups by proteolysis and that the functional groups are overall negatively charged. Karaman et al.[35] suggested that the functional groups were glycoprotein related surface carboxylate groups or phosphate groups. Furthermore, the double layer shielding effect for treated oocysts was observed but not as significant as that of untreated oocysts, and quartz surface.

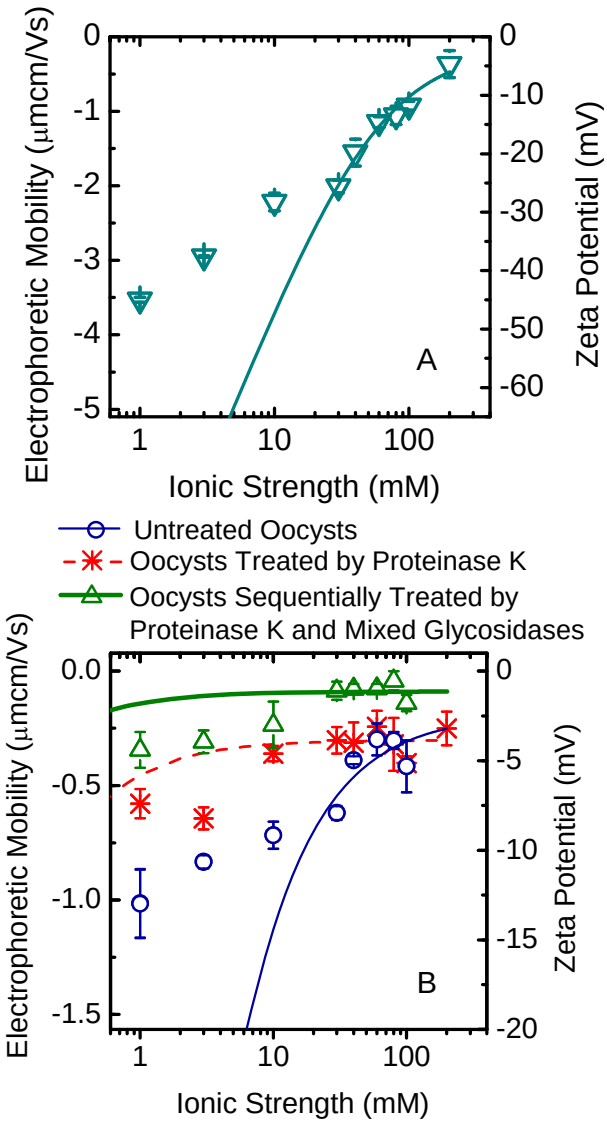

Figure 3.3 A) Electric surface charge properties of quartz surfaces as a function of IS (NaCl) at pH 5.8-6.0. Overlapped open triangles represent experimental electrophoretic mobility and zeta potential calculated by Smoluchowski equation; solid line represents electrophoretic mobility fitted by Ohshima's theory. B) Electric surface charge properties of untreated oocysts (circle), oocysts treated by proteinase K (star) and oocysts sequentially treated by proteinase K then mixed glycosidases (triangle) as a function of IS (NaCl) at pH 5.8-6.0. Overlapped symbols represent experimental electrophoretic mobility and zeta potential calculated by Smoluchowski equation; solid or dash lines represent electrophoretic mobility fitted by Ohshima's theory.

Electrophoretic mobility of untreated and treated oocysts was fitted with Ohshima's theory[36] to study the surface softness of oocysts. Surface softness of quartz was also studied to illustrate the difference between a hard surface and soft surface though Ohshima's theory is not a good model for hard surface such as quartz. We fitted the experimental EM at IS above 30 mM NaCl to determine the value of ZN and $1/\lambda$ since EM of "soft particles" tends to reach a nonzero limitation ($ZeN/\eta\lambda^2$) at high ionic strength (IS) and the limitation value is sensitive to the value of ZN and $1/\lambda$. Fitted values of the uniform charge densities (ZN) and particle electrophoretic softnesses ($1/\lambda$) are listed in Table 3.3. The absolute value of ZN for oocyst surface decreased after each modification step when oocysts were sequentially treated by proteinase K and mixed glycosidases. According to the definition of electrophoretic softness, $1/\lambda \sim \left(a_p N_p\right)^{-1/2}$, softness is a parameter to describe both the the equivalent sphere radius of the polymer segment (a_p) and the density (N_p) of the polymer segment in the polyelectrolyte layer. Softness $1/\lambda$ of treated oocysts is of one order of magnitude higher than the softness of untreated oocysts (11-12 nm vs. 1 nm). This increase in softness suggested that proteolysis hydrolyzed the big macromolecules and loosened the outer layer of the oocyst wall and made it fluffier. The absolute value of ζ of the treated oocysts did not decrease as significantly as untreated oocysts did because the fluffier layer after proteolysis was resistant to the double layer compaction effect. The discrepancy between experimental EM (symbols) and EM fitted by Ohshima's theory (solid lines) of quartz surfaces (Figure 3.3A) and untreated oocysts (Figure 3.3B) was mainly at low IS. This discrepancy was due to the deviation of particle surface structures from the ideal assumptions of Ohshima's model that ionized groups and polymer segments were uniformly distributed inside the surface layer.[11, 36-38]

Table 3.3 Fitted value of the uniform charge density (ZN) and particle electrophoretic softness ($1/\lambda$) within the polyelectrolyte layer determined by Ohshima's theory

Particle	ZN (mM)	$1/\lambda$ (nm)
Quartz	-121.3	0.3
PLL	198.6[11]	0.7[11]
Untreated oocysts	-15.5	1.1
Oocysts treated by proteinase K	-0.2	11.9
Oocysts orderly treated by proteinase K then glycosidases	-0.1	11.2

Effect of Proteolysis on *C. parvum* Oocysts Adhesion on Quartz Surface. Adhesion rate coefficient (k_d) of proteinases treated oocysts on quartz surface at 30 mM NaCl in RSPF system were compared to that of untreated oocysts (Figure 3.4). k_d of pepsin treated oocysts were the same as untreated oocysts. Treatment with mixed glycosidases slightly increased k_d of oocysts. The value of k_d reduced from 3.1×10^{-8} m/s for untreated to 2.7×10^{-9} m/s for proteinase K treatment. When proteinase K treated oocysts were further sequentially treated by mixed glycosidases, k_d of oocysts increased back to the level similar to that of untreated oocysts. The results showed that proteinase K treatment allowed mixed glycosidases better access to carbohydrates.

Note that Kuznar et al.[1] reported that proteinase-K treatment led to higher deposition of oocysts on quartz surface. Our result of adhesion of proteinase K treated oocysts on quartz surface disagreed with the result of Kuznar et al.[1] mainly because we used a different digestion method and we purified the treated oocysts before using in deposition experiments. We purified the treated oocysts because in our experiments, the sutures of some treated oocysts were open. Broken oocysts due to formalin treatment was also reported by Byrd et al.[10]

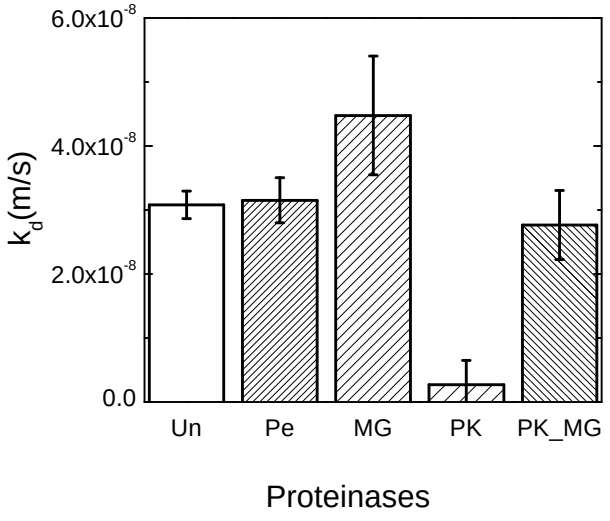

Figure 3.4 Adhesion rate coefficient (kd) of untreated or proteinases treated C. parvum oocysts on quartz surface at 30 mM NaCl at pH 5.8-6.0. Un: untreated oocysts, Pe: pepsin treated oocysts, MG: Mixed glycosidases treated oocysts, PK: proteinase K treated oocysts, and PK_MG: oocysts sequentially treated by proteinase K and mixed glycosidases.

Adhesion Kinetics of Untreated and Proteinase K treated *C. parvum* Oocysts on Quartz Surface: DLVO Interaction. The adhesion kinetics of untreated and proteinase K treated oocysts over a wide range of IS (1 to 200 mM NaCl) were shown in Figure 3.5. The attachment efficiency (α) of untreated oocysts was quite stable above 10 mM NaCl. Even at high IS, α of untreated oocysts was less than 0.2 and was far from unity as predicted by classic DLVO theory under nonrepulsive condition at high IS. α of proteinase K treated oocysts were significantly decreased comparing to that of untreated oocysts and were almost negligible throughout the entire range of IS.

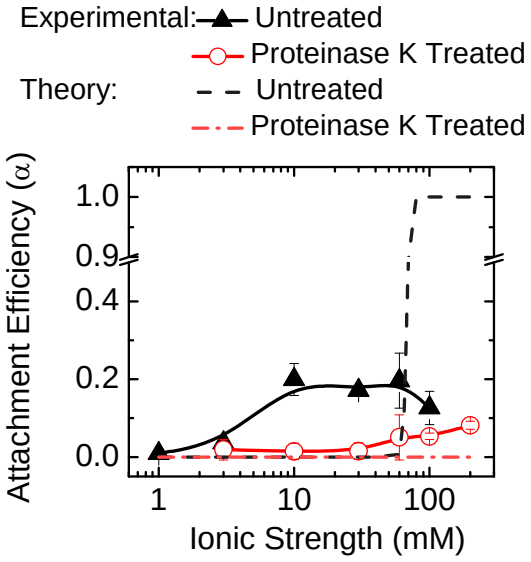

Figure 3.5 Adhesion efficiencies (α) for untreated and proteinase K digested *C. parvum* oocysts on quartz surface. Experimental conditions were as follows: capillary flow rate of 1 mL/min (average velocity = 0.0053 m/s with Re = 5.29), pH 5.6 - 5.8, and temperature of 25 ºC.

The classic DLVO theory of colloidal interactions includes only van der Waals interaction and double-layer interaction.[39] ζ was used to calculate DLVO energy profile. van der Waals interaction was calculated from Hamaker constant, and Hamaker constant of oocyst-water-quartz/PLL system was calculated from LW component of free energy of adhesion and was listed in Table 3.2.

Figure 3.6 shows the DLVO energy profiles of untreated/proteinase K treated oocyst-water-quartz system. Based on DLVO interaction, theoretical α was predicted by solving convective-diffusion equation (Figure 3.5, dash/dash-dot lines). DLVO theory predicted critical

deposition concentration (CDC) of 60 mM NaCl for untreated oocysts-water-quartz system (Figure 3.6A). Theoretical α based on DLVO interaction was correspondingly increased (Figure 3.5, black dash line) at IS of 60 mM NaCl and progressed to unity, at 75 mM NaCl. However, experimental data (Figure 3.5) showed a maximum deposition at 10 mM NaCl. More importantly, the maximum observed α was only 0.2. This number was far from unity which was expected when only van der Waals interaction and double-layer interaction are counted. The lower observed IS value of maximum deposition than CDC and lower observed α at IS higher than CDC compared to those predicted theoretically implied the existence of secondary minimum energy well and non-DLVO interactions.

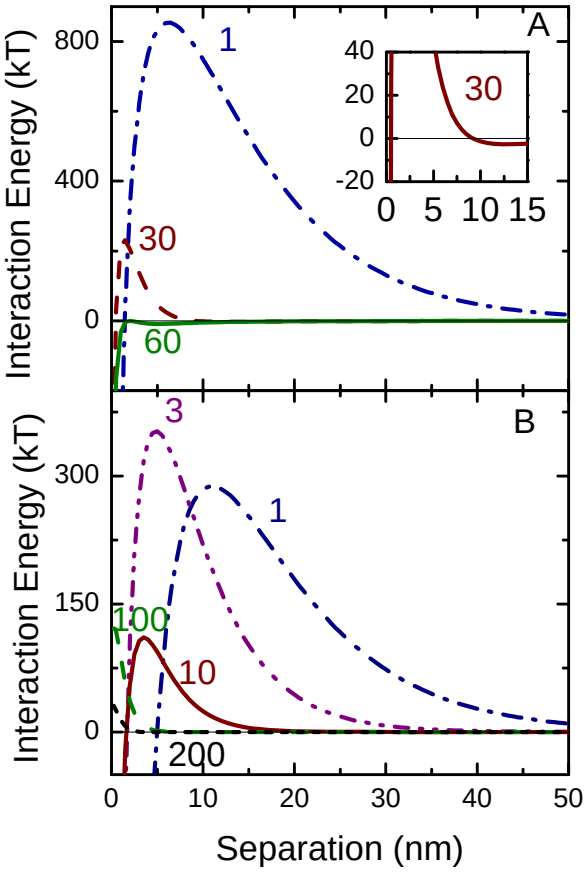

Figure 3.6 DLVO interaction energy profiles between quartz and untreated *C. parvum* oocysts (A) or proteinase K treated *C. parvum* oocysts (B) in NaCl solution. Numbers next to lines are ionic strength of NaCl solution.

DLVO theory predicted energy barrier of proteinase K treated oocyst-water-quartz system (Figure 3.6B) over the entire studied range of IS because the repulsive double layer interaction overwhelmed van der Waals forces over a wider range of separation distance and IS. On the basis of DLVO interaction, theoretical α (Figure 3.5, red dash-dot line) remained extremely low at all IS. This was exactly in line with our experimental observation (Figure 3.5). As shown in Table 3.2, Hamaker constant for proteinase K treated oocyst-water-quartz system (2.3×10^{-23}) was two orders of magnitude smaller than that of untreated oocyst-water-quartz (1.2×10^{-21}) system. van der Waals interaction is proportional to Hamaker constant.[40] Therefore van der Waals interaction was extremely weak and the range of van der Waals interaction is unusually short for proteinase K treated oocysts-water-quartz system which resulted in decrease of α at the same IS compare to that of untreated oocysts.

Table 3.2 listed γ^{LW} of each solvent and surface, ΔG_{y0}^{LW} between oocysts and collector surfaces, and Hamaker constant (A) of surfaces across vacuum or water. Israelachivili[40] reported similar Hamaker constant for water (3.7, 4.0×10^{-20} J) and fused quartz (6.5×10^{-20} J) that confirmed our calculation. Nir et al.[41] reported Hamaker constant of cell surfaces between 8×10^{-22} and 6×10^{-21} J in agreement with our measurement of Hamaker constants for untreated oocyst-water-quartz system (1.2×10^{-21}) and untreated oocyst-water-PLL system (7.5×10^{-22}). Standard nonretarded Lifshitz theory[40] shows that Hamaker constant of colloid-water-collector system decreases when dielectric constant of colloids increases or when refractive index of colloids decreases. Moreover, Nir et al.[41] reported that Hamaker constant was mainly controlled by the cell surface coating layer rather than the plasma membrane below the coating layer. Previous studies[42, 43] reported higher dielectric constant due to more polar substance or lower sugar concentration. Similarly, other studies[44, 45] showed lower refractive index of protein or polysaccharide solution as a result of lower protein or polysaccharide concentration. MATH test and contact angle measurements showed that proteinase K treated oocysts were more polar than untreated oocysts. Lager electrophoretic softness, i.e. $1/\lambda \sim \left(a_p N_p\right)^{-1/2}$ of proteinase K treated oocysts suggested a lower concentration of glycocalyx. Those facts indicated that proteinase K treated oocysts had higher dielectric constant and lower refractive index and consequently indicated a smaller Hamaker constant and weaker van der Waals interaction.

In addition, as shown in Figure 3.5, experimental α was greater than DLVO predicted α at low IS. The attractive van der Waals interaction dominated at large separation (greater than 10

nm); the repulsive double layer interaction turned out to be dominating at modest separation at low IS (e.g., from 2 nm to 100 nm at 1 mM NaCl and from 2 nm to 10 nm at 30 mN NaCl). As shown in the magnified profile at 30 mM NaCl in Figure 3.6 A, the dominating van der Waals interaction at larger separation resulted in secondary minimum energy well and enhanced the transport of oocysts towards the surface.

Adhesion Kinetics of Untreated and Proteinase K treated *C. parvum* Oocysts on Quartz Surface: Non-DLVO Interactions. The fact that α of untreated oocysts was far from unity even at high IS suggests the existence of non-DLVO interactions. Typical non-DLVO interactions include steric and hydration interaction. Both of them are essentially repulsive entropic interactions; and the range of those two interactions is from several to 22-24 nm. Therefore, it is impractical to differentiate steric interaction from hydration interaction. Usually, they are treated as steric-hydration force.[40] As we showed before, oocyst surface was covered with a fluffy glycocalyx layer which promoted the steric-hydratio interaction. For this reason, α of untreated oocysts did not reach unity. Treated with proteinase K, this fluffy glycocalyx layer became even fluffier, the steric-hydration interaction was consequently increased, and α of proteinase K treated oocysts was further decreased. The effect of steric interaction was essential not only for proteinase K treated oocysts but also for untreated oocysts. Both Kuznar et al. and our previous studies[11, 12] showed that steric interaction hindered oocyst deposition at high IS. AFM studies of Byrd[9, 10] et al. confirmed the existence of steric interaction caused by oocyst outer polysaccharide layer.

3.5 Conclusions

The results from oocyst surface characterization suggest that composition and conformation of *C. parvum* oocyst surface macromolecules determined the magnitude and range of van der Waals interaction, the double layer interaction, and steric-hydration interaction. Those interactions dominated oocyst deposition behavior at different separation range and IS. Specifically, 1) when the oocyst surface is more negatively charged, the repulsive double layer interaction is greater and acts at greater separation; 2) when the oocyst surface is more polar, the attractive van der Waals interaction is weaker and acts at shorter range; 3) when the oocyst surface is fluffier, the attractive van der Waals interaction is weaker and acts at shorter range, while the repulsive steric-hydration interaction is stronger and acts at longer range.

Acknowledgements. We acknowledge Peter Yau for the peptides analysis conducted at the Roy J. Carver Biotechnology Center of University of Illinois at Urbana-Champaign. This work was partially supported by the WaterCAMPWS, The Center of Advanced Materials for the Purification of Water with Systems under the National Science Foundation agreement number CTS-0120978. We acknowledge the financial support of the Illinois Water Resources Center (grant # USGS 06HQGR0083) and NSF Career grant #0954501.

3.6 References

1. Kuznar, Z. A.; Elimelech, M. *Cryptosporidium* oocyst surface macromolecules significantly hinder oocyst attachment. *Environmental Science & Technology* **2006,** *40* (6), 1837-1842.

2. Kuznar, Z. A.; Elimelech, M. Role of surface proteins in the deposition kinetics of *Cryptosporidium parvum* oocysts. *Langmuir* **2005,** *21* (2), 710-716.

3. Poitras, C.; Fatisson, J.; Tufenkji, N. Real-time microgravimetric quantification of *Cryptosporidium parvum* in the presence of potential interferents. *Water Research* **2009,** *43* (10), 2631-2638.

4. Harris, J. R.; Petry, F. *Cryptosporidium parvum*: Structural components of the oocyst wall. *Journal of Parasitology* **1999,** *85* (5), 839-849.

5. Nanduri, J.; Williams, S.; Aji, T.; Flanigan, T. P. Characterization of an immunogenic glycocalyx on the surfaces of *Cryptosporidium parvum* oocysts and sporozoites. *Infection and Immunity* **1999,** *67* (4), 2022-2024.

6. Considine, R. F.; Dixon, D. R.; Drummond, C. J. Laterally-resolved force microscopy of biological microspheres-oocysts of *Cryptosporidium parvum*. *Langmuir* **2000,** *16* (3), 1323-1330.

7. Considine, R. F.; Drummond, C. J.; Dixon, D. R. Force of interaction between a biocolloid and an inorganic oxide: Complexity of surface deformation, roughness, and brushlike behavior. *Langmuir* **2001,** *17* (20), 6325-6335.

8. Considine, R. F.; Dixon, D. R.; Drummond, C. J. Oocysts of *Cryptosporidium parvum* and model sand surfaces in aqueous solutions: an atomic force microscope (AFM) study. *Water Research* **2002,** *36* (14), 3421-3428.

9. Byrd, T. L.; Walz, J. Y. Interaction force profiles between *Cryptosporidium parvum* oocysts and silica surfaces. *Environmental Science & Technology* **2005,** *39* (24), 9574-9582.

10. Byrd, T. L.; Walz, J. Y. Investigation of the interaction force between *Cryptosporidium parvum* oocysts and solid surfaces. *Langmuir* **2007,** *23* (14), 7475-7483.

11. Liu, Y. Y.; Janjaroen, D.; Kuhlenschmidt, M. S.; Kuhlenschmidt, T. B.; Nguyen, T. H. Deposition of Cryptosporidium parvum Oocysts on Natural Organic Matter Surfaces: Microscopic Evidence for Secondary Minimum Deposition in a Radial Stagnation Point Flow Cell. *Langmuir* **2009,** *25* (3), 1594-1605.

12. Kuznar, Z. A.; Elimelech, M. Adhesion kinetics of viable *Cryptosporidium parvum* oocysts to quartz surfaces. *Environmental Science & Technology* **2004,** *38* (24), 6839-6845.

13. Tufenkji, N.; Dixon, D. R.; Considine, R.; Drummond, C. J. Multi-scale *Cryptosporidium*/sand interactions in water treatment. *Water Research* **2006,** *40* (18), 3315-3331.

14. Tufenkji, N.; Elimelech, M. Spatial distributions of *Cryptosporidium oocysts* in porous media: Evidence for dual mode deposition. *Environmental Science & Technology* **2005,** *39* (10), 3620-3629.

15. Tufenkji, N.; Miller, G. F.; Ryan, J. N.; Harvey, R. W.; Elimelech, M. Transport of *Cryptosporidium oocysts* in porous media: Role of straining and physicochemical filtration. *Environmental Science & Technology* **2004,** *38* (22), 5932-5938.

16. Dai, X. J.; Hozalski, R. M. Effect of NOM and biofilm on the removal of *Cryptosporidium parvum* oocysts in rapid filters. *Water Research* **2002,** *36* (14), 3523-3532.

17. Johnson, J. K.; Schmidt, J.; Gelberg, H. B.; Kuhlenschmidt, M. S. Microbial adhesion of *Cryptosporidium parvum* sporozoites: Purification of an inhibitory lipid from bovine mucosa. *Journal of Parasitology* **2004,** *90* (5), 980-990.

18. Kraus, E.; Femfert, U. Proteinase K from mold tritirachium-album limber specificity and mode of action. *Hoppe-Seylers Zeitschrift Fur Physiologische Chemie* **1976,** *357* (7), 937-947.

19. Current, W. L., *Techniques and laboratory maintenance of Cryptosporidium*. CRC Press: Boca Raton, Florida, 1990; p 31-49.

20. Masuko, T.; Minami, A.; Iwasaki, N.; Majima, T.; Nishimura, S. I.; Lee, Y. C. Carbohydrate analysis by a phenol-sulfuric acid method in microplate format. *Analytical Biochemistry* **2005,** *339* (1), 69-72.

21. Pembrey, R. S.; Marshall, K. C.; Schneider, R. P. Cell surface analysis techniques: What do cell preparation protocols do to cell surface properties? *Applied and Environmental Microbiology* **1999,** *65* (7), 2877-2894.

22. Chen, G.; Beving, D. E.; Bedi, R. S.; Yan, Y. S.; Walker, S. L. Initial bacterial deposition on bare and zeolite-coated aluminum alloy and stainless steel. *Langmuir* **2009,** *25* (3), 1620-1626.
23. Chen, G. X.; Walker, S. L. Role of solution chemistry and ion valence on the adhesion kinetics of groundwater and marine bacteria. *Langmuir* **2007,** *23* (13), 7162-7169.
24. Kim, H. N.; Hong, Y.; Lee, I.; Bradford, S. A.; Walker, S. L. Surface characteristics and adhesion behavior of *Escherichia coli* O157:H7: Role of extracellular macromolecules. *Biomacromolecules* **2009,** *10* (9), 2556-2564.
25. van Oss, C. J. Acid--base interfacial interactions in aqueous media. *Colloids and Surfaces a-Physicochemical and Engineering Aspects* **1993,** *78*, 1-49.
26. Brant, J. A.; Childress, A. E. Assessing short-range membrane-colloid interactions using surface energetics. *Journal of Membrane Science* **2002,** *203* (1-2), 257-273.
27. Wan, J.; Wilson, J. L. Colloid transport in unsaturated porous media. *Water Resour. Res.* **1994,** *30* (4), 857-864.
28. Weronski, P.; Elimelech, M. Novel numerical method for calculating initial flux of colloid particle adsorption through an energy barrier. *J. Colloid Interface Sci.* **2008,** *319* (2), 406-415.
29. de Kerchove, A. J.; Elimelech, M. Relevance of electrokinetic theory for "soft" particles to bacterial cells: Implications for bacterial adhesion. *Langmuir* **2005,** *21* (14), 6462-6472.
30. Hogg, R.; Healy, T. W.; Fuerstenau, D. W. Mutual coagulation of colloidal dispersions. *Transactions of the Faraday Society* **1966,** *62*, 1638-1651.
31. Gregory, J. Approximate Expressions for Retarded Vanderwaals Interaction. *J. Colloid Interface Sci.* **1981,** *83* (1), 138-145.
32. Koenig, T.; Menze, B. H.; Kirchner, M.; Monigatti, F.; Parker, K. C.; Patterson, T.; Steen, J. J.; Hamprecht, F. A.; Steen, H. Robust prediction of the MASCOT score for an improved quality assessment in mass spectrometric proteomics. *Journal of Proteome Research* **2008,** *7* (9), 3708-3717.
33. Forner, F.; Foster, L. J.; Campanaro, S.; Valle, G.; Mann, M. Quantitative proteomic comparison of rat mitochondria from muscle, heart, and liver. *Molecular & Cellular Proteomics* **2006,** *5* (4), 608-619.
34. Cooper, G. M.; Hausman, R. E., *The cell: A molecular approach* 3rd ed.; Sinauer: 2004; p 51.

35. Karaman, M. E.; Pashley, R. M.; Bustamante, H.; Shanker, S. R. Microelectrophoresis of *Cryptosporidium parvum* oocysts in aqueous solutions of inorganic and surfactant cations. *Colloids and Surfaces a-Physicochemical and Engineering Aspects* **1999,** *146* (1-3), 217-225.

36. Ohshima, H. Electrokinetics of soft particles. *Colloid Polym. Sci.* **2007,** *285* (13), 1411-1421.

37. de Kerchove, A. J.; Weronski, P.; Elimelech, M. Adhesion of nonmotile Pseudomonas aeruginosa on "soft" polyelectrolyte layer in a radial stagnation point flow system: Measurements and model predictions. *Langmuir* **2007,** *23* (24), 12301-12308.

38. Sonohara, R.; Muramatsu, N.; Ohshima, H.; Kondo, T. Difference in surface-properties between *Escherichia-Coli* and *Staphylococcus-Aureus* as revealed by electrophoretic mobility measurements. *Biophysical Chemistry* **1995,** *55* (3), 273-277.

39. Derjaguin, B.; Landau, L. Theory of the stability of strongly charged lyophobic sols and of the adhesion of strongly charged particles in solutions of electrolytes. *Progress in Surface Science* **1941,** *43* (1-4), 30-59.

40. Israelachivili, J. N., *Intermolecular & surface forces*. 2nd ed.; Elsevier Science & Technology Books: 1991.

41. Nir, S.; Andersen, M. Vanderwaals Interactions between cell-surfaces. *Journal of Membrane Biology* **1977,** *31* (1-2), 1-18.

42. Wyman, J. Studies on the dielectric constant of protein solutions: I. Zein. *Journal of Biological Chemistry* **1931,** *90*, 443-476.

43. Malmberg, C. G.; Maryott, A. A. Dielectric constants of aqueous solutions of dextrose and sucrose. *Journal of Research of the National Bureau of Standards* **1950,** *45* (4), 2137-2141.

44. Barer, R.; Tkaczyk, S. Refractive index of concentrated protein solutions. *Nature* **1954,** *173* (4409), 821-822.

45. Greenwood, C. T.; Hourston, D. J. Specific refractive-index increments of certain polysaccharide systems. *Polymer* **1975,** *16* (7), 474-476.

CHAPTER 4
TRANSPORT OF *CRYPTOSPORIDIUM PARVUM* OOCYSTS IN A SILICON MICROMODEL

Published in *Environmental Science & Technology,* 2012

Liu, Y.; Zhang, C.; Hilpert, M.; Kuhlenschmidt, M. S.; Kuhlenschmidt, T. B.; Nguyen, T. H. Transport of *Cryptosporidium parvum* Oocysts in a Silicon Micromodel, *Environmental Science & Technology*, 46, 1471-1479.

4.1 Abstract

Effective removal of *Cryptosporidium parvum* oocysts by granular filtration requires the knowledge of oocyst transport and deposition mechanisms, which can be obtained based on real time microscopic observation of oocyst transport in porous media. Attachment of oocysts to silica surface in a radial stagnation point flow cell and in a micromodel, which has 2-dimensional (2-D) microscopic pore structures consisting of an array of cylindrical collectors, was studied and compared. Real time transport of oocysts in the micromodel was recorded to determine the attached oocyst distributions in transversal and longitudinal directions. In the micromodel, oocysts attached to the forward portion of clean collectors, where the flow velocity was lowest. After initial attachment, oocysts attached onto already attached oocysts. As a result, the collectors ripened and the region available for flow was reduced. Results of attachment and detachment experiments suggest that surface charge heterogeneity allowed for oocyst attachment. In addition to experiments, Lattice-Boltzmann simulations helped understanding the slightly nonuniform flow field and explained differences in attachment in the longitudinal direction.

4.2 Introduction

Cryptosporidium parvum (*C. parvum*), a diarrhea-causing protozoan pathogen, has been a public health concern.[1-3] Oocysts, the resistant stage of *C. parvum*, have been widely found in surface and groundwater.[4, 5] Protecting drinking water resources requires understanding of oocyst

transport and fate in both natural and engineering environments. Since micrometer size oocysts can be effectively removed by granular filtration,[6-8] mathematical models to predict oocyst transport in granular porous media are of interest. Studies ranging from the microscopic to the field scale have been conducted to reveal oocyst transport mechanisms[7-13] as a basis for predictive model development.

Electrostatic interaction, van der Waals interactions, steric repulsion, and cation bridging in the presence of Ca^{2+} have been identified as mechanisms governing oocyst attachment to collector surfaces.[6, 7, 10, 14-16] Besides the electrostatic interaction that controls oocyst attachment by means such as electrostatic screening and surface charge heterogeneity,[7, 15] steric interaction was proposed to explain the observed independence of oocysts' Debye length with ionic strength. Higher deposition of oocysts on silica and natural organic matter (NOM) coated surfaces in Ca^{2+} solution compared to those in Na^{+} solution was observed.[6, 15] In addition, when oocysts were digested with proteinase K to remove carboxylate functional groups, inductive couple plasma (ICP) analysis showed less Ca^{2+} bound to digested oocysts compared to original oocysts.[15] As a result, lower deposition of digested oocysts to NOM-coated surface than that original oocysts was observed.

Packed columns have frequently been used to simulate oocyst transport in porous media. The influence of ionic strength, NOM, and surface charge on oocyst transport has been systematically studied.[8, 9, 17-24] The electrostatic effects have been found to dominate any hydrophobic effect on oocyst transport.[25] Suspended particles associated with oocysts resulted in larger aggregates and enhanced oocyst attachment.[26, 27] Larger grain size and macropores in soil enhance oocyst mobility.[28, 29] Increasing loading rate, which is well correlated with grain size, also enhances oocyst mobilization.[12, 18, 28] In general, ripening changes particle transport through the filter and enhances particle removal.[30-32] Larger particles and the presence of polymers induce faster ripening.[30, 31] Straining and partial release have been frequently reported as important oocyst transport mechanisms.[11, 12, 17, 28]

Some transport mechanisms mentioned above have been incorporated into transport models. For example, a dual mode deposition model was proposed to consider fast and slow oocyst attachment.[9] A continuous time random walk model was used to examine the effects of collector surface physicochemical heterogeneity.[21]

New techniques were developed to visualize colloid transport that allow for real time observation of colloid transport in parallel flow chambers packed with glass beads.[13, 33] Carboxylate-modified latex (CML) particles entrapped in the secondary minimum energy well calculated from DLVO theory were suggested to translate along the collector surface and accumulate near the rear of the collector at pH 11.[33] Colloid-colloid aggregation was driven by funneling of fluid into grain-to-grain contacts at pH 6.7.[13] Recently, columnar morphology attachment and partial breaking were visualized at the collector forward stagnation point at neutral pH in a single cylindrical collector chamber. Attachment to the rear of the collector was observed only under sufficiently high flow rate.[34] Because oocysts have a more complex surface characteristic than latex particles,[10, 14, 16, 35] the remaining question is whether oocyst and latex particles have similar transport behaviors.

Oocyst deposition has often been quantified with the attachment efficiency (α). The Radial Stagnation Point Flow (RSPF) setup has been used to determine attachment efficiency at forward stagnation point.[6, 7] In addition, the average attachment efficiency for packed column was often determined from column breakthrough curves.[9, 17, 36] Large discrepancy between attachment efficiency for RSPF system and column was reported and attributed to attachment in secondary minimum.[36] However, direct observation of oocyst transport in porous media with multiple collectors is currently lacking. Micromodel, a two dimensional (2D) microfluidic device, provides a flexible design of pore network structure and allows direct observation of colloid transport. This device has been used to study flow path, colloids velocity, and the influence of straining, surface roughness and pore-scale on colloids transport.[37, 38] These visualization techniques emphasized the importance of hydrodynamic effects on colloid transport.

In this work, a micromodel was designed to observe oocyst transport in porous media with multiple collectors. The effects of flow field and charge heterogeneity on oocyst transport were studied. Attachment efficiencies were experimentally determined in the micromodel, and compared to those measured with the RSPF setup. Attachment regimes ranged from clean bed filtration to ripening. Experiments with carboxylate modified latex (CML) particles, which have been used as model colloids in previous studies[7-9, 17, 23] were also conducted.

4.3 Materials and Methods

***C. parvum* Oocyst Preparation.** *C. parvum* oocysts (4-5 μm in diameter) were isolated from the feces of an infected male Holstein calf and purified by sieve filtration, Sheather's sugar floatation, and discontinuous cesium chloride density centrifugation. The purified oocysts were stored in a mixture of Hanks' balanced salt and antibiotic-antimycotic solution at 4°C following previously published protocol.[39] No additional treatment was applied to inactivate oocysts. Red-fluorescent nucleic acid stain showed that 95% oocysts were viable. Infection and purification process were conducted in the Department of Pathobiology, UIUC. Procedures related to animals were acted upon protocols approved by the University of Illinois Institutional Animal Care and Use Committee.

Before each experiment, the oocysts were washed twice with deionized water and centrifuged (Eppendorf) at 17000 × g for 2 min. The oocysts were then suspended in desired electrolyte solutions. Oocyst concentration in the suspension was determined by counting with a hemocytometer (Hausser Scientific). All experiments were conducted at room temperature, and the lab temperature was maintained around 22-25 °C. Thermometers were used to monitor the lab temperature.

Micromodel Fabrication. Pore network and inlet/outlet patterns of the micromodel were designed in AutoCAD (Autodesk) and printed onto transparencies by high-resolution printer (5080 dpi). Both patterns were then transferred onto chrome masks and etched into each side of the same silicon wafer through a standard photolithography procedure (described below) in a class 10 cleanroom in UIUC. The silicon wafer used to fabricate micromodel was 100 mm in diameter, 0.5 mm thick and polished on both sides (Virginia Semiconductor). A total of seven micromodels can be fabricated from each wafer. The wafer was first cleaned by deionized water, acetone and isopropyl alcohol (J. T. Baker), and then dried with nitrogen gas. Clean silicon wafer was coated with a thin layer (8 μm thickness) of photoresist (PR) polymer (AZ 4620, AZ Electronic Materials). The pore network pattern on the mask was selectively exposed onto the wafer pre-coated with PR polymer by ultraviolet (UV) light (EVGroup) with wavelength of 405 nm for 25 s. PR exposed to the UV light was weakened and can be removed by a PR developer (AZ 400 K, AZ Electronic Materials). The exposed area was etched to a depth around 22 μm using an inductively coupled plasma-deep reactive ion etching (ICP-DRIE) system

(Plasmatherm). The inlet/outlet pattern was through etched into the wafer on the back side using the same procedure. Next, the wafer was cleaned suing a PR stripper (AZ 400 T, AZ Electronic Materials) at 75 °C, an acid solution (H_2SO_4: H_2O_2 at a ratio of 3:1) at room temperature, and a base solution (deionized water: H_2O_2: NH_4OH at ratio of 5:1:1) at 75 °C. A layer of 0.15 µm silicon dioxide was obtained on the etched wafer surface by thermal dry oxidation. The wafer was again cleaned using base solution and dried by N_2. Finally, the porous media pattern side was sealed by anodically bonding to a Pyrex glass wafer (Sensor Prep Services, 7740) using a bonder (EVGroup). Using a dicing saw (Disco Corporation), the wafer was cut into individual micromodels which were 9.9 mm long and 6.5 mm wide (Figure 4.1). The pore network of each micromodel was formed by 1440 uniformly distributed cylindrical collectors with a diameter of 180 µm and a height of 22 µm. The pore-body and pore throat diameter were 114 µm and 28 µm, respectively. The resulting porosity was 0.41. The diameter of inlet and outlet tubes was 0.8 mm. As shown in the scanning electron microscope (SEM) picture of the micromodel in Figure 4.2, the collectors are macroscopically smooth compared to the size of the oocysts.

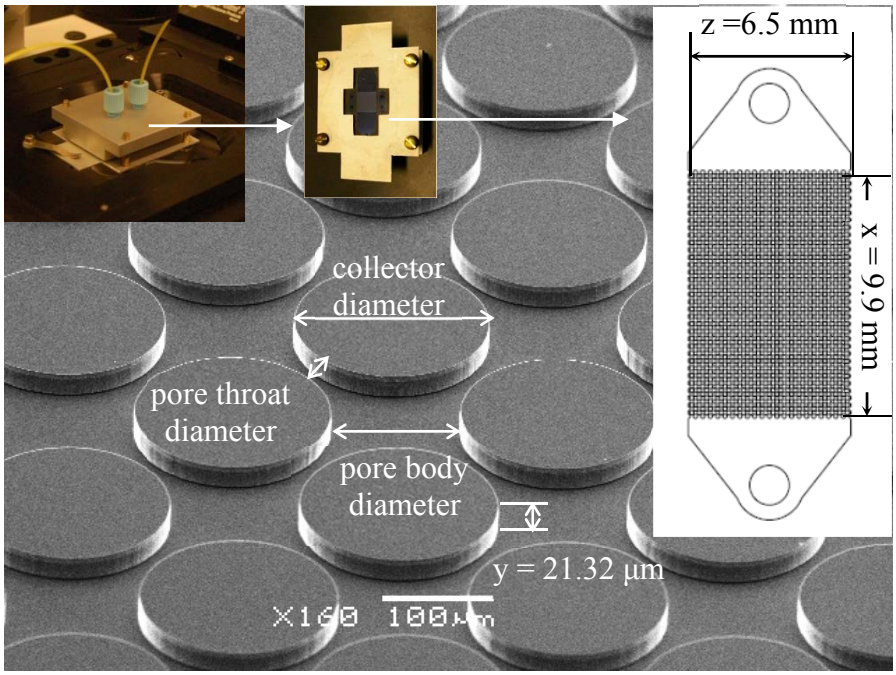

Figure 4.1 Micromodel experiment setup and scanning electron microscope picture of the pore network. Length of pore network: x = 9.9 mm, width of pore network: z = 6.5 mm, height of collector: y = 21.32 µm, collector diameter: 180 µm, pore space diameter: 114.16 µm and pore throat diameter: 28 µm.

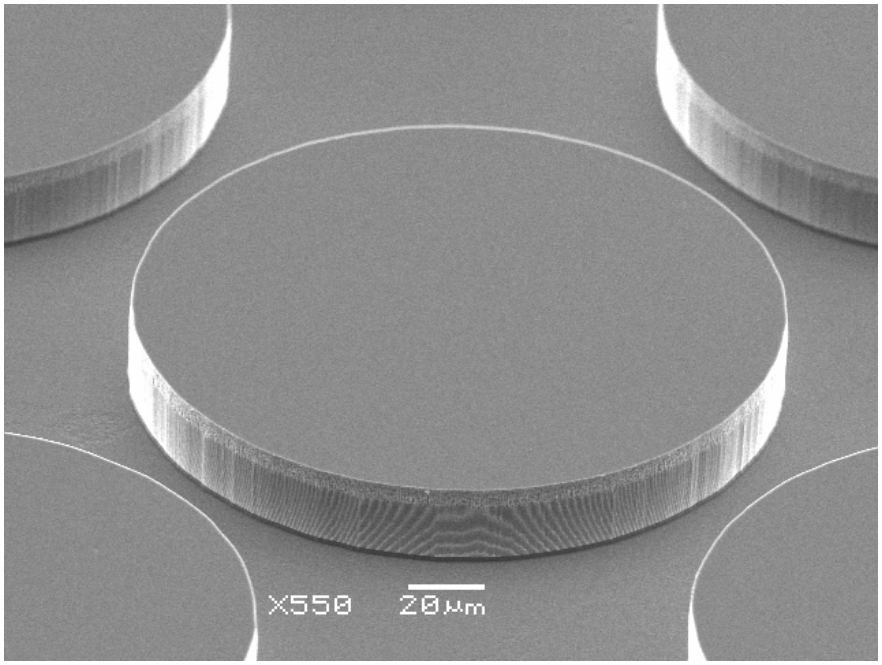

Figure 4.2 Scanning electron microscope picture of the pore network of micromodel.

Surface Potential Measurement. The electrophoretic mobilities of oocysts, oxidized silicon (silica) wafer, and quartz coverslip surfaces were measured by a Zetasizer Nano analyzer (Malvern Instruments) for different solution chemistries and converted to zeta potential using the Smoluchowski equation. Clean silicon wafer was pulverized and dry oxidized in a high temperature furnace (Thermal Technology) to create particles of silicon dioxide surface. The samples were suspended in desirable electrolytes for electrophoretic mobility measurement as described in previous publication.[7] The electrophoretic mobility of carboxylate-modified latex (CML, 5 μm in diameter, 4% w/v, Invitrogen) particles has been studied in our previous publication.[7] These 5-μm CML particles were selected because they are easier to observe in the micromodel and they have similar size as the studied oocysts.

DLVO Energy Profile. The DLVO interaction profiles for oocysts-collector system were calculated as the sum of electrostatic interaction and van der Waals interaction from particle-surface model by Hogg et al.[40] and retarded van der Waals interaction.[41] The equations and parameter engaged are listed (Equation 4.1-4.4). Specifically, the Hamaker constant of oocyst-water-quartz system (1.2×10^{-21} J) was determined previously from contact angle,[35] and was used for the DLVO calculation.

The total interaction energy between charged surfaces was calculated as the sum (ϕ_T) of electrostatic (ϕ_{EDL}) and van der Waals (ϕ_{VDW}) interactions using the Hogg et al. expression[6, 40] and retarded van der Waals interaction equation derived by Gregory.[41]

Equation 4.1 and 4.2 were used to calculate DLVO energy profiles between charged particle (oocyst or CML particle) and plate surface (micromodel or quartz surface in RSPF cell).

$$\phi_{EDL} = \pi\varepsilon_0\varepsilon_r a\left\{2\psi_p\psi_c \ln[\frac{1+\exp(-\kappa H)}{1-\exp(-\kappa H)}] + (\psi_p^2+\psi_c^2)\ln[1-\exp(-2\kappa H)]\right\} \quad (4.1)$$

$$\phi_{VDW} = -\frac{Aa}{6H}\left(\frac{1}{1+14H/\lambda'}\right) \quad (4.2)$$

Equation 4.3 and 4.4 were used to calculate DLVO energy profiles between charged particles (oocyst-oocyst or CML-CML).

$$\phi_{EDL} = \pi\varepsilon_0\varepsilon_r a\psi_p^2\left[\ln\left(\frac{1+\exp(-\kappa H)}{1-\exp(-\kappa H)}\right)+\ln(1-\exp(-2\kappa H))\right] \quad (4.3)$$

$$\phi_{VDW} = -\frac{Aa}{12H}\left(\frac{1}{1+14H/\lambda'}\right) \quad (4.4)$$

where H is the separation distance between particle and the collector surface, ψ_p and ψ_c are the surface potentials of the particle and collector surface, λ' is the characteristic wavelength of the dielectric (assumed to be 100 nm) and A is the Hamaker constant of the interacting medium. The Hamaker constant of oocyst were determined previously from contact angle.[35] We used a Hamaker constant of 1.2×10^{-21} J for oocyst-silica interaction, 4.9×10^{-22} J for oocyst-oocyst interaction, and 1×10^{-20} J for CML-silica and CML-CML interaction, as suggested by Kuznar et al.[6] and de Kerchove et al.,[42] respectively.

Micromodel Experiment. The micromodel was assembled under the microscope (Leica, DMI5000 M) with a reflected differential interference contrast (DIC) (Figure 4.1). Before each experiment, the micromodel was saturated with a desirable electrolyte supplied by a syringe pump (KD Scientific) through 0.18 mm inner diameter Teflon FEP tubing (Upchurch). Next, oocysts with concentration of 1×10^6 oocysts/mL in the desirable electrolyte were pumped into the micromodel. A magnetic stirrer was used to stir the oocyst suspension in the syringe. This concentration was selected to comply with the condition that no oocyst aggregation in the solution was observed during the course of the experiment (i.e., 60 min). The linear velocity was

2.9 mm/s. This is the lowest velocity that the syringe pump can deliver oocysts reliably. This velocity is also the lowest velocity that did not allow a substantial number of oocysts to stick to the wall of the Teflon tubing. Oocyst transport was directly observed at 40X magnification, recorded by a charge-coupled-device (CCD) camera (Qimaging Retiga 2000R Fast 1394), and analyzed with Image Pro 6.2 software. The same experiment was conducted for CML particles with concentration of 1×10^6 CML/mL in 100 mM NaCl at pH 7.0-7.2. Oocysts or CML particles that attached to the 1440 collectors were determined by direct counting.

The average single collector removal efficiency (η) and average attachment efficiency (α) of oocysts were determined after 500 oocysts attached on the whole collectors and before multiple layers of oocysts accumulated on the collectors.[38] Experiments lasted several minutes up to one hour, depending on the solution chemistry. An average η was calculated by counting the number of oocysts attached to a single cylindrical collector and the number of upstream oocysts approaching the cylinder over time.[17]

$$\eta = \frac{I}{DR_c u C_0} \tag{4.5}$$

where I is an average attachment rate of oocysts on one cylindrical collector (I is obtained by dividing the total number of attached oocysts by the product of experimental duration time and the number of collectors), D is the height of the cylinder, R_c is the radius of the cylinder, u is the Darcy velocity, and C_0 is the oocyst concentration. The repulsive condition was created by buffered NaCl electrolytes (pH 7.0-7.2 with 0.05 mM $NaHCO_3$).[17] The favorable attachment condition was created by lowering the pH to 2.5 and fixing the ionic strength to 30 mM NaCl, at which condition the DLVO profile showed no energy barrier.[6] The average attachment efficiency was calculated as the ratio between the average single collector removal efficiencies for repulsive condition (η) and for the favorable condition (η_0). The average attachment efficiency was determined with the micromodels from the same batch.

After each attachment experiment at pH 7.0-7.2, a solution with lower ionic strength (1 mM NaCl) at the same pH and a solution at pH 11 (1 mM NaOH) were sequentially pumped into the micromodel to release oocysts deposited due to secondary minimum energy well and surface charge heterogeneities.[9]

Flow Field Simulation. In order to reveal potential nonuniformity in the nonmeasured 3D flow field in the collector array, we simulated it with the multiple-relaxation-time (MRT)

lattice Boltzmann (LB) model by d'Humieres et al.[43] The simulation was parameterized following methods described in Hilpert.[44] Since the Reynolds number of the real flow was smaller than one, we could perform simulations at a smaller Reynolds number and then scale the simulated velocity field in order to predict the actual one. Using the measured flow rate we scaled the simulated velocity field. Due to CPU time limitations, we reduced the length of the pore network in the flow direction by about a factor of one-half but preserved its width and the region between the inlet supply and the outlet withdrawal tubes and the pore network.

Radial Stagnation Point Flow Setup Experiment. Oocyst attachment efficiency (α) on a square quartz coverslip (19 × 19 × 0.5 mm, Ted Pella) was measured in a RSPF setup. A solution with a concentration of 2×10^6 oocysts/mL was pumped in the RSPF cell at a constant flow rate of 1 mL/min or 5.3 mm/s linear velocity. This is the lowest velocity that did not lead to particle suspension in the middle of the RSPF. Similar or higher velocity has been used in previous studies.[6, 10, 16, 33, 36] The oocyst concentration was selected so that there was detectable oocyst attachment on the quartz surface at low ionic strength, and at the same time no oocyst aggregation in the suspension was observed. Similar to the micromodel experiments, the oocyst suspension was stirred continuously. More details of the experiment setup, experimental process, image analysis, and deposition rate coefficient (k_d) calculation can be found in previous publication.[7] Attachment efficiency was determined as the ratio between k_d under repulsive conditions at pH 7.0-7.2 and k_d under favorable condition at pH 2.5.[6]

4.4 Results and Discussion

Electrokinetic Properties of Oocysts, Silica Wafer, and Quartz Surfaces. Zeta potential of oocysts, silica wafer, and quartz surfaces as a function of ionic strength (NaCl, pH 7.0-7.2) are shown in Figure 4.3A. All substrate surfaces were negatively charged and became less negative with increasing ionic strength. Zeta potential for oocysts was -4.1 mV in 1 mM NaCl and -2.4 mV in 200 mM NaCl, similar as in previous reports: -5 to -1 mV in Ca^{2+} at pH 6.7.[24] Oocyst zeta potential was less sensitive to ionic strength compared to those for other surfaces and has been attributed to the resistance of a fluffy glycocalyx layer on oocyst surface to double layer compression effect.[35] Zeta potential of silica wafer surface was slightly more negative than that of quartz surface. Zeta potential of oocysts, silica wafer, and quartz surfaces at

30 mM NaCl, pH 2.5 were 0.3, 2.4 and 0.6 mV, which were near zero. DLVO profile shows no energy barrier between oocysts and collector surfaces under these conditions. Therefore, electrostatic conditions favorable for attachment were approximately achieved at pH 2.5.[6] Zeta potential of oocysts and silica wafer were -9.6 and -71.3 mV at pH 11 at which surface charge heterogeneity was reduced.[9]

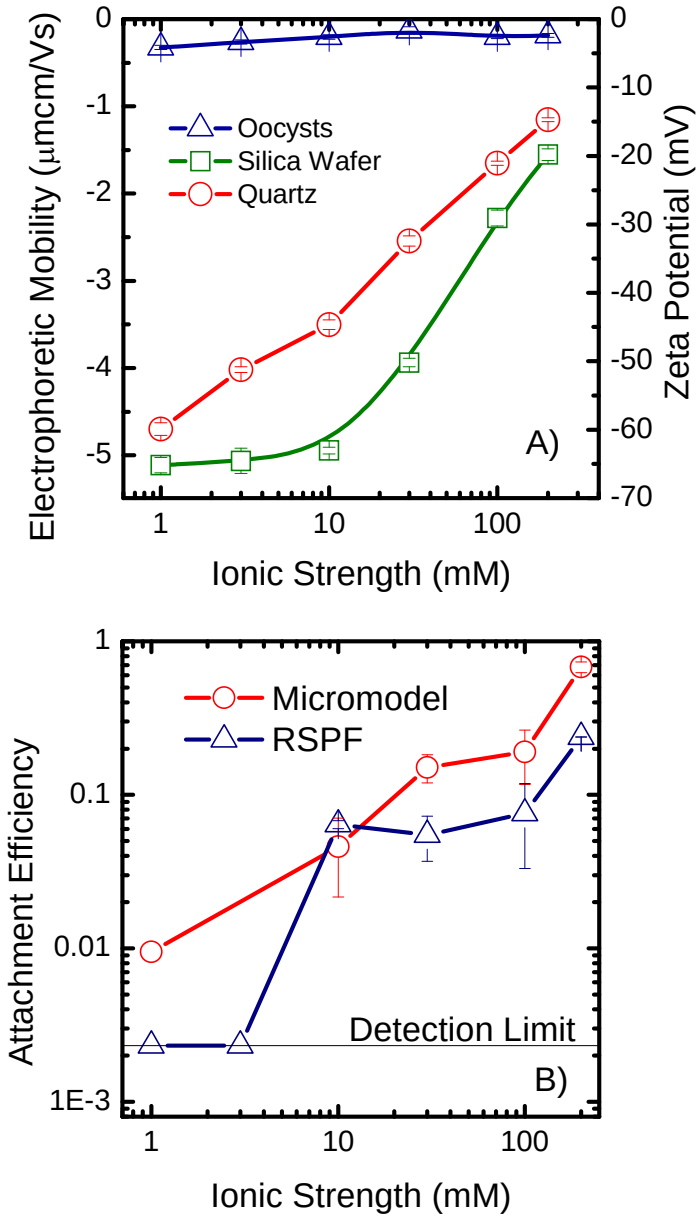

Figure 4.3 (A) Zeta potential of oocysts, silica wafer and quartz surfaces as a function of ionic strength. (B) Attachment efficiency of oocysts as a function of ionic strength in micromodel (circle) and RSPF (triangle). Detection limit is the lowest attachment efficiency that can be detected using a RSPF setup, i.e. one particle deposited during 30 min. Experimental pH: 7.0-7.2.

The calculated DLVO energy profiles of oocyst-micromodel, oocyst-oocyst, CML-micromodel, and CML-CML interaction are shown in Figure 4.4. The values of DLVO energy barriers and the depth of the secondary minimum energy wells for an oocyst interacting with silica wafer (micromodel), quartz (RSPF cell) or another oocyst surface were calculated using zeta potentials and listed in Table 4.1. The same values for a CML particle interacting with silica wafer or another CML particle are listed in Table 4.2. It can be seen from the energy profile and the tables that energy barrier and secondary minimum energy well disappeared above 30 mM and 20 mM NaCl for oocyst attachment in micromodel and RSPF cell, respectively. For oocyst-oocyst interaction, energy barrier disappeared at ionic strength of 10 mM NaCl. For CML-micromodel and CML-CML interaction, energy barriers were found in electrolyte solutions up to 100 mM and 30 mM NaCl, respectively.

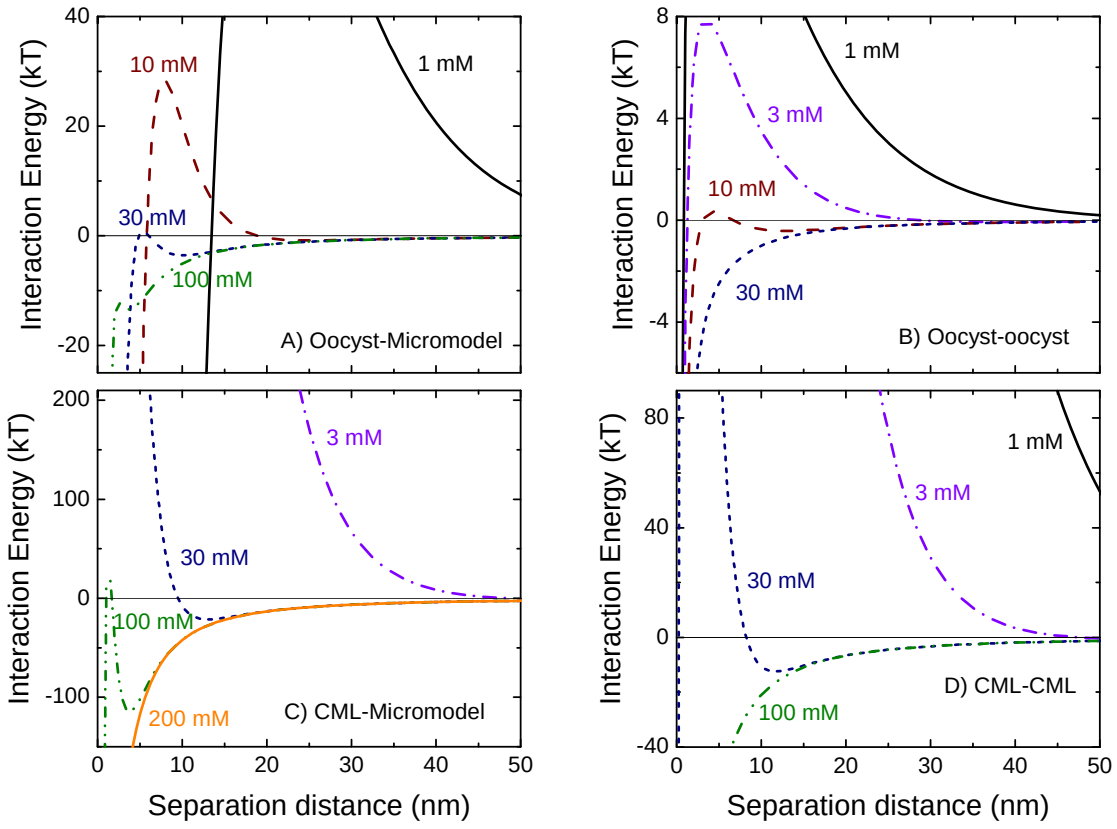

Figure 4.4 DLVO energy profile of oocyst-micromodel interaction (A), oocyst-oocyst interaction (B), CML particle-micromodel interaction (C) and CML particle-CML particle interaction at a variety of ionic strength (Black solid line: 1 mM, violet dash-dot line: 3 mM, wine dash line: 10 mM, navy short dash line: 30 mM, olive dash-dot-dot line: 100 mM and orange solid line: 200 mM).

Table 4.1 Values of DLVO energy barriers, secondary minimum energy well depth, and distance of the secondary minimum energy well for *C. parvum* oocyst interacting with silica wafer, quartz or another *C. parvum* oocyst surfaces (pH 7.0-7.2).

Oocyst-Silica (Micromodel)			
Ionic strength (mM)	Energy barrier (kT)	Secondary minimum depth (kT)	Distance of secondary minimum (nm)
1	90	-0.05	110
3	55	-0.2	55
10	28	-0.8	25
20	22	-1.9	15
30	0.7	-3.6	10
100	NONE	NONE	NONE
Oocyst-Quartz (RSPF cell)			
Ionic strength (mM)	Energy barrier (kT)	Secondary minimum depth (kT)	Distance of secondary minimum (nm)
1	88	-0.05	110
3	55	-0.2	55
10	26	-0.9	23
20	18	-2.2	14
30	NONE	NONE	NONE
Oocyst-oocyst			
Ionic strength (mM)	Energy barrier (kT)	Secondary minimum depth (kT)	Distance of secondary minimum (nm)
1	19	-0.05	75
3	8	-0.07	40
10	0.3	-0.4	13
30	NONE	NONE	NONE

Flow Field in Micromodel. A constant flow rate resulted in an average linear velocity of 2.9 mm/s in the collector array. Reynolds number ($\mathrm{Re} = ((2\rho v R_c)/\mu)$, ρ, μ, and v denoting the density, viscosity, and average linear velocity of the fluid) was 0.52.[45] We simulated the 3D flow field in the micromodel where we also resolved the flow in the region between the supply/withdrawal tubes and the pore network. Figure 4.5A illustrates that the velocity field in the collector array is uniform (when neglecting the pore-scale variability of the flow), even though the flow is nonuniform in the inlet and outlet regions where the flow velocity decreased from the center to the edge along the width (Figure 4.5A). In order to evaluate the uniformity of the flow in the collector array, we determined the average velocity in the 22 pore channels

formed by the first layer of collectors. As shown in Figure 4.5C, this velocity is approximately 10% lower at the micromodel's lateral boundaries than in its center. Since we did not simulate the entire length of the collector array, the actual percentage is even smaller. The flow becomes more uniform in collector layers in the center of the pore network. In any case, the flow nonuniformity is small, and one should expect uniform attachment rates when comparing collectors in the transversal flow direction.

Table 4.2 Values of DLVO energy barriers, secondary minimum energy well depth, and distance of the secondary minimum energy well for CML particle interacting with silica wafer or another CML particle surfaces (pH 7.0-7.2).

CML-Silica (Micromodel)			
Ionic strength (mM)	Energy barrier (kT)	Secondary minimum depth (kT)	Distance of secondary minimum (nm)
1	10800	-0.4	120
10	5800	-6	28
30	3400	-21	13
100	18	-114	4
200	NONE	NONE	NONE
CML-CML			
Ionic strength (mM)	Energy barrier (kT)	Secondary minimum depth (kT)	Distance of secondary minimum (nm)
1	5800	-0.2	125
10	1900	-3	25
30	900	-12	12
100	NONE	NONE	NONE

Within a pore, the velocity profile is nonuniform, as expected. The velocity is highest in the pore centers and vanishes on the collector surfaces due to the no-slip boundary condition. In the collector array, the flow velocity is lowest at the forward and backward stagnation points and highest in pore throats. Figure 4.5B illustrates details of the flow field at the upstream boundary of the collector array. The forward stagnation zones in the first collector layer and the backward stagnation zones in the last layer are larger than inside. Therefore the flow velocity is slower around the first and last transversal collector row at the inlet and outlet regions. Spatial variability in oocyst attachment was expected to correlate with the variability of the flow field.

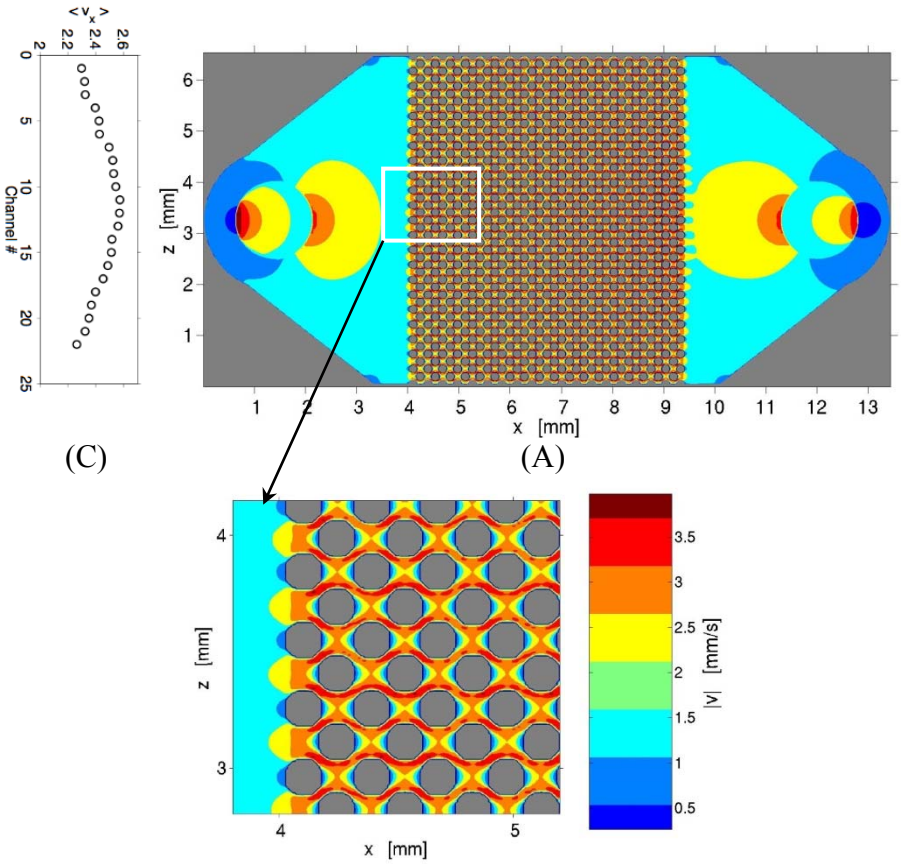

Figure 4.5 (A) Vertically averaged flow field in the micromodel. (B) Magnification of flow field at the beginning of the collector array. (C) Average velocity $<v_x>$ in the 22 channels formed by the first layer of collectors.

Real Time Observation of Oocyst Transport Within a Micromodel. A representative distribution of oocysts on single collectors throughout the pore network at 100 mM NaCl, pH 7.0-7.2 is shown in Figure 4.6. When collectors were clean, most of the oocysts attached to the forward stagnation zone (Figure 4.6A), where the flow velocity was lowest, and less than 1% of oocysts attached to the rear, another region of low flow (Figure 4.5B). Similar observations were made for oocyst attachment at other ionic strengths and CML particle attachment at 100 mM NaCl. For example, for 1 mM NaCl, most oocysts attached to the forward stagnation zone and less than 8% of oocysts attached to the rear (SI Figure 4.7A). For ionic strengths ranging from 3 mM to 200 mM NaCl, less than 2% attached to the rear. For CML particle attachment at 100 mM NaCl, less than 10% CML particles attached to the rear (SI Figure 4.8A). In all the experiments mentioned above, oocysts and CML particles were not observed to migrate along collectors to the backward stagnation regions.

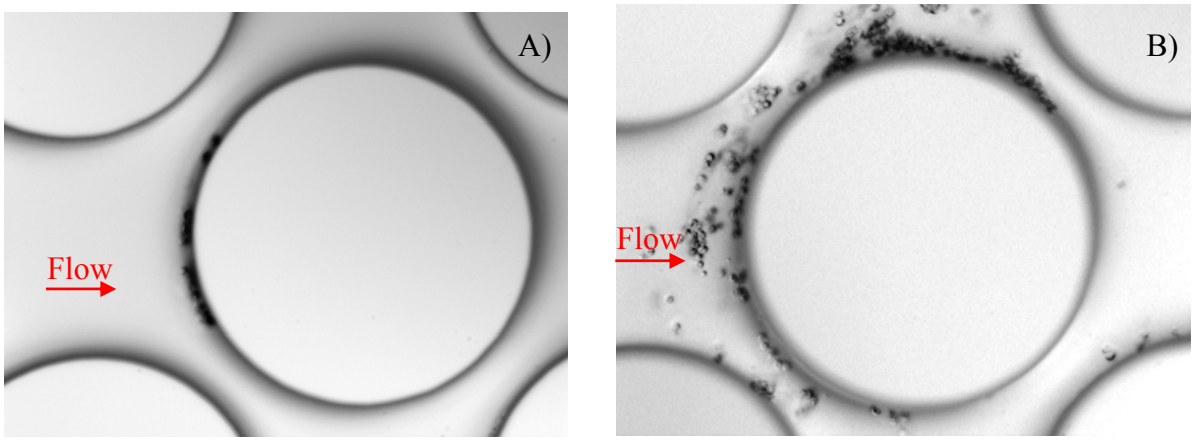

Figure 4.6 Distribution of oocysts on porous media at 100 mM NaCl, pH 7.0-7.2. On clean collector, oocysts (A) attached to the forward portion of the collector. When the surface was covered by oocysts, oocysts (B) were able to attach to already attached oocysts. Experimental condition: porous media depth = 21.3 μm, flow rate = 0.60 mL/h.

At 100 mM NaCl, after 15-20 oocysts attached, oocysts started to attach onto already attached oocysts. As a result, the collectors ripened, multilayer attachment formed, and the number of attached particles was too large to count after half an hour (Figure 4.6B). Similar observations were made for oocyst attachment at 20 mM NaCl and above and for CML particle attachment at 100 mM NaCl (SI Figure 4.8B). Note that at low ionic strength (i.e., 1 mM NaCl) collectors were not ripened during the experimental duration (i.e., 60 min). However, given time (in an experiment extended to 22 hrs), oocyst-oocyst interaction was observed (SI Figure 4.7B). This indicated that ripening time was dependent on ionic strength.

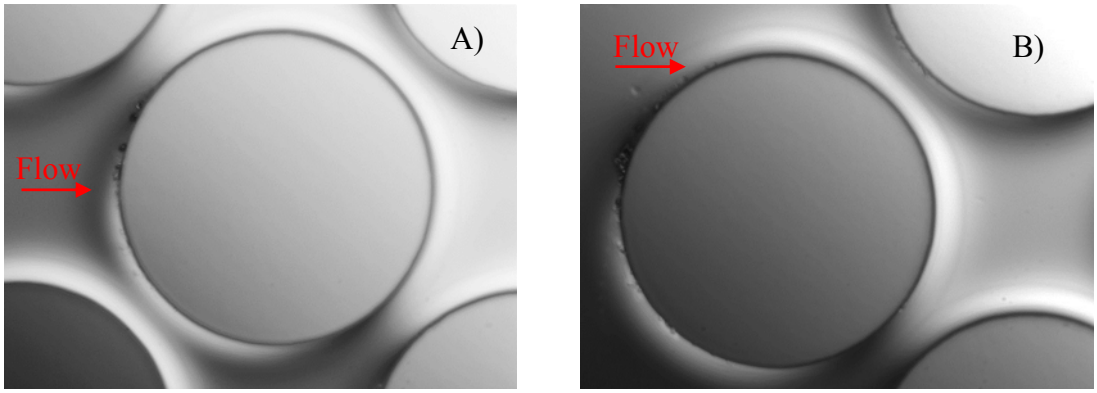

Figure 4.7 Distribution of oocysts on single collectors at 1 mM NaCl, pH 7.0-7.2. On clean collector (A, experimental duration: 1 hr.), oocysts attached to the forward portion of the collector. Giving time, when the surface was covered by oocysts (B, experimental duration: 22 hrs.), oocysts particles were able to attach to already attached oocysts. At low ionic strength (i.e. 1 mM NaCl), it took much longer time for the collectors to be ripened. In this experimental duration, 22 hrs., most collectors were not ripened. Experimental condition: porous media depth = 25.2 μm, flow rate = 0.71 mL/hr.

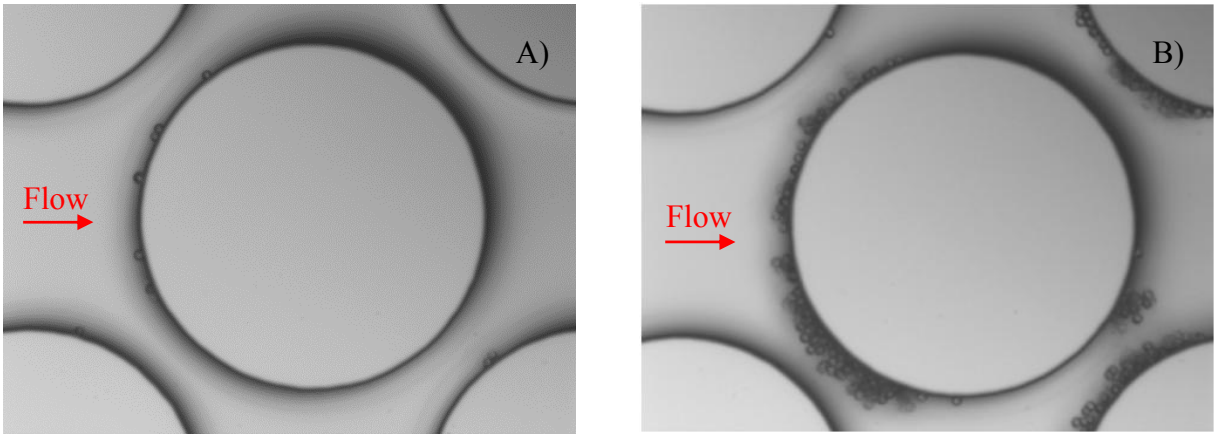

Figure 4.8 Distribution of CML particles on single collectors at 100 mM NaCl, pH 7.0-7.2. On clean collector (A), CML particles attached to the forward portion of the collector. When the surface was covered by particles (B), CML particles were able to attach to already attached particles. Experimental condition: porous media depth = 21.3 μm, flow rate = 0.60 mL/hr.

As shown in Table 4.1 and 4.2, energy barriers of oocyst-oocyst or CML-CML interaction existed up to 10 mM or 30 mM NaCl. Thus, above 10 mM or 30 mM NaCl, it was electrostatically favorable for oocysts or CML particles attached onto already attached oocysts or CML-particles. Therefore oocyst and CML particle concentrations were carefully determined and magnetic stir was used so that no particle aggregation occurred in the suspension. Although particle-particle interactions were not electrostatically favorable at low ionic strength and particle aggregations in suspension at high ionic strength were eliminated by experimental design, particle-particle interactions on collector surface were constantly observed. It is likely that hydrodynamic conditions in the micromodel allow oocysts or CML particles to collide with the already attached oocysts or particles to ripen the filter.

In Figure 4.9, we show the percentage of oocysts that attached to each column (Figure 4.9A) and row (Figure 4.9B) of the collector array under favorable conditions (30 mM NaCl, pH 2.5) in micromodels from different batches. In the transversal direction (Figure 4.9A), oocyst distribution adopted a double hump-shaped pattern: fewer oocysts attached in the center and at the very edges of the pore network. In the longitudinal direction (Figure 4.9B), oocyst distribution adopted a concave-shaped pattern: more oocysts attached to the first 10 to 15 rows and the last few rows of the porous media. The distribution of oocysts at other ionic strengths (e.g. 1 and 100 mM NaCl) and CML particles at 100 mM have similar double hump-shaped patterns in transversal direction and concave-shaped patterns in longitudinal direction (Figure 4.10 and 4.11). The differences of attachment between the upstream and downstream grains in a

single row along the length of the micromodel were also significant (an example at 100 mM NaCl was shown in Figure 4.12 and 4.13). In summary, fewer oocysts attached to collectors in the center region of the pore network. A previous study also showed more attachment at the inlet region of a grain network.

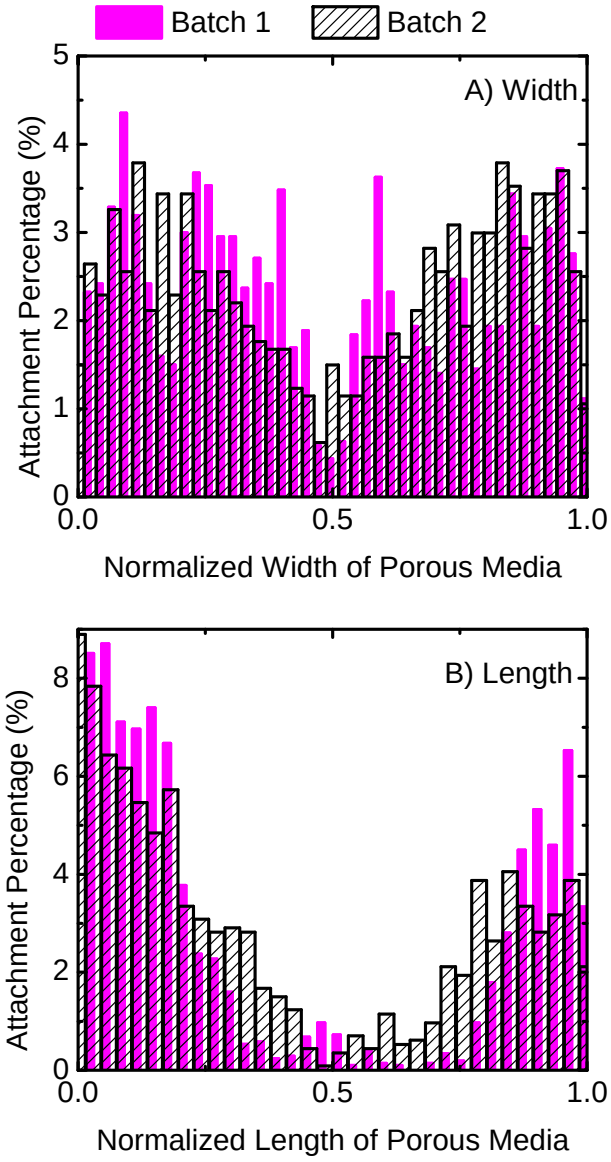

Figure 4.9 Distribution of oocysts at ionic strength of 30 mM NaCl, pH 2.5 along the width (A) and length (B) of porous media in two micromodels made from different batches. The normalized width is the distance from one edge of the porous media divided by the total width. The normalized length is the distance from the first layer of the collectors of the porous media divided by the total length. Experimental condition: batch 1) porous media depth = 21.32 μm, flow rate = 0.60 mL/h; batch 2) porous media depth = 25.2 μm, flow rate = 0.71 mL/h.

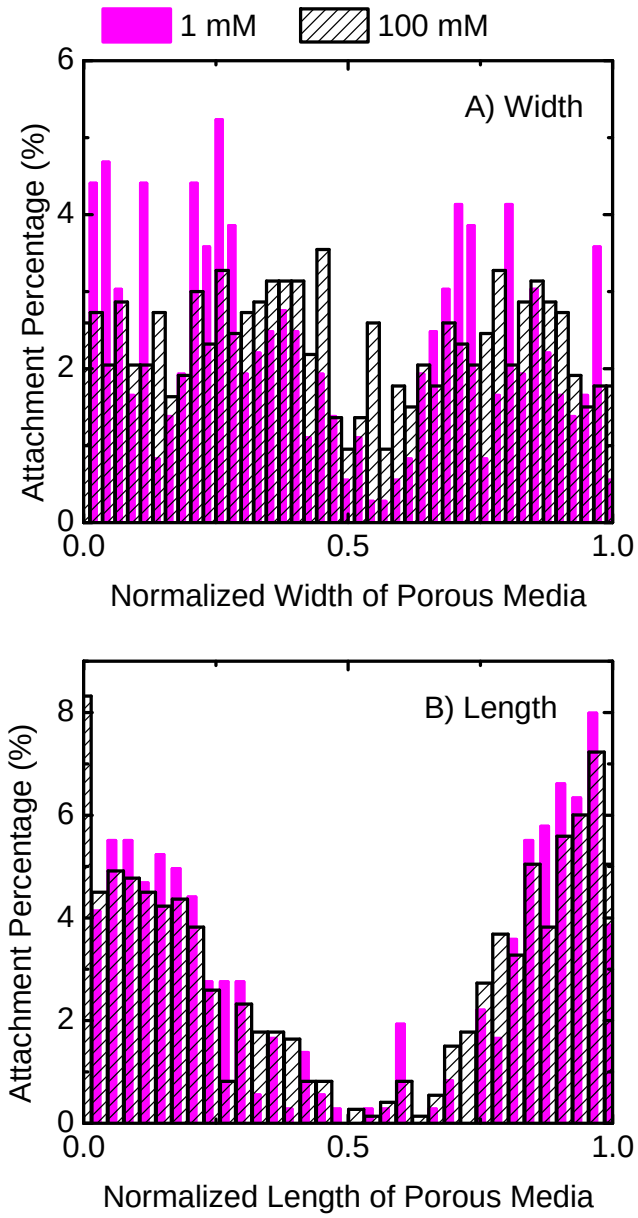

Figure 4.10 Distribution of oocysts at ionic strength of 1 mM and 100 mM NaCl, pH 7.0-7.2 along the width (A) and length (B) of porous media of the micromodel. The normalized width is the distance from one edge of the porous media divided by the total width. The normalized length is the distance from the first layer of the collector rows at the inlet region divided by the total length. Experimental condition: porous media depth = 25.2 μm, flow rate = 0.71 mL/hr.

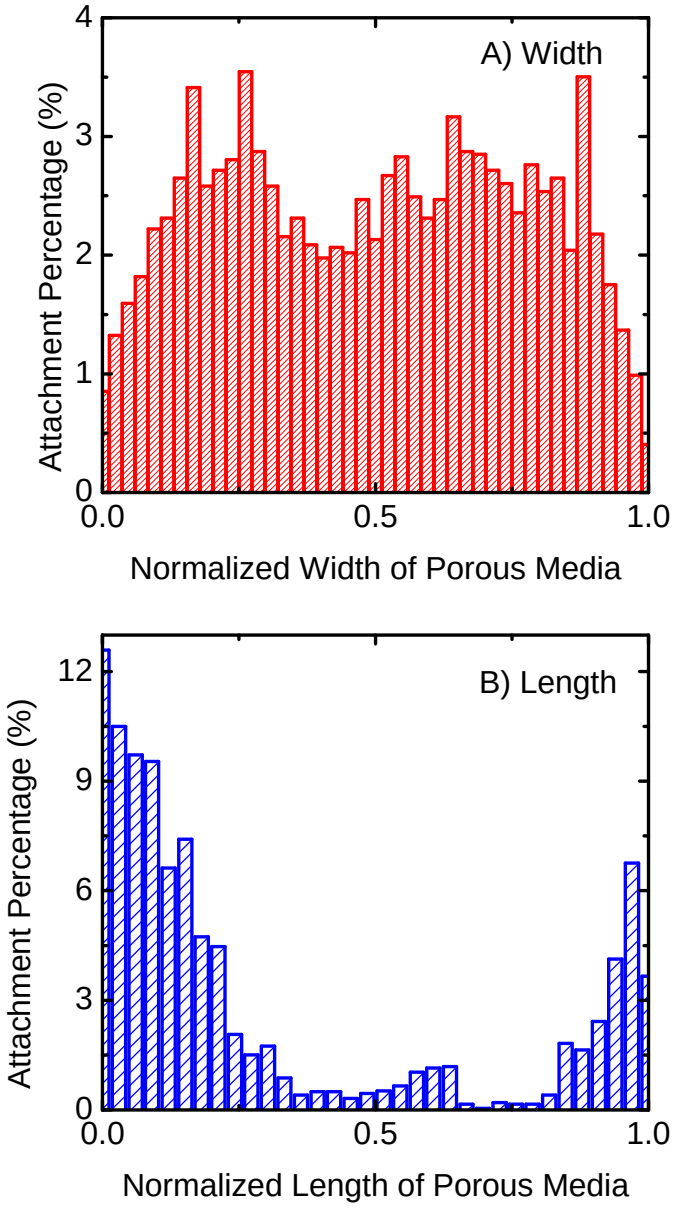

Figure 4.11 Distribution of CML particles at ionic strength of 100 mM NaCl, pH 7.0-7.2 along the width (A) and length (B) of porous media of the micromodel. The normalized width is the distance from one edge of the porous media divided by the total width. The normalized length is the distance from the first layer of the collector rows at the inlet region divided by the total length. Experimental condition: porous media depth = 21.3 μm, flow rate = 0.60 mL/hr.

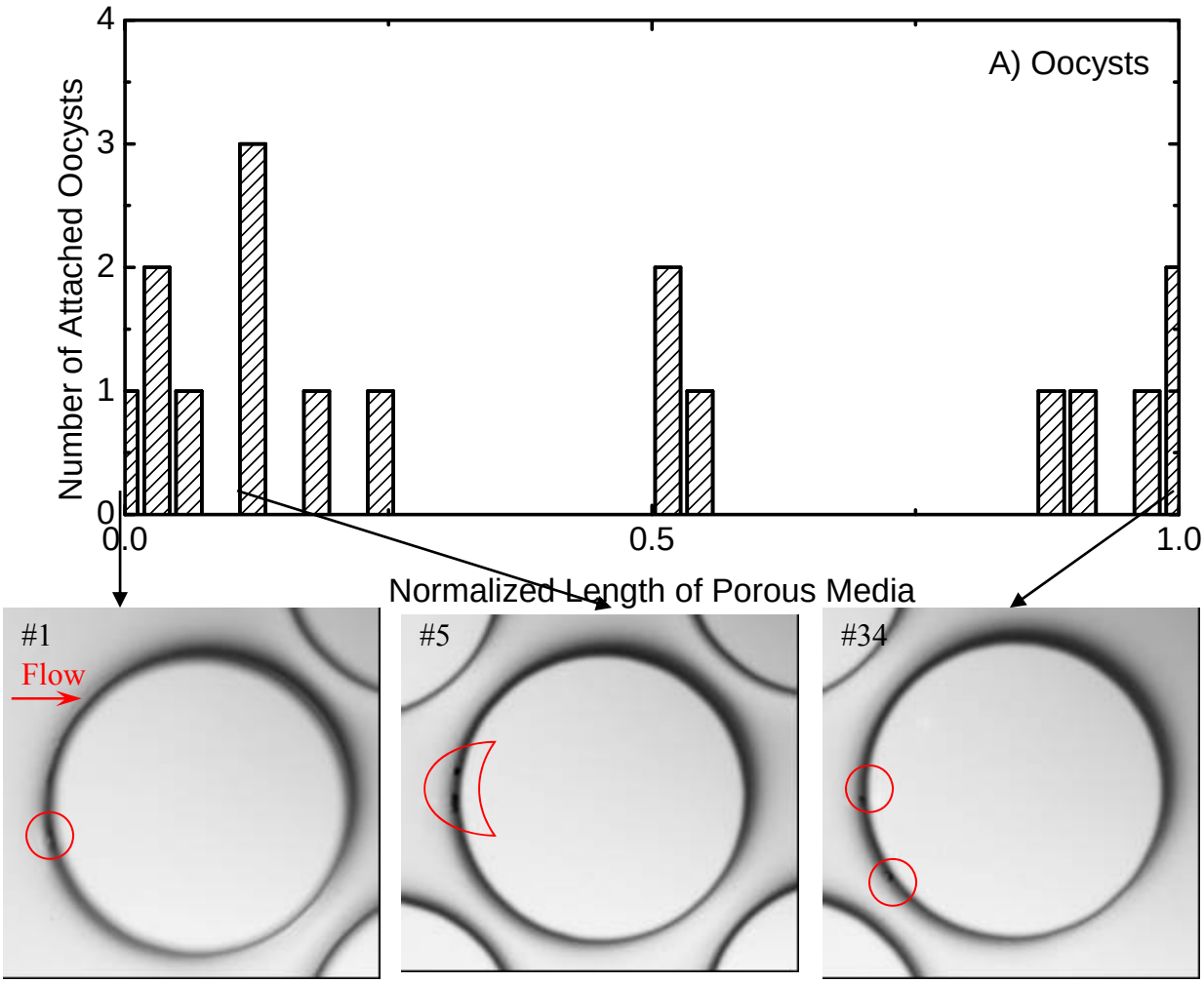

Figure 4.12 Distribution of oocysts on collectors from the same line (line 18#) along the longitudinal direction in the center region of the pore network. Experiment condition: 30 mM NaCl, pH 7.0-7.2.

In the transversal direction (Figure 4.9A), attachment in the center was lower than on the sides. This could be due to a slightly higher flow velocity in the center as shown in Figure 4.5C. This velocity dependence could in principle be explained by the velocity dependence of the diffusion attachment efficiency, $\eta_D \approx v^{-\beta}$ where $\beta > 0$;[46] however, in our experiments diffusion is a negligible deposition mechanism as compared to interception due to the very high Peclet number (on the order of 106) which was used in our experiments. Oocyst attachment to the forward stagnation regions of the collectors was higher in the first two transversal collector rows than in the immediate downstream rows (Figure 4.9B). The larger forward stagnation zones with small flow velocities in the first row (Figure 4.5B) could explain the attachment variation; because these enlarged stagnation zones should direct more oocysts toward the downstream

collector rows. Surprisingly, we observed significantly less oocyst attachment to the central transversal collector rows than to the row that defines the downstream boundary of the grain network (Figure 4.9B and 4.7B). Indeed the attachment rate exhibits a pronounced minimum in the longitudinal center of the network. This observation cannot be explained by variations in flow velocity. Also colloid filtration theory prohibits this minimum and instead predicts that the attachment rate decreases monotonically as suspended particles move through a porous medium, because their concentration decreases (due to attachment). The high flow velocity used in the micromodel experiments unfortunately prevented us from performing LB simulations of advective-diffusive particle transport, because this high velocity led to the aforementioned extremely high Peclet number which is out of reach of LB modeling in a filter medium.[46]

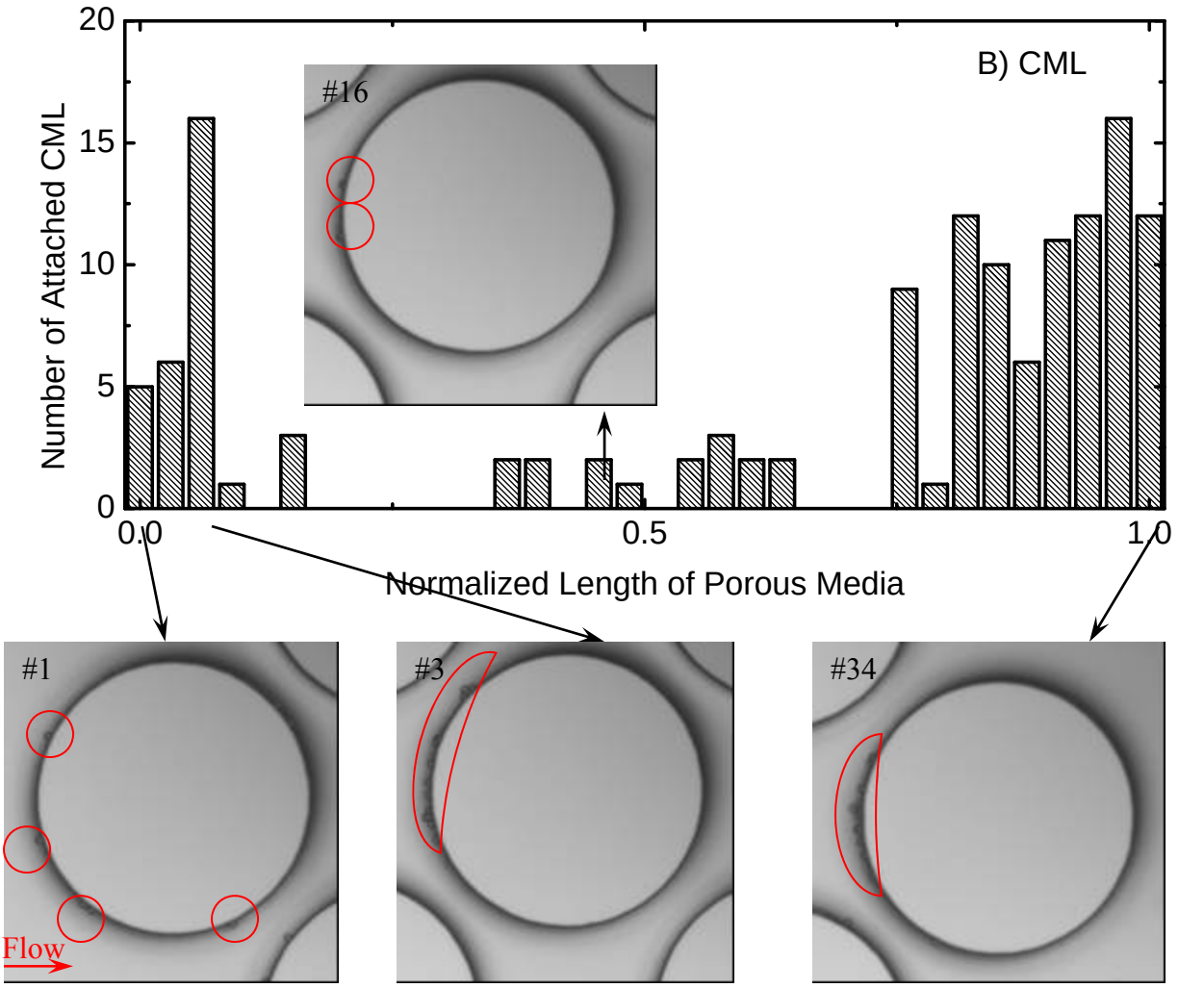

Figure 4.13 Distribution of CML particles on collectors from the same column (column 14#) along the longitudinal direction in the center region of the pore network. Experimental condition: 100 mM NaCl, pH 7.0-7.2.

Measurement of Attachment Efficiency in Micromodel. Under favorable condition, the removal efficiency (η_0) of micromodel batch 1 and micromodel batch 2 was 0.002 and 0.005, respectively. The trend of repulsive condition removal efficiency (η) over a wide range of ionic strength was similar between different batches. The repulsive condition removal efficiency (η) was normalized by favorable condition removal efficiency ($\eta 0$) of the same batch of micromodel to calculate the average attachment efficiency (α). Small error bars of attachment efficiency in Figure 4.3B indicated that the average attachment efficiency (α) from different batches of micromodel were consistent and comparable.

On the bases of DLVO calculation (Table 4.1), attachment efficiency (α) should be equal to unity for ionic strength above 30 mM NaCl, where the energy barrier between oocysts and collector surfaces disappears. However, attachment efficiency (α) increased to less than unity over the whole range of ionic strength (i.e., 0.68 at 200 mM NaCl). The discrepancy between experimental measurement and DLVO theory has been observed before.[6, 7, 10, 16] Similar to the previous studies, we also attribute this discrepancy to the steric repulsion between oocyst and the collector surface. This interaction has been measured before by atomic force microscopy technique.[14]

Comparison of Attachment Efficiencies Measured by Micromodel and RSPF Setups. Attachment efficiencies were measured with linear velocity of 2.9 mm/s for micromodel and 5.3 mm/s for RSPF setups. Because of the difference in velocity and pore geometries, direct comparison for attachment efficiency obtained by these two setups was not possible. Instead the trend of attachment efficiency obtained over a range of ionic strength was compared to illustrate the effect of electrostatic interaction on oocyst attachment in setups with single stagnation points (i.e., RSPF) and multiple collectors (i.e., micromodel). As mentioned above, in micromodels, oocysts deposited mainly on the forward half zone of the collector surface. For the RSFP, attachment efficiency was determined for an area of 296 × 222 μm, while for micromodel attachment efficiency was determined for 1440 collectors each with 565 μm × 24 μm area. As shown in Figure 4.3B, the attachment efficiency (α) increased with ionic strength for both setups and the trends were similar, indicating that electrostatic interaction controls oocyst attachment. However, attachment efficiency for micromodel was consistently higher than that for RSPF cell. This observation is consistent with a previous study on *E. coli* transport using column with linear velocity of 0.2 mm/s and RSPF with 26.5 mm/s.[36] Another study focusing on latex particle

attachment in micromodel at different flow rates also found higher collector efficiency at lower velocity.[38]

Reversibility of Oocyst Attachment in Micromodel. Detachment experiments for oocysts were conducted after attachment experiments at 30 mM NaCl, where secondary minimum attachment was possible, and at 200 mM NaCl, where only primary attachment took place, based on DLVO calculation (Table 4.1). The detachment experiment for CML particles was conducted after attachment experiment at 100 mM NaCl, where secondary minimum attachment was possible. Specifically, after attachment experiments, the micromodel was eluted sequentially with the same electrolyte as for the attachment experiments but without oocysts, then with 1 mM NaCl at pH 7.0-7.2, and finally with 1 mM NaOH solution at pH 11. For all experiments, i.e., attachment at 30 mM and 200 mM NaCl and attachment of CML particles at 100 mM NaCl, elution with 1 mM NaCl resulted in the release of less than 6% of the attached oocysts or CML particles. However, elution with pH 11 led to the release of around 60-75% of attached oocysts (Figure 4.15) and the release of 21% of attached CML particles (SI Figure 4.14).

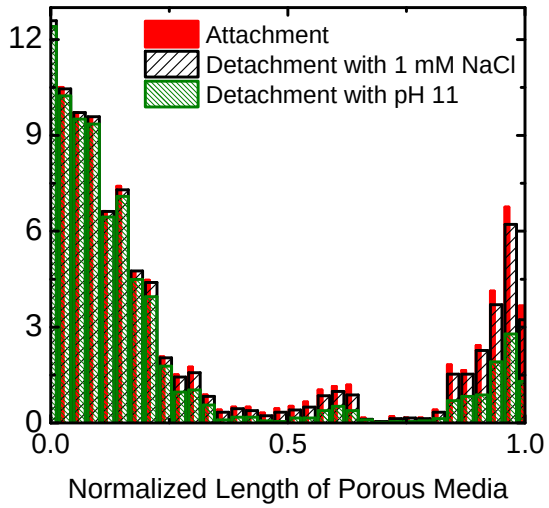

Figure 4.14 Distribution of CML (red column) along the length of porous media in 100 mM NaCl at pH 7.0-7.2. CML remained in the porous media after pumped in 1 mM NaCl at pH 7.0-7.2 (black column) and after pumped in solution of pH 11 (green column) at least 4 hours. The normalized length is the distance from the first layer of the collectors of the porous media divided by the total length. Experimental condition: porous media depth = 24.2 μm, flow rate = 0.68 mL/hr.

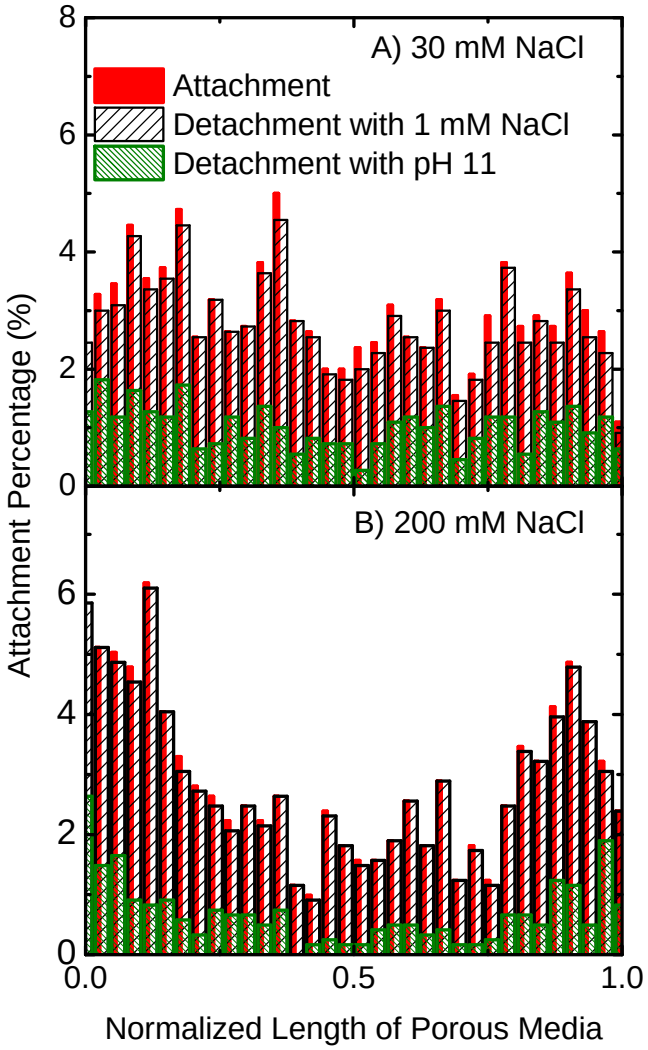

Figure 4.15 Distribution of oocysts (red column) along the length of porous media in (A) 30 mM NaCl and (B) 200 mM NaCl at pH 7.0-7.2. Oocysts remained in the porous media after pumped in 1 mM NaCl at pH 7.0-7.2 (black column) and after pumped in solution of pH 11 (green column) at least 4 hours. The normalized length is the distance from the first layer of the collectors of the porous media divided by the total length. Experimental condition: (A) porous media depth = 25.20 μm, flow rate = 0.709 mL/hr. (B) Porous media depth = 21.32 μm, flow rate = 0.6 mL/hr.

In our previous work,[35] peptides digested from oocyst surface macromolecules by proteinase K were analyzed by LC/MS/MS. Among the digested peptides, we identified amino acids with both negatively charged (i.e., carboxylate with pKa 1.8-2.6) and positively charged (i.e., amine with pKa 8.8-10.6) functional groups. These positively and negatively charged functional groups qualitatively indicated surface charge heterogeneity of oocysts. Elution by pH

11 electrolyte has been used in a number of studies to release colloid attached due to surface charge heterogeneity.[9, 47] On the one hand, increasing pH leads to increase of the energy barrier, which drives particle release. On the other hand, at pH 11, functional groups of amino acids in the oocyst walls, which are positively charged at pH 7, are negatively charged. Oocysts attached to negatively charged collectors due to positively charged sites on the oocyst surface at pH 7.0 are expected to be released at pH 11. The micromodels were fabricated in a clean-room condition and were expected to be free of metal oxide contamination that could give collector surface positively charged sites. Sixty to seventy five percent of attached oocysts were released at pH 11 while only 21% of CML particles, which have more charge homogeneous surface than oocysts, were released at pH 11, indicating that charge heterogeneity of the oocyst surface allowed oocysts to attach to collector at pH 7.

We have shown previously that in a RSPF setup oocysts entrapped in secondary minimum on quartz surfaces can be transferred to primary minimum attachment or swiped away by bypass flow.[7] With elution by 1 mM NaCl, the energy barrier between oocyst and collector surfaces calculated by DLVO theory increased from 0.7 kT to 90 kT. Oocysts entrapped in secondary minimum were expected to be released upon exposure to 1 mM NaCl. Less than 6% attached oocysts were released when eluted by 1 mM NaCl, indicating that oocysts entrapped in the secondary minimum were not stable due to the shallow energy well. Those oocysts were either transferred to primary minimum attachment or released by bypass flow.

4.5 Environmental Implications

As observed in this study, filter collectors were ripened because oocysts attached onto already attached oocysts and reduced the region available for flow. Thus, oocyst-oocyst interaction is essential in formulating a transport model.

The observation that oocyst attachment increased as the flow velocity decreased suggests the important role of porous media heterogeneity. More oocysts may accumulate where physical heterogeneity leads to low flow condition. However, oocysts may transport further where high flow condition is achieved. For example, Hater et al. suggested that macroporous flow is responsible for oocyst transport through the soil.[29] The results from the micromodel attachment and detachment experiments showed that surface charge heterogeneity significantly increased

oocyst attachment. Those oocysts attached due to charge heterogeneity may be remobilized when the environmental solution pH increases. The attachment and detachment experiments also suggested that oocysts entrapped in secondary minimum were either transferred to primary minimum or were released by the bypass flow. Therefore, few oocysts were detached when ionic strength decreased. A modest change of environmental solution chemistry is probably not sufficient to release a significant number of oocysts from the subsurface environment. Our results imply that oocysts can be immobilized by filtration through subsurface. However, the low ionic strength and high flow rate during the rainy season may cause the soil environment to be more vulnerable for oocyst breakthrough.

Acknowledgements. This work was supported by the National Science Foundation (NSF, CTS-0120978), NSF Career grant #0954501, and the Illinois Water Resources Center (grant #USGS 06HQGR0083). Partial financial support for CYZ was provided by the Environmental Molecular Sciences Laboratory (EMSL), a national scientific user facility sponsored by the DOE, Office of Biological and Environmental Research and located at PNNL. MH was supported by NSF Grant EAR-0911425. Computations were performed on the Homewood High Performance Cluster at JHU.

4.6 References

1. Corso, P. S.; Kramer, M. H.; Blair, K. A.; Addiss, D. G.; Davis, J. P.; Haddix, A. C. Cost of illness in the 1993 waterborne *Cryptosporidium* outbreak, Milwaukee, Wisconsin. *Emerging Infectious Diseases* **2003,** *9* (4), 426-431.

2. Fong, T. T.; Mansfield, L. S.; Wilson, D. L.; Schwab, D. J.; Molloy, S. L.; Rose, J. B. Massive microbiological groundwater contamination associated with a waterborne outbreak in Lake Erie, South Bass Island, Ohio. *Environmental Health Perspectives* **2007,** *115* (6), 856-864.

3. Gallay, A.; De Valk, H.; Cournot, M.; Ladeuil, B.; Hemery, C.; Castor, C.; Bon, F.; Megraud, F.; Le Cann, P.; Desenclos, J. C. A large multi-pathogen waterborne community outbreak linked to faecal contamination of a groundwater system, France, 2000. *Clinical Microbiology and Infection* **2006,** *12* (6), 561-570.

4. Hancock, C. M.; Rose, J. B.; Callahan, M. Crypto and *Giardia* in U.S. groundwater. *Journal of the American Water Works Association* **1998,** *90*, 58-61.

5. LeChevallier, M. W.; Norton, W. D.; Siegel, J. E.; Abbaszadegan, M., Evaluation of the immunofluorescence procedure for detection of *Giardia* cysts and *Cryptosporidium* oocysts in water. In 1995; Vol. 61, pp 690-697.

6. Kuznar, Z. A.; Elimelech, M. Adhesion kinetics of viable *Cryptosporidium parvum* oocysts to quartz surfaces. *Environmental Science & Technology* **2004,** *38* (24), 6839-6845.

7. Liu, Y.; Janjaroen, D.; Kuhlenschmidt, M. S.; Kuhlenschmidt, T. B.; Nguyen, T. H. Deposition of *Cryptosporidium parvum* oocysts on natural organic matter surfaces: microscopic evidence for secondary minimum deposition in a radial stagnation point flow cell. *Langmuir* **2009,** *25* (3), 1594-1605.

8. Tufenkji, N.; Dixon, D. R.; Considine, R.; Drummond, C. J. Multi-scale *Cryptosporidium*/sand interactions in water treatment. *Water Research* **2006,** *40* (18), 3315-3331.

9. Tufenkji, N.; Elimelech, M. Spatial distributions of *Cryptosporidium oocysts* in porous media: Evidence for dual mode deposition. *Environmental Science & Technology* **2005,** *39* (10), 3620-3629.

10. Kuznar, Z. A.; Elimelech, M. *Cryptosporidium* oocyst surface macromolecules significantly hinder oocyst attachment. *Environmental Science & Technology* **2006,** *40* (6), 1837-1842.

11. Bradford, S. A.; Simunek, J.; Bettahar, M.; van Genuchten, M. T.; Yates, S. R. Significance of straining in colloid deposition: Evidence and implications. *Water Resources Research* **2006,** *42* (12).

12. Harter, T.; Wagner, S.; Atwill, E. R. Colloid transport and filtration of *Cryptosporidium parvum* in sandy soils and aquifer sediments. *Environmental Science & Technology* **2000,** *34* (1), 62-70.

13. Tong, M. P.; Ma, H. L.; Johnson, W. P. Funneling of flow into grain-to-grain contacts drives colloid-colloid aggregation in the presence of an energy barrier. *Environmental Science & Technology* **2008,** *42* (8), 2826-2832.

14. Byrd, T. L.; Walz, J. Y. Interaction force profiles between *Cryptosporidium parvum* oocysts and silica surfaces. *Environmental Science & Technology* **2005,** *39* (24), 9574-9582.

15. Janjaroen, D.; Liu, Y.; Kuhlenschmidt, M. S.; Kuhlenschmidt, T. B.; Nguyen, T. H. Role of divalent cations on deposition of *Cryptosporidium parvum* oocysts on natural organic matter surfaces. *Environmental Science & Technology* **2010,** *44* (12), 4519-4524.

16. Kuznar, Z. A.; Elimelech, M. Role of surface proteins in the deposition kinetics of *Cryptosporidium parvum* oocysts. *Langmuir* **2005,** *21* (2), 710-716.
17. Tufenkji, N.; Miller, G. F.; Ryan, J. N.; Harvey, R. W.; Elimelech, M. Transport of *Cryptosporidium oocysts* in porous media: Role of straining and physicochemical filtration. *Environmental Science & Technology* **2004,** *38* (22), 5932-5938.
18. Kim, H. N.; Walker, S. L.; Bradford, S. A. Coupled factors influencing the transport and retention of *Cryptosporidium parvum* oocysts in saturated porous media. *Water Research* **2010,** *44* (4), 1213-1223.
19. Bradford, S. A.; Bettahar, M. Straining, attachment, and detachment of *Cryptosporidium oocysts* in saturated porous media. *Journal of Environmental Quality* **2005,** *34* (2), 469-478.
20. Hsu, B. M.; Huang, C. P.; Pan, J. R. Filtration behaviors of *Giardia* and *Cryptosporidium* - Ionic strength and pH effects. *Water Research* **2001,** *35* (16), 3777-3782.
21. Cortis, A.; Harter, T.; Hou, L.; Atwill, E. R.; Packman, A. I.; Green, P. G. Transport of *Cryptosporidium parvum* in porous media: Long-term elution experiments and continuous time random walk filtration modeling. *Water Resources Research* **2006,** *42* (12), W12S13.
22. Abudalo, R. A.; Bogatsu, Y. G.; Ryan, J. N.; Harvey, R. W.; Metge, D. W.; Elimelech, M. Effect of ferric oxyhydroxide grain coatings on the transport of bacteriophage PRD1 and *Cryptosporidium parvum* oocysts in saturated porous media. *Environmental Science & Technology* **2005,** *39* (17), 6412-6419.
23. Metge, D. W.; Harvey, R. W.; Aiken, G. R.; Anders, R.; Lincoln, G.; Jasperse, J. Influence of organic carbon loading, sediment associated metal oxide content and sediment grain size distributions upon *Cryptosporidium parvum* removal during riverbank filtration operations, Sonoma County, CA. *Water Research* **2010,** *44* (4), 1126-1137.
24. Dai, X. J.; Hozalski, R. M. Effect of NOM and biofilm on the removal of *Cryptosporidium parvum* oocysts in rapid filters. *Water Research* **2002,** *36* (14), 3523-3532.
25. Dai, X.; Boll, J.; Hayes, M. E.; Aston, D. E. Adhesion of *Cryptosporidium parvum* and *Giardia lamblia* to solid surfaces: the role of surface charge and hydrophobicity. *Colloids and Surfaces B-Biointerfaces* **2004,** *34* (4), 259-263.
26. Searcy, K. E.; Packman, A. I.; Atwill, E. R.; Harter, T. Association of *Cryptosporidium parvum* with suspended particles: Impact on oocyst sedimentation. *Appl. Environ. Microbiol.* **2005,** *71* (2), 1072-1078.

27. Searcy, K. E.; Packman, A. L.; Atwill, E. R.; Harter, T. Deposition of *Cryptosporidium* oocysts in streambeds. *Applied and Environmental Microbiology* **2006,** *72* (3), 1810-1816.
28. Logan, A. J.; Stevik, T. K.; Siegrist, R. L.; Ronn, R. M. Transport and fate of *Cryptosporidium parvum* oocysts in intermittent sand filters. *Water Research* **2001,** *35* (18), 4359-4369.
29. Harter, T.; Atwill, E. R.; Hou, L.; Karle, B. M.; Tate, K. W. Developing risk models of *Cryptosporidium* transport in soils from vegetated, tilted soilbox experiments. *Journal of Environmental Quality* **2008,** *37* (1), 245-258.
30. Kim, J.; Lawler, D. F. Influence of particle characteristics on filter ripening. *Separation Science & Technology* **2008,** *43* (7), 1583-1594.
31. Kim, J.; Nason, J. A.; Lawler, D. F. Influence of surface charge distributions and particle size distributions on particle attachment in granular media filtration. *Environmental Science & Technology* **2008,** *42* (7), 2557-2562.
32. Kretzschmar, R.; Barmettler, K.; Grolimund, D.; Yan, Y.-d.; Borkovec, M.; Sticher, H. Experimental determination of colloid deposition rates and collision efficiencies in natural porous media. *Water Resources Research* **1997,** *33* (5), 1129-1137.
33. Kuznar, Z. A.; Elimelech, M. Direct microscopic observation of particle deposition in porous media: Role of the secondary energy minimum. *Colloids and Surfaces a-Physicochemical and Engineering Aspects* **2007,** *294* (1-3), 156-162.
34. Kusaka, Y.; Duval, J. F. L.; Adachi, Y. Morphology and breaking of latex particle deposits at a cylindrical collector in a microfluidic chamber. *Environmental Science & Technology* **2010**, 9413–9418.
35. Liu, Y.; Kuhlenschmidt, M. S.; Kuhlenschmidt, T. B.; Nguyen, T. H. Composition and conformation of *Cryptosporidium parvum* oocyst wall surface macromolecules and their effect on adhesion kinetics of oocysts on quartz surface. *Biomacromolecules* **2010,** *11* (8), 2109-2115.
36. Walker, S. L.; Redman, J. A.; Elimelech, M. Role of cell surface lipopolysaccharides in *Escherichia coli* K12 adhesion and transport. *Langmuir* **2004,** *20* (18), 7736-7746.
37. Baumann, T.; Werth, C. J. Visualization and modeling of polystyrol colloid transport in a silicon micromodel. *Vadose Zone Journal* **2004,** *3* (2), 434-443.
38. Auset, M.; Keller, A. A. Pore-scale visualization of colloid straining and filtration in saturated porous media using micromodels. *Water Resources Research* **2006,** *42* (12).

39. Johnson, J. K.; Schmidt, J.; Gelberg, H. B.; Kuhlenschmidt, M. S. Microbial adhesion of *Cryptosporidium parvum* sporozoites: Purification of an inhibitory lipid from bovine mucosa. *Journal of Parasitology* **2004,** *90* (5), 980-990.

40. Hogg, R.; Healy, T. W.; Fuerstenau, D. W. Mutual coagulation of colloidal dispersions. *Transactions of the Faraday Society* **1965,** *62*, 1638-1651.

41. Gregory, J. Approximate expressions for retarded van der waals interaction. *J. Colloid Interface Sci.* **1981,** *83* (1), 138-145.

42. de Kerchove, A. J.; Weronski, P.; Elimelech, M. Adhesion of nonmotile Pseudomonas aeruginosa on "soft" polyelectrolyte layer in a radial stagnation point flow system: Measurements and model predictions. *Langmuir* **2007,** *23* (24), 12301-12308.

43. d'Humieres, D.; Ginzburg, I.; Krafczyk, M.; Lallemand, P.; Luo, L. S. Multiple-relaxation-time lattice Boltzmann models in three dimensions. *Philosophical Transactions of The Royal Society of London Series A* **2002,** *360* (1792), 437-451.

44. Hilpert, M. Determination of dimensional flow fields in hydrogeological settings via the MRT lattice Boltzmann method. *Water Resources Research* **2011**.

45. Koch, D., L. ; Ladd, A. J. C. Moderate Reynolds number flows through periodic and random arrays of aligned cylinders. *Journal of Fluid Mechanics* **1997,** *349*, 31-66.

46. Long, W.; Hilpert, M. A correlation for the collector efficiency of brownian particles in clean-bed filtration in sphere packings by a lattice-Boltzmann method. *Environmental Science & Technology* **2009,** *43* (12), 4419-4424.

47. Ryan, J. N.; Elimelech, M. Colloid mobilization and transport in groundwater. *Colloids and Surfaces A: Physicochemical and Engineering Aspects* **1996,** *107* (0), 1-56.

CHAPTER 5

ROLE OF COLLECTOR ALTERNATING CHARGED PATCHES ON TRANSPORT OF *CRYPTOSPORIDIUM PARVUM* OOCYSTS IN A MICROMODEL

Will Submit to *Environmental Science & Technology*, 2012

Liu, Y.; Zhang, C.; Hu, D.; Kuhlenschmidt, M. S.; Kuhlenschmidt, T. B.; Mylon, S. E.; Kong, R.; Bhargava, R; Nguyen, T. H. Role of Collector Alternating Charged Patches on Transport of *Cryptosporidium parvum* Oocysts in a Micromodel,

5.1 Abstract

The role of collector surface charge heterogeneity on transport of *Cryptosporidium parvum* oocyst and carboxylate microsphere in 2-dimensional micromodels was studied. The cylindrical silica collectors of the micromodels were coated with 0, 10, 20, 50, and 100% Fe_2O_3 patches. The experimental values of average single collector removal efficiencies (η) on the Fe_2O_3 patches and on the entire collectors were determined. In the presence of significant (>3500 kT) Derjaguin–Landau–Verwey–Overbeek (DLVO) energy barrier between the microspheres and the silica collectors at pH 5.8 and 8.1, the values of η determined for Fe_2O_3 patches were lower than that obtained for collectors coated entirely with Fe_2O_3. However, η on Fe_2O_3 patches for microspheres at pH 4.4 and for oocysts at pH 5.8 and 8.1, where the DLVO energy barrier was relatively small (198-360 kT), were higher than that on the collectors coated entirely with Fe_2O_3. The dependence of η determined for Fe_2O_3 patches on DLVO energy barrier indicated the importance of periodic favorable and unfavorable electrostatic interactions between colloids and collectors with alternating Fe_2O_3 and silica patches. The discrepancy between experimental determined and patchwise geochemical heterogeneous model predicted η for the entire collectors was observed and can be explained by the model's lack of consideration for the spatial distribution of charge heterogeneity on the collector surface. In addition, oocysts attached more on Fe_2O_3 surfaces at pH 8.1 than at pH 5.8 though DLVO predicted energy barrier between

oocyst and Fe_2O_3 surfaces at pH 8.1 while no energy barrier at pH 5.8. The results indicated complexations between oocyst carboxylate groups and Fe mental centers of Fe_2O_3 surfaces at different pH.

5.2 Introduction

Cryptosporidium parvum (C. parvum) is identified as a pathogenic microorganism that targets mammals including humans. This protozoan waterborne pathogen causes a self-limited gastrointestinal disease, cryptosporidiosis, by the fecal-oral route and exists as oocysts in the environment. Outbreaks of cryptosporidiosis were reported frequently each year due to the challenges to remove *Cryptosporidium* oocysts from drinking or recreational water.[1-3] Filtration is recommended to control this potential contaminant by National Primary Drinking Water Regulations.[4] Facilities without filtration are required to include *Cryptosporidium* in their existing watershed control provisions. Therefore, investigation of oocyst transport in porous media has been intensively reported in the past decades.[5-13]

Soil is a mixture of minerals, which includes various elements such as O, Si, Al, Fe, Ca, Na, K and Mn. The oxides of Fe and Mn are important sources of geochemical heterogeneities of soil matrix and their fraction in the total mass of the soil matrix is typically in the range of 0.5-2%.[14, 15] The Fe concentration varies in the range of 4-47% under extreme condition, such as in the sediments of a river receiving acid mine waters.[16] This geochemical charge heterogeneity is expected to play an important role on oocyst transport.[5, 8, 10, 17] Transport experiments of oocysts in columns packed with mixed quartz sand and ferric oxyhydroxide grain suggested that oocyst attachment was not proportional with the fraction of ferric oxyhydroxide.[8]

Patchwise geochemical heterogeneous model assumes a linear correlation between attachment efficiency and fraction of chemical heterogeneity.[18] This model fits well for colloid attachment on surfaces with macroscopic-scale charge heterogeneity, of where the heterogeneous patches are much larger than the interacting colloids.[8, 14, 18-20] However, the influence of microscopic-scale surface charge heterogeneity, where the heterogeneous patches are comparable to colloids in size, on colloid transport is less understood.[8, 21, 22] Positively charged amino-silanized strips were created on glass substrate, which was assembled onto a radial stagnation point flow (RSPF) system, to study the influence of patchwise geochemical

heterogeneity on polystyrene latex particle attachment.[22] The results showed an obvious over-prediction of patchwise geochemical heterogeneity model at low ionic strength and high flow velocity due to "hydrodynamic bump" effect. The Eulerian model (convection-diffusion-migration equation), which incorporated DLVO interaction in a steady state flux conservation equation, was used to simulate colloid attachment in a RSPF system with circular alternating strips bearing different charges[23] or on a spherical collectors with alternating strips bearing different charges[21]. The results illustrated that simulated colloid attachment reached the platform with 30-40% fraction of chemical heterogeneity and was significantly higher than particle attachment predicted by patchwise geochemical heterogeneity model. This simulation result contradicted the "hydrodynamic bump" effect and needed to be tested by experimental data.

In this chapter, silica micromodels contained collectors coated with 0, 10, 20, 50 and 100% Fe_2O_3 was first fabricated to create microscopic-scale patchwise charged heterogeneous collectors to study the influence of charge heterogeneous on oocyst and carboxylate microsphere transport. Direct observations of colloid transport on charged heterogeneous collectors were conducted. Experimental attachment efficiencies were compared to patchwise geochemical heterogeneity model to give insight into the influence of charge heterogeneity on oocyst transport.

5.3 Materials and Methods

Patchwise Charged Heterogeneous Micromodel Fabrication. The micromodel with/without Fe_2O_3 coating was fabricated following a modified photolithography procedure in a class 10 cleanroom.[7] The Fe_2O_3 source was purchased from Kurt J Lesker (99.9% Fe_2O_3). A total of 9 micromodels was fabricated from one silicon wafer (100 mm in diameter and 0.5 mm in thickness, Virginia Semiconductor). Each micromodel (Figure 5.1A) had 1838 uniformly distributed cylindrical collectors with a diameter of 190 μm and a height range from 22 μm to 28 μm. The pore network had a pore-body of 130 μm and a pore-throat of 36 μm resulting in a porosity of 0.45 (Figure 5.1B). For the patchwise charged heterogeneous collectors, Fe_2O_3 band covered the wall of the cylindrical collectors from top to bottom and an area adjacent to the collectors (Figure 5.1B and Figure 5.2G). The width of the Fe_2O_3 band was 9.9, 9.9 and 49.7 μm

for silica collectors coated with 10, 20 and 50% Fe_2O_3, respectively (Figure 5.3B, 5.3C and 5.3D).

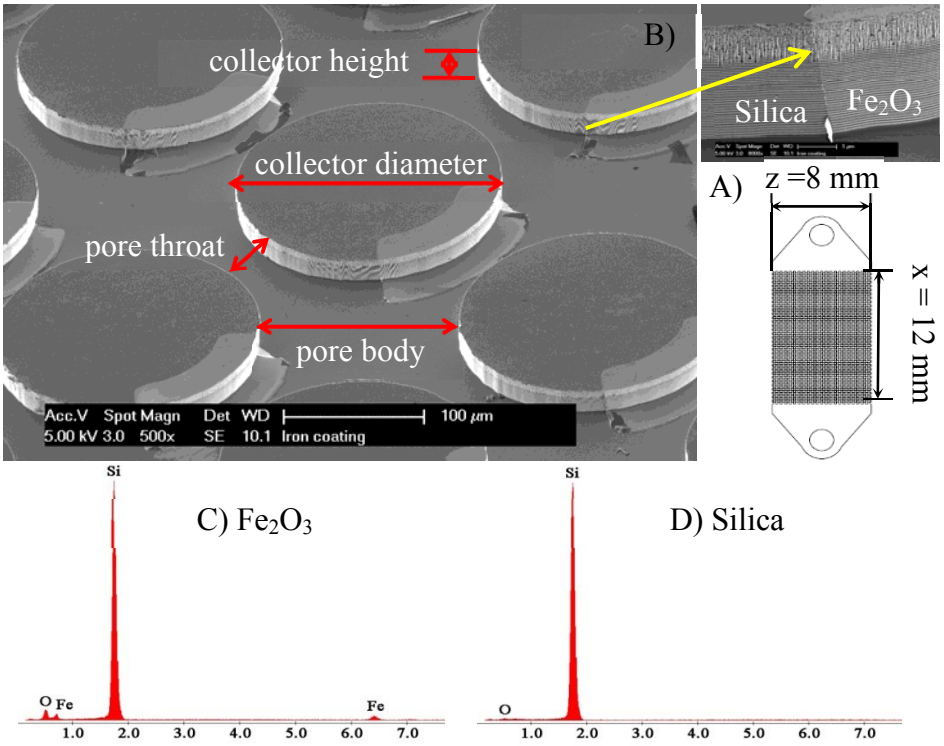

Figure 5.1 (A) Geometry of micromodel and (B) scanning electron microscopy (SEM) picture of the heterogeneous silica/ Fe_2O_3 collectors at Acc.V = 5 kV. Length of pore network: x = 12 mm, width of pore network: z = 8 mm, height of collector: 22-28 µm, collector diameter: 190 µm, pore space: 130 µm, and pore throat: 36.3 µm. Energy dispersive X-ray spectroscopy (EDS) spectrum of Fe_2O_3 (C) and silica (D) surfaces at Acc.V = 15 kV.

The pore network pattern and Fe_2O_3 coating pattern (Figure 5.3) were designed by AutoCAD (Autodesk) and transferred onto separate chrome masks (Fineline Imaging). The pore network pattern was etched into a silicon wafer following the procedures described in previous chapter.[7] Briefly, as shown in Figure 5.2A, the wafer was coated with a layer (8 µm thickness) of photoresist polymer (PR, AZ 4620, AZ Electronic Materials). Then pore network pattern on the mask was selectively exposed to ultraviolet (UV) light (EVGroup) for 25 s and the pattern was transferred to the wafer. PR exposed to UV light was removed by a PR developer (AZ 400K, AZ Electronic Materials) as shown in Figure 5.2B. The exposed area was etched to a depth around 25 µm using an inductively coupled plasma-deep reactive ion etching (ICP-DRIE) system (Plasmatherm). Then, the wafer was cleaned using a PR stripper (AZ 400 T, AZ Electronic Materials), acid solution (H_2SO_4: H_2O_2 = 3:1) and SC1 solution (deionized water: H_2O_2: NH_4OH

= 5:1:1) following our previous publication.[7] A layer of 0.15 µm silicon dioxide was created on the silica wafer by thermal dry oxidation at 1100 °C for 1.5 hr. The pore network of the micromodel is shown in Figure 5.2C.

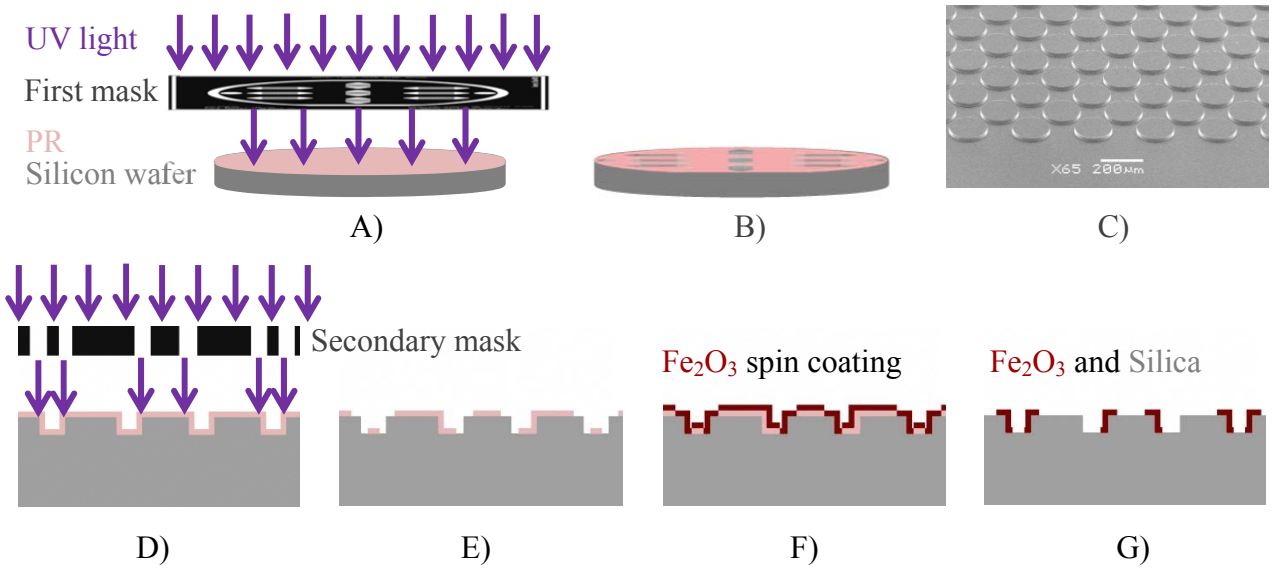

Figure 5.2 Micromodel fabrication procedure. Grey: silicon or silica surface, Pink: photoresist (PR), Black: mask, Violet: UV light, and Red: Fe_2O_3 surface. Graph (A) and (B) are an illustration of the whole silicon wafer which had 9 micromodels. Graph (C) is the SEM (Scanning Electron Microscopy) picture of the inlet area of one micromodel. Gragh (D), (E), (F) and (G) are the illustration of part of the pore network.

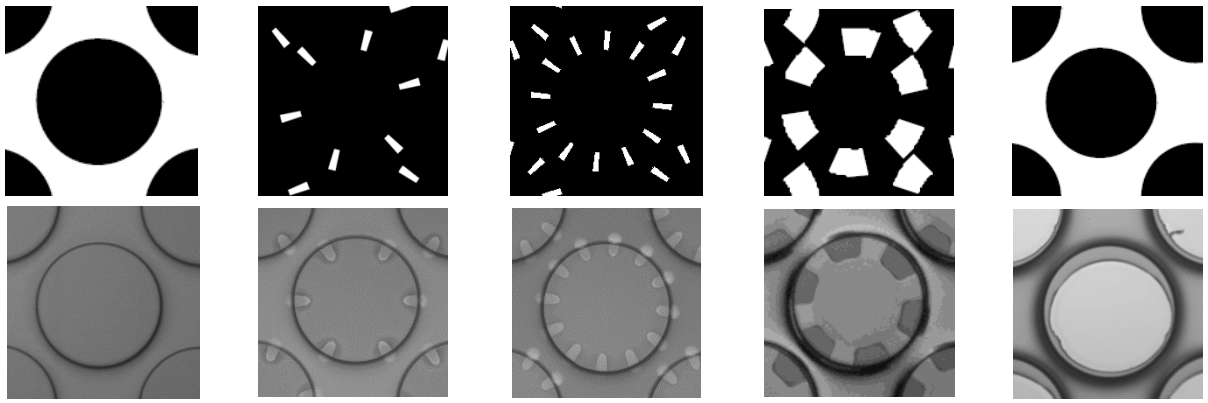

Figure 5.3 Illustration of the masks and collectors. Transparent area on the mask (A) was etched into the silica wafer. Transparent area on the mask (B), (C), (D) and (E) was coated with Fe_2O_3. The width of the Fe_2O_3 band was 9.9, 9.9 and 49.7 µm for collectors coated with 10 (B), 20 (C) and 50% (D) Fe_2O_3.

For micromodel without the Fe_2O_3 coating, the inlet and outlet (0.8 mm in diameter） of the micromodel were drilled using a micro press drill (Micro Drill Presses) equipped with a 1 inch diameter diamond plated drill (UKAM Industrial). After being cleaned with oxygen plasma (March Plasma System) and SC1 solution, the silica wafer was sealed with a glass wafer and cut into individual micromodel as described in a previous chapter.[7]

To fabricate wafer with a patchwise charge heterogeneous surface, the etched and oxidized wafer was coated with another layer (8 μm thickness) of PR (Figure 5.2D). Then a second mask (Figure 5.3) was applied to selectively expose the area, which was transparent on the second mask, that will be coated with Fe_2O_3 (expose under UV light for 50 s). Next, PR developer was used to remove UV light exposed PR on the wall of the cylindrical collectors from top to bottom, and an area adjacent to the collectors (Figure 5.2E). As shown in Figure 5.2F, the wafer was coated with 100 nm Fe_2O_3 (Kurt J Lesker, 99.9% Fe_2O_3) in a magnetron sputtering deposition system (Discovery 785, Denton Vacuum Inc.). The wafer was then cleaned with PR stripper to remove the PR and unwanted Fe_2O_3 (Figure 5.2G). At last, the wafer was drilled, cleaned, sealed and cut into individual micromodel as described above.

Scanning electron microscopy (SEM) was used to characterize the structure of silica and Fe_2O_3 surfaces on the collector. Full elemental spectra were required in 4.5 × 3 μm area at more than 10 locations on silica and Fe_2O_3 surfaces separately by energy dispersive X-ray spectroscopy (EDS, FEI XL30 ESEM-FEG microscopy) to test the quality of Fe_2O_3 coating. The SEM and EDS was operated at accelerating voltage (Acc.V) of 5.0 kV and 15.0 kV, respectively.

***C. parvum* Oocyst Preparation and Microspheres**. *C. parvum* oocysts (4-5 μm in diameter) were propagated using an infected male Holstein calf. The procedure was complied with protocols approved by the University of Illinois Institutional Animal Care and Use Committee. The feces was collected and oocysts were purified following previously published protocol.[9] A mixture of Hanks' balanced salt and antibiotic-antimycotic solution was used to store oocysts at 4°C. Fluoresbrite® YG Carboxylate Microspheres were purchased from Polysciences, Inc. (4.5 μm in diameter). Before use, the stock solution of oocysts and microspheres was removed by centrifugation (17000 × g for 2 min). The oocysts or microspheres then were washed twice with deionized water by centrifugation and re-suspended in the experimental electrolyte. A concentration range from 0.5×10^6 to 1.5×10^6 particles/mL was used in the experiment. A lower concentration was used in favorable conditions and a higher

concentration was used in unfavorable conditions. A hemacytometer (INCYTO, 22-600 series) was used to quantify particle concentration.

Fourier transform Infrared Spectroscopic (FT-IR) Imaging. Infrared spectroscopic imaging data were acquired using a Perkin Elmer Spotlight 400 imaging system (Perkin Elmer, Waltham, MA). FT-IR images were acquired in attenuated total reflectance (ATR) imaging modes with the ATR imaging adapter using a Germanium crystal. Data were collected over the nominal free-scanning spectral range and saved over 4000–750 cm^{-1}, and were recorded with an interferometer speed of 1.0 cm/s and collected using a linear mercuric cadmium telluride (MCT) detector array. Spectral images were acquired with a pixel size of 1.56 μm × 1.56 μm, with 4 scans per pixel at a spectral resolution of 4 cm^{-1}. ATR images were acquired across a 100 μm × 100 μm region of the ATR crystal. The ATR crystal was gently placed in contact with the sample using minimal pressure to ensure good contact and minimize sample damage. All data was then exported to the program ENVI/IDL and all further computation was performed using in-house written programs.

Surface Potential Measurement and DLVO Energy Profile. A Zetasizer Nano analyzer (Malvern Instruments) was used to measure the electrophoretic mobilities of oocysts, microspheres, and pulverized silica and Fe_2O_3 particles at 1 mM NaCl with a pH range from 3 to 10. Pulverized silica particles were prepared following procedures described in previous chapter.[7] Pulverized Fe_2O_3 particles were grounded from a piece of Fe_2O_3 source using an agate mortar. The electrophoretic mobilities were converted to zeta potential using Smoluchowski equation.

DLVO energy profiles for oocyst-silica, oocyst-Fe_2O_3, microsphere-silica, and microsphere-Fe_2O_3 systems were calculated from the electrostatic interaction model by Hogg et al.[24] and the retarded van der Waals interaction model by Gregory.[25] The equations and parameters used in our calculation are listed in previous publication.[5, 7] The Hamaker constant of oocyst-water-silica, oocyst-water-Fe_2O_3, microsphere-water-silica, and microsphere-water-Fe_2O_3 systems were 1.2×10^{-21}, 2.2×10^{-21}, 2.2×10^{-21}, and 4.0×10^{-21}, respectively (Table 5.1). The Hamaker constant of oocyst-water-silica system (1.2×10^{-21} J) was reported in our previous publication.[6] The Hamaker constant of oocyst-water-Fe_2O_3, carboxylate microsphere-water-silica and carboxylate microsphere-water-Fe_2O_3 systems was determined from Lifshitz-van der Waals (LW) component of surface energy (γ^{LW}) as described in the previous chapter.[6]

$$A = -12\pi y_0^2 \Delta G_{y0}^{LW} \tag{5.1}$$

$$\Delta G_{y0}^{LW} = 2\left(\gamma_l^{LW} - \gamma_s^{LW}\right)\left(\gamma_c^{LW} - \gamma_l^{LW}\right) \tag{5.2}$$

where y_0 is minimum equilibrium cut-off distance[26] that is usually assigned a value of 0.157 nm, ΔG_{y0}^{LW} is LW component of free energy of adhesion, γ_c^{LW} is γ^{LW} of oocysts or carboxylate microspheres, γ_l^{LW} is γ^{LW} of water and γ_s^{LW} is γ^{LW} of silica or Fe_2O_3.

Table 5.1 Surface energy ($\gamma^{LW}, \Delta G_{y0}^{LW}$) and Hamaker constant ($A$) in the presence of water at 20°C

	$\gamma^{LW}/\Delta G_{y0}{}^{LW}$ (mJ/m^2)	A(J)
Water	21.8 [a, c]	
Oocysts	26.9 [a, d]	
Carboxylate microspheres	31.4 [a, e]	
Silica (Quartz)	35.6 [a, d]	
Fe_2O_3 (Hematite)	48.5 [a, f]	
Oocyst-silica	-1.33 [b]	1.2×10^{-21}
Oocyst-Fe_2O_3	-2.16 [b]	2.2×10^{-21}
Carboxylate microsphere-silica	-2.42 [b]	2.2×10^{-21}
Carboxylate microsphere-Fe_2O_3	-3.92 [b]	4.0×10^{-21}

[a] γ^{LW}: LW component of surface tension
[b] $\Delta G_{y0}{}^{LW}$: LW component of free energy of adhesion per unit area
[c] Data from van Oss[26]
[d] Data from Liu et al.[6]
[e] Data from Janjaroen et al.[27]
[f] Data from Plaze et al.[28]

Micromodel Experiment. To investigate the influence of collector surface charge heterogeneity on oocyst and microsphere transport, transport experiments were conducted in micromodels coated with 0, 10, 20, 50 or 100% Fe_2O_3 in 1 mM NaCl at pH 4.4, 1 mM NaCl at pH 5.8 ± 0.1 or 1 mM $NaHCO_3$ at pH 8.1 ± 0.1. The details of experimental setup and calculation of particle attachment efficiencies (α) are described in the previous chapter.[7] Briefly, the micromodel was saturated with colloid free experimental electrolyte solution. Then an electrolyte solution with a colloid concentration range from 0.5×10^6 to 1.5×10^6 particle/mL was pumped into the micromodel at a constant flow rate, which maintained the linear velocity in the pore network at 1.86 mm/s. For microsphere transport, the microspheres attached on collectors were directly observed at 20 × magnification with a fluorescent microscope (Leica, DMI5000 M) and a FITC filter, recorded by a charge-coupled device (CCD) camera (Qimaging Retiga 2000R Fast 1394) and analyzed with Image Pro 7.0 software. For experiment with

oocysts, after a transport experiment, Crypt-a-Glo^{TM} (Waterborne, Inc.), a fluorescent antibody that specifically binds with oocyst surface protein, was pumped in the micromodel in the dark for 20 min. Then images of oocyst attachment were recorded with fluorescent microscopy. Oocysts or microspheres that attached to the 1838 collectors were determined by direct counting. Particles attached to silica or Fe_2O_3 surfaces were counted separately to determine the average single collector removal efficiency (η) for only Fe_2O_3 patches ($\eta_{Fe_2O_3}$), silica patches (η_{silica}) and for the entire collectors (η_{total}). The values of η were calculated as the ratios of the number of colloids attached to the collectors over the number of colloids approaching the collectors.[7, 13, 29] The average attachment efficiency (α) of colloids was determined by the ratio between the average single collector removal efficiencies for unfavorable conditions (η, particle attached on collectors coated with 0, 10, 20 or 50% Fe_2O_3) and for favorable conditions (η_0, particle attached on 100% Fe_2O_3 surface).

Confocal Microscopy Observation for selected Micromodel Experiment. Laser scanning confocal microscopy (Zeiss LSM 710 Upright) was used to observe the location of microspheres attached to a charge heterogeneous collector wall. After the transport experiment, the micromodel was sealed and carefully installed on a confocal microscope with an argon ion gas laser at 488 nm (FITC). The pinhole of 98.1, which resulted in 1.7 μm of optical section thickness, was set to eliminate light outside the focal plane. Grey-scale images were scanned with a 40 × magnification oil immersion objective every 1 μm from the bottom of the pore network to the top of the collectors. Each image was converted to a binary image by setting a threshold of 40 using ImageJ. In the binary image, pixels with a grey value above the threshold were marked as "object" pixels (fluorescent signal pixels of microsphere) and pixels with a grey value below the threshold were marked as "background" pixels. The total number of "object" pixels on all the pictures were summed up and divided by the total number of microspheres to determine the total pixels of a single microsphere. Then the number of "object" pixels on each binary image was normalized by the total pixels of a single microsphere to investigate the location of the attached microspheres on the collector wall.

Patchwise Geochemical Heterogeneity Model. The patchwise geochemical heterogeneity model[18, 30] was based on the assumptions that 1) each of the isolated patches is a homogeneous surface and can be distinguished on the basis of size, and 2) if the transition between two adjacent patches $\kappa R > 1$ (κ is the inverse Debye length and R is the size of the

patch), the interactions at patch boundaries can be neglected. In our charged heterogeneous micromodel, each of the isolated silica and Fe_2O_3 patches was homogeneous. The inverse Debye length at 1 mM ionic strength ($\kappa = 1.04 \times 10^8$ m^{-1}) and the smallest patch size ($R = 9.9 \times 10^{-5}$ m) resulted in a smallest transition of $\kappa R = 1 \times 10^4$, which was >>1. Therefore, the overall partial attachment efficiency on the charged heterogeneous surface can be described as follows:

$$\alpha = \lambda \alpha_{Fe_2O_3} + (1-\lambda)\alpha_{silica} \quad (1)$$

where λ is the fraction of Fe_2O_3 surface, $\alpha_{Fe_2O_3}$ is attachment efficiency on Fe_2O_3 surface and α_{silica} is attachment efficiency on silica surface.

5.4 Results and Discussion

Characterization of the Patchwise Charged Heterogeneous Collector. The SEM image of the charged heterogeneous collectors is shown in Figure 5.1. As shown in Figure 5.1B, the silica collector wall was coated with Fe_2O_3 (lighter area) and the coating area was completely coated with Fe_2O_3. Raman spectroscopy confirmed that the Fe_2O_3 layer was hematite (Figure 5.4).[31] More than 10 EDS spectra were required at different locations on Fe_2O_3 surface (Figure 5.1C). All spectra revealed the presence of Fe, O and Si, which confirmed the complete coverage of Fe_2O_3. The presence of Si was due to the presence of the silica substrate under the Fe_2O_3 surface. EDS spectra at more than 10 locations on silica surfaces (Figure 5.1D) illustrated no presence of Fe_2O_3, which indicated that the silica patches were not contaminated with Fe_2O_3.

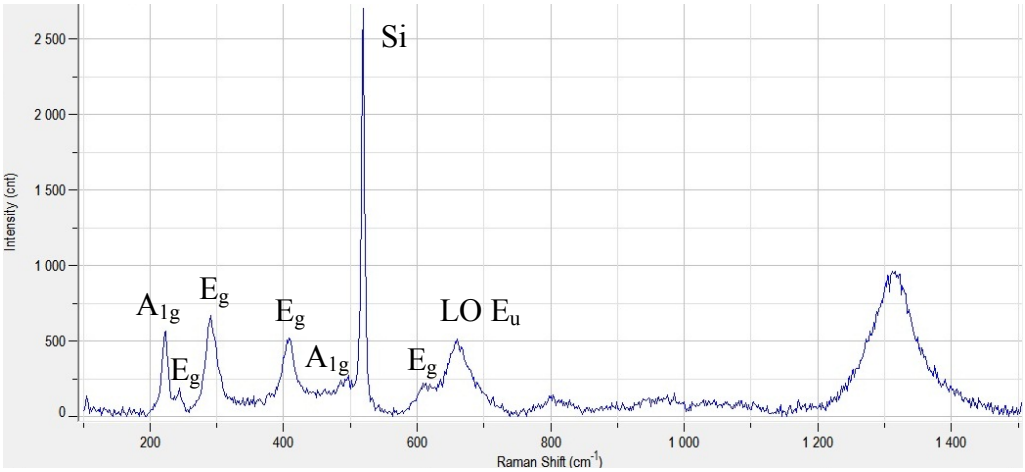

Figure 5.4. Raman spectra of thin Fe_2O_3 film coated on silica surface. Raman shift (cm^{-1}) assigned to hematite: 229 (A_{1g}), 249 (E_g), 295 (E_g), 414 (E_g), 500 (A_{1g}), 615 (E_g) and 660 (LO E_u)[31] and to silica: 520[32].

Characterization of Oocyst Surface. FT-IR spectra with a spatial resolution of 1.56 μm and a spectral resolution of 4 cm^{-1} were acquired in a 100 × 100 μm area to characterize oocyst surface functional groups and chemical heterogeneity. Two representative spectra of viable oocysts scanned at different locations are shown in Figure 5.5. The FT-IR spectra indicated the presence of amides (1638, 1544 and 1338 cm^{-1} for amide I, amide II and amide III, respectively), carboxylate (1400 cm^{-1} for COO^-), phosphate (1238 cm^{-1} for PO_2^-), and polysaccharide (1152 and 1078 cm^{-1} for sugar ring vibration and C-O-C, C-C) functional groups. These functionalities are consistent with similar spectra of oocyst surfaces that have been reported previously.[33, 34] Interestingly, an unknown peak at 1002 cm^{-1} was shown only in spectra b (Figure 5.5). This peak was observed in only a few of the many spectra acquired within the 100 × 100 μm. Three samples were scanned and we consistently observed the variation of the peak at 1002 cm^{-1} at different locations. The presence of multi-functional groups and the variation of FT-IR spectra measured at different location on oocyst surfaces could imply a degree of oocyst surface chemical heterogeneity, which would contribute to charge heterogeneity at the surface. As FT-IR imaging resolution is improved, characterization of surface chemical heterogeneity should become even more robust.

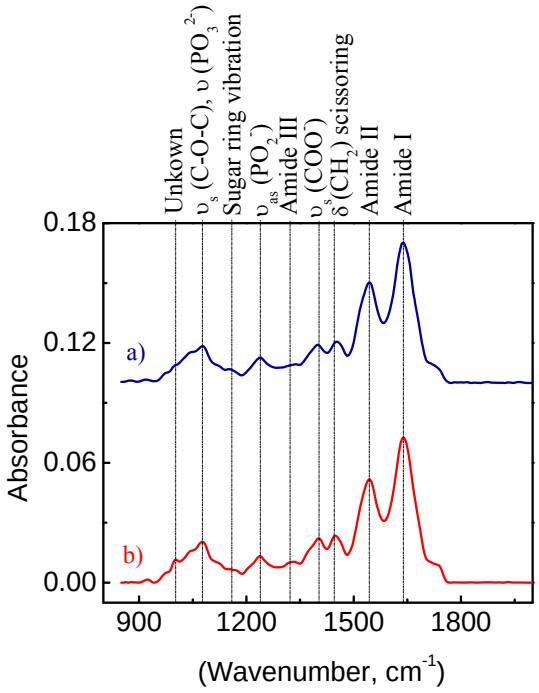

Figure 5.5 FT-IR spectra of viable oocyst suspension scanned at different locations in deionized water at pH 5.7-5.9. The deionized water background was subtracted from the spectra. Amide I: C=O, C-N, N-H, amide II: N-H, C-N and amide III: N-H, C-N, C-H, and N-H.

Electrokinetic Properties of Studied Surfaces. The zeta potentials of particle and collector surfaces in 1 mM NaCl solution at different pH is shown in Figure 5.6. Based on the zeta potential data, the isoelectric points of oocysts, microspheres, silica and Fe_2O_3 surfaces were determined to be approximately pH 3.8, 3.2, 4.0, and 6.7, respectively. It was reported that the isoelectric point of SiO_2 and synthetic hematite were pH 2.31-3.17[35] and pH 6.9, respectively.[36] Our measurement of isoelectric points of silica and Fe_2O_3 surfaces were comparable to the isoelectric points reported in the literature.

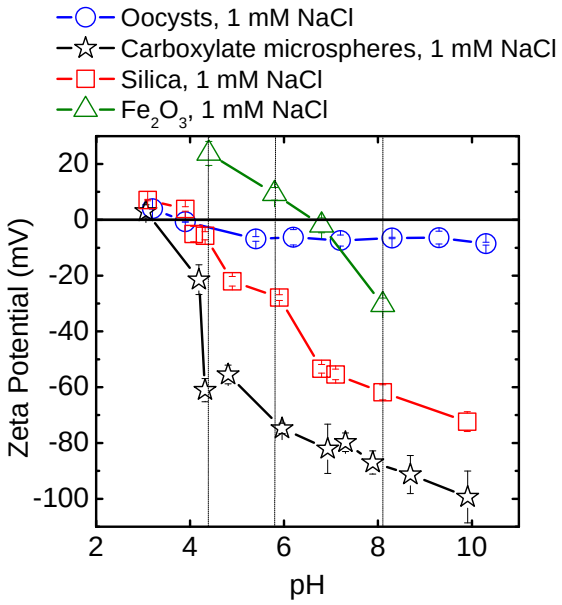

Figure 5.6 Zeta potential of oocysts, microspheres, and pulverized silica and Fe_2O_3 particles at 1 mM NaCl as a function of pH in 1 mM NaCl.

A 3-Dimensional Confocal Imaging for Carboxylate Microspheres Attached on Charged Heterogeneous Surface. The 3-dimensional confocal microscopy imaging (Figure 5.7A) of microspheres attached to silica collectors coated with 20% Fe_2O_3 in 1 mM NaCl at pH 7.1 ± 0.1 was shown to investigate the distribution of microspheres on collector wall. The geometry outline of the collector was drawn with Adobe Photoshop CS5 and is shown in Figure 5.7A. The shadow area on the collector wall was the Fe_2O_3 surface. As shown in Figure 5.7A, the majority of the particles were attached to Fe_2O_3 surface on the collector wall. The distribution of microspheres attached on the collector wall was determined by the fluorescent signal of 24 images taken every 1 μm from the bottom to the top, as shown in Figure 5.7B and 5.7C. The normalized fluorescent signal represented the abundance of microspheres attached on each layer. The sum of the fluorescent signal for the height below 5 μm, i.e. 20% of the total depth, was only

half of the signal from one microsphere. The fluorescent signal was highest at 8-12 μm from the bottom of the collector. Note that the middle of the collector was at 12 μm from the bottom of the collector. It was concluded that the majority of the microspheres were attached in the middle of the collector wall.

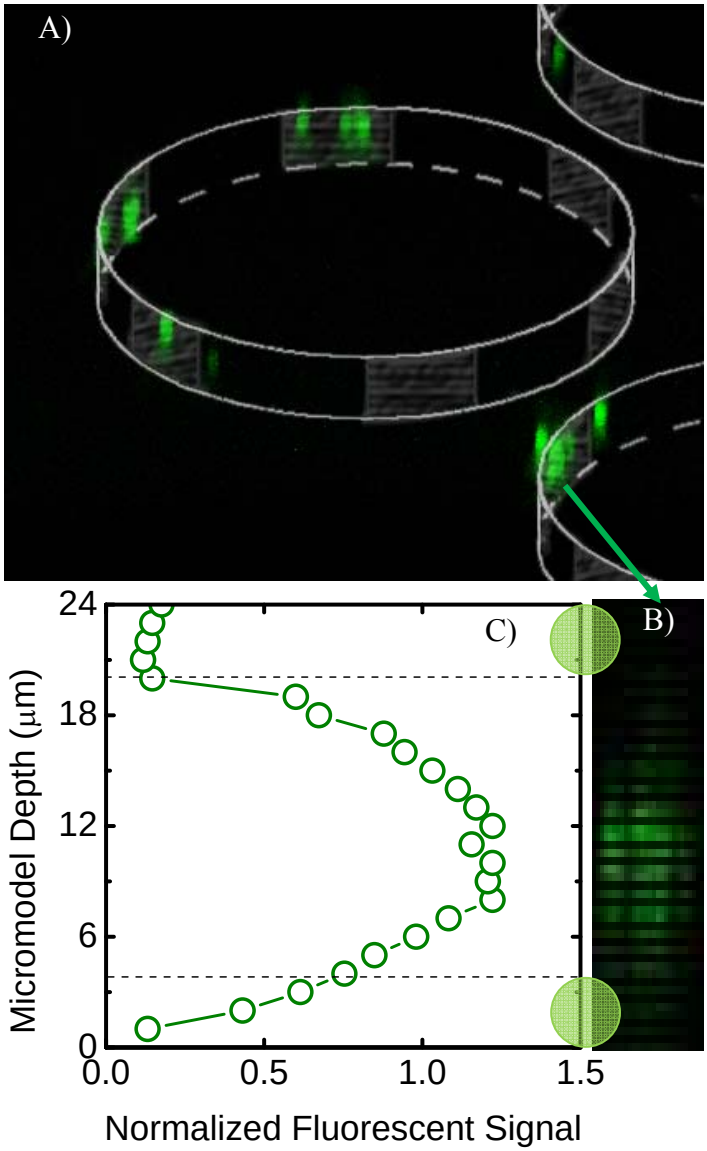

Figure 5.7 (A) A 3-dimensional reconstructed confocal microscopy image of attached microspheres on a silica collector coated with 20% Fe_2O_3. The geometry outline of the collector was drawn to illustrate the silica (transparent) and Fe_2O_3 (shadow) surfaces. (B) A side view of the confocal microscopy image of the attached microspheres on the collector wall. (C) The distribution of microsphere fluorescent signals in the collector depth. A micromodel depth of 0 was the heterogeneous silica/Fe_2O_3 surface and a depth of 24 was the Pyrex glass. The green spheres illustrate the size of the microspheres. Experimental solution chemistry: 1 mM NaCl, pH 7.1 ± 0.1, buffered with 0.05 mM $NaHCO_3$.

Oocyst and Carboxylate Microsphere Attachment on Charged Heterogeneous Surface. Attachment of oocysts and microspheres on charged heterogeneous collector at different pH are shown in Figure 5.8 and Figure 5.9, respectively. The average single collector removal efficiencies (η_{total}) for oocysts and microspheres on the entire collectors are shown in Figure 5.10. The values of DLVO energy barrier between colloid and collector surfaces calculated for different pH are shown in Table 5.2. In general, oocyst and microsphere attachment at the same pH increased with the percentage of Fe_2O_3 on the collector surfaces due to the presence or absence of a smaller energy barrier between the colloids and Fe_2O_3 surface as compared to energy barrier between the colloids and silica surface. Oocyst and microsphere attachment on the collectors coated with the same amount of Fe_2O_3 decreased with increasing pH due to an increasing energy barrier between the particle and silica surfaces (Table 5.2). For example, when the energy barrier between the microsphere and silica surface increased from 360 kT at pH 4.4 to 3500 kT at pH 5.8 to 15000 kT at 8.1, the η_{total} for microsphere on collectors coated with 10% Fe_2O_3 decreased from 3.7×10^{-3} to 2.8×10^{-4} to 3.9×10^{-5}.

On the silica collectors coated with 10% Fe_2O_3, more than 93% of oocysts attached onto Fe_2O_3 patches at pH 8.1 (Figure 5.8), while only 30-60% oocysts were attached on Fe_2O_3 patches at pH 5.8. Less than 80% of microspheres were attached to Fe_2O_3 patches even on the collectors coated with 50% Fe_2O_3 (Figure 5.9). The preference of oocysts for Fe_2O_3 patches was obvious at pH 8.1. In addition, as shown in Figure 5.10, for collectors coated entirely with Fe_2O_3, η_{total} for oocysts obtained at pH 8.1 was higher than that at pH 5.8 ($8.1 \times 10^{-3} \pm 1.4 \times 10^{-3}$ vs. $6.9 \times 10^{-3} \pm 1.8 \times 10^{-3}$). This observation contradicts the estimated higher DLVO energy barrier between oocyst and Fe_2O_3 surfaces at pH 8.1 compared to that at pH 5.8. Furthermore, the energy barrier and separation distance between oocyst and 100% Fe_2O_3 surface at pH 8.1 were similar to those between oocyst and silica surface at pH 5.8 (210 kT at 9 nm vs. 198 kT at 9 nm). However, η_{total} for 100% Fe_2O_3 surface at pH 8.1 was significantly higher than η_{total} for entire silica surface at pH 5.8 ($8.1 \pm 1.4 \times 10^{-3}$ vs. $2.5 \pm 0.7 \times 10^{-3}$). The discrepancies between experimental observation and DLVO theory could be contributed to surface complexation between oocyst and Fe_2O_3 surfaces suggested by Gao et al.[37] Their results suggested that monodentate complexes between carboxylate groups and Fe metal centers predominated oocyst-hematite complexes at low pH, whereas binuclear bidentate complexes became prevalent with higher pH. Because of the stronger binding between oocyst and Fe_2O_3 at pH 8.1, the average single collector removal

efficiency (η_{total}) for oocysts on Fe_2O_3 at pH 8.1 ($8.1 \pm 1.4 \times 10^{-3}$) was used as maximum average single collector removal efficiency (η_0) to calculate attachment efficiency (α) of oocyst attachment at pH 8.1.

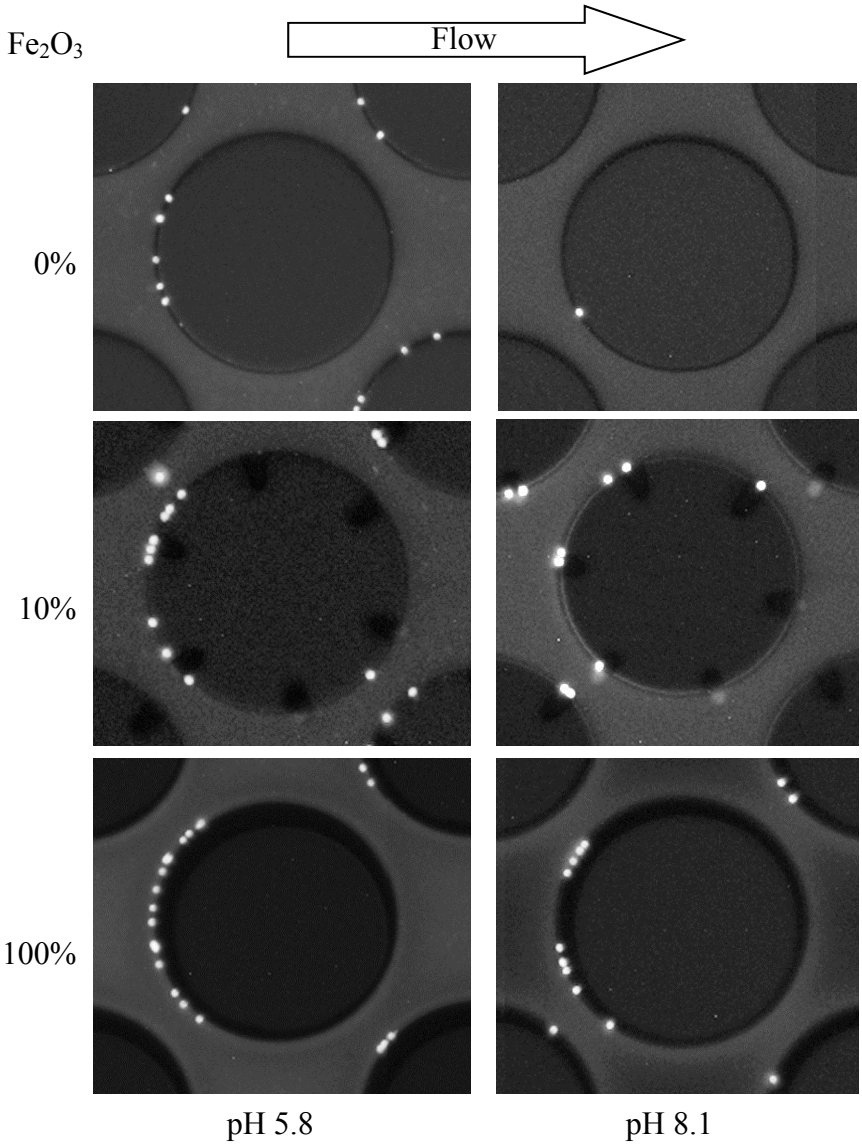

Figure 5.8 Attachment of oocysts on silica collectors coated with 0, 10 and 100% Fe_2O_3. Experimental solution chemistry: 1 mM NaCl at pH 5.8 or 1 mM $NaHCO_3$ at pH 8.1. Linear velocity = 1.86 mm/s.

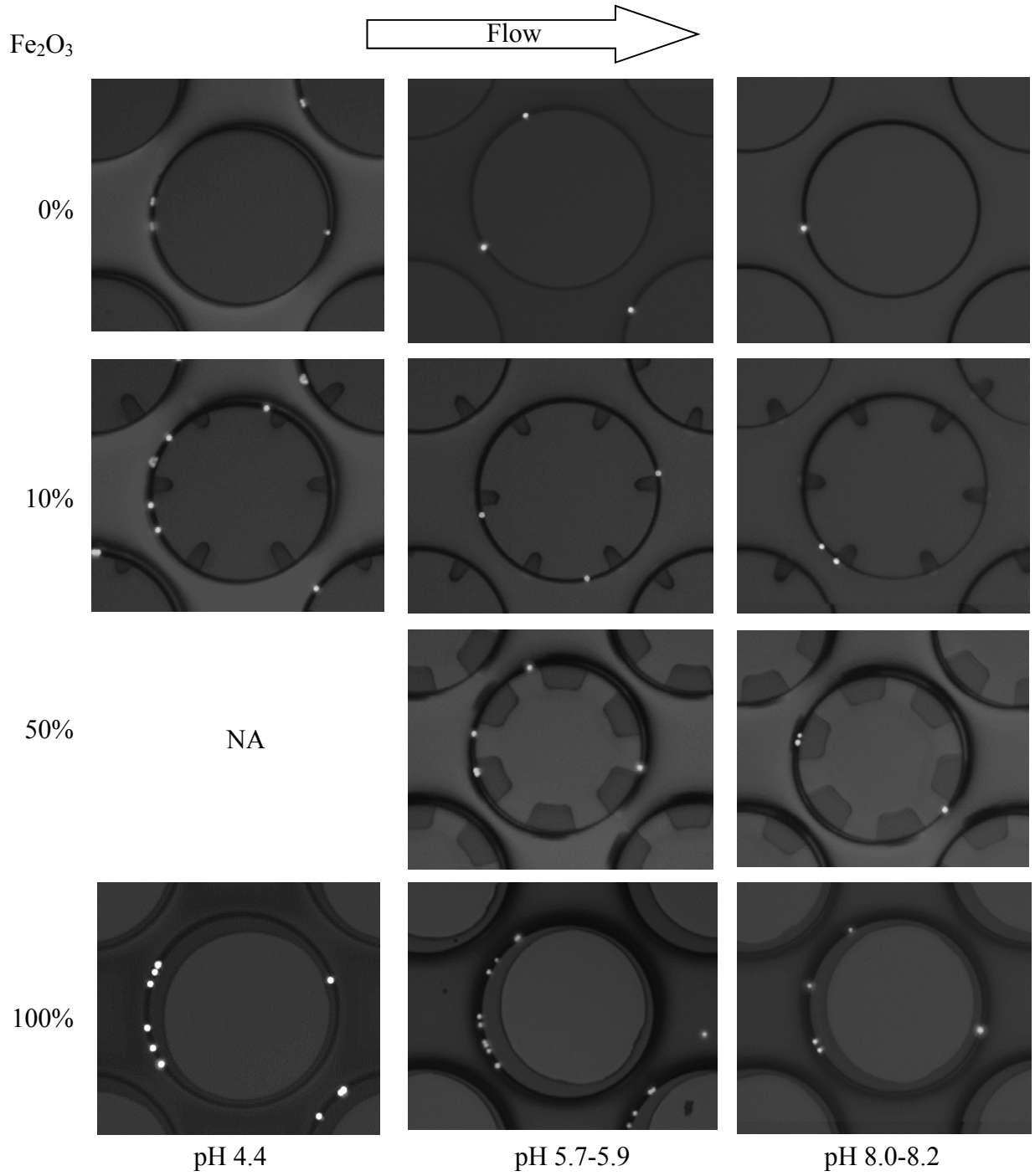

Figure 5.9 Attachment of carboxylate microspheres on silica collectors coated with 0, 10, 50 and 100% Fe_2O_3. Experimental solution chemistry: 1 mM NaCl at pH 4.4, 1 mM NaCl at pH 5.8 or 1 mM $NaHCO_3$ at pH 8.1. Linear velocity = 1.86 mm/s.

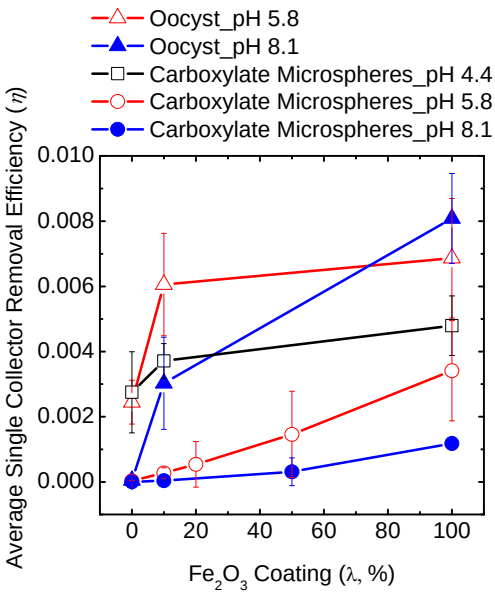

Figure 5.10 Average single collector removal efficiency (η_{total}) of oocysts (triangle) and carboxylate microspheres (square and circle) on silica collectors coated with 0, 10, 20, 50 and 100% Fe_2O_3. Experimental solution chemistry: 1 mM NaCl at pH 4.4 (black), 1 mM NaCl at pH 5.8 (red) or 1 mM $NaHCO_3$ at pH 8.1 (blue). Linear velocity = 1.86 mm/s.

Table 5.2. Values of DLVO energy barrier, separation distance of the energy barrier for oocysts and microspheres interacting with silica or Fe_2O_3 surfaces, and average single collector removal efficiencies (η) for oocysts and microspheres on entirely Fe_2O_3 surface, Fe_2O_3 patches, entirely silica surface or silica patches of charged heterogeneous collectors.

	pH	η_{total} on entirely Fe_2O_3 surface			$\eta_{Fe_2O_3}$ on Fe_2O_3 patches		
		Φ_T	H	$\lambda = 1$	$\lambda = 0.1$	$\lambda = 0.2$	$\lambda = 0.5$
Oocyst	5.8±0.1	-	-	$6.9\pm1.8\times10^{-3}$	$2.5\pm0.2\times10^{-2}$		
Oocyst	8.1±0.1	210	9	$8.1\pm1.4\times10^{-3}$	$2.9\pm1.4\times10^{-2}$		
Microsphere	4.4	-	-	$4.8\pm0.9\times10^{-3}$	$1.6\pm0.2\times10^{-2}$		
Microsphere	5.8±0.1	-	-	$3.4\pm1.5\times10^{-3}$	$1.2\pm0.4\times10^{-3}$	$1.1\pm0.1\times10^{-3}$	$2.0\pm1.9\times10^{-3}$
Microsphere	8.1±0.1	4200	5	$1.2\pm0.2\times10^{-3}$	$2.0\pm1.1\times10^{-4}$		$4.3\pm5.7\times10^{-4}$
	pH	η_{total} on entirely silica surface			$\eta_{Fe_2O_3}$ on silica patches		
		Φ_T	H	$\lambda = 0$	$\lambda = 0.1$	$\lambda = 0.2$	$\lambda = 0.5$
Oocyst	5.8±0.1	198	9	$2.5\pm0.7\times10^{-3}$	$4.0\pm1.9\times10^{-3}$		
Oocyst	8.1±0.1	222	15	$4.7\pm4.1\times10^{-5}$	$9.0\pm5.1\times10^{-5}$		
Microsphere	4.4	360	7	$2.8\pm1.2\times10^{-3}$	$2.3\pm0.3\times10^{-3}$		
Microsphere	5.8±0.1	3500	4	$3.4\pm1.5\times10^{-5}$	$1.8\pm1.6\times10^{-4}$	$3.9\pm5.8\times10^{-4}$	$8.9\pm7.3\times10^{-4}$
Microsphere	8.1±0.1	15000	1	$3.2\pm2.5\times10^{-6}$	$2.0\pm1.1\times10^{-5}$		$1.9\pm2.8\times10^{-4}$

Φ_T (kT): DLVO interaction energy barrier

H (nm): Separation distance of the maximum energy barrier between colloid and the collector surface

η: Average single collector removal efficiencies

λ: Fraction of Fe_2O_3 surface

At pH 8.1, above the isoelectric points for all studied surfaces, the energy barriers between microsphere and Fe_2O_3 surfaces were 4200 kT (Table 5.2). Due to the presence of the high energy barrier, η_{total} on 100% Fe_2O_3 surface at pH 5.8 ($3.4 \pm 1.5 \times 10^{-3}$) was used as the maximum average single collector removal efficiency (η_0) to calculate attachment efficiency (α) of microsphere attachment at pH 8.1. When there was no energy barrier between colloids and Fe_2O_3 surfaces at pH 4.4 and 5.8, the η_{total} on 100% Fe_2O_3 ($6.9 \pm 1.8 \times 10^{-3}$ for oocysts at pH 5.8, $4.8 \pm 0.9 \times 10^{-3}$ and $3.4 \pm 1.5 \times 10^{-3}$ for microspheres at pH 4.4 and pH 5.8, Table 5.2) was used as the maximum average single collector removal efficiency (η_0) to calculate attachment efficiency (α) at the same pH, respectively.

Comparison between Measured and Patchwise Geochemical Heterogeneity Model Predicted Attachment Efficiency. Oocyst and microsphere attachment efficiencies on charged heterogeneous surfaces at different pH were determined using silica micromodels coated with 0, 10, 20, 50 or 100% Fe_2O_3. The experimental data (symbols) was compared to attachment efficiencies predicted by patchwise geochemical heterogeneity model (dash lines) as shown in Figure 5.11. The fraction of Fe_2O_3 surface (λ) and experimental attachment efficiencies on entirely silica (α_{silica}) and entirely Fe_2O_3 ($\alpha_{Fe_2O_3}$) collectors were used to calculate the theoretical attachment efficiencies on charge heterogeneous collectors using equation 5.1. As shown in Figure 5.11A, the patchwise geochemical heterogeneity model significantly under-predicted oocyst attachment on charged heterogeneous collectors at pH 5.8 and 8.1. However, the model slightly over-predicted microsphere attachment on charged heterogeneous collectors at pH 5.8 and 8.1, where the DLVO energy barrier between microsphere and silica surfaces was more than one order of magnitude greater than that between oocyst and silica surfaces (Table 5.2 and Figure 5.11B). Interestingly, the patchwise geochemical heterogeneity model under-predicted microsphere attachment on charged heterogeneous collectors at pH 4.4, where the DLVO energy barrier between microsphere and silica (360 kT at 7 nm) was comparable with that between oocyst and silica surfaces at pH 5.8 and 8.1 (198 kT at 9 nm and 222 kT at 15 nm).

The over-prediction of particle attachment on charged heterogeneous surface by patchwise geochemical heterogeneous model was observed previously[22] and was explained by the "hydrodynamic bump" effect. As illustrated in Figure 5.11C, the hydrodynamic bump effect was related to the periodic favorable and unfavorable interaction between the colloids and the alternating charged heterogeneous patches on the collector surface. Elimelech et al.[22] suggested

that the repulsive interaction between the colloids and the unfavorable patches repelled the particles against the collector surface. As the colloids moved along the collector surface, the probability of colloid attachment on downstream favorable patches was reduced. Similarly, the attractive interaction between the colloids and the favorable patches would attract the colloids towards collector surface and increase the probability of colloid attachment on downstream unfavorable patches.

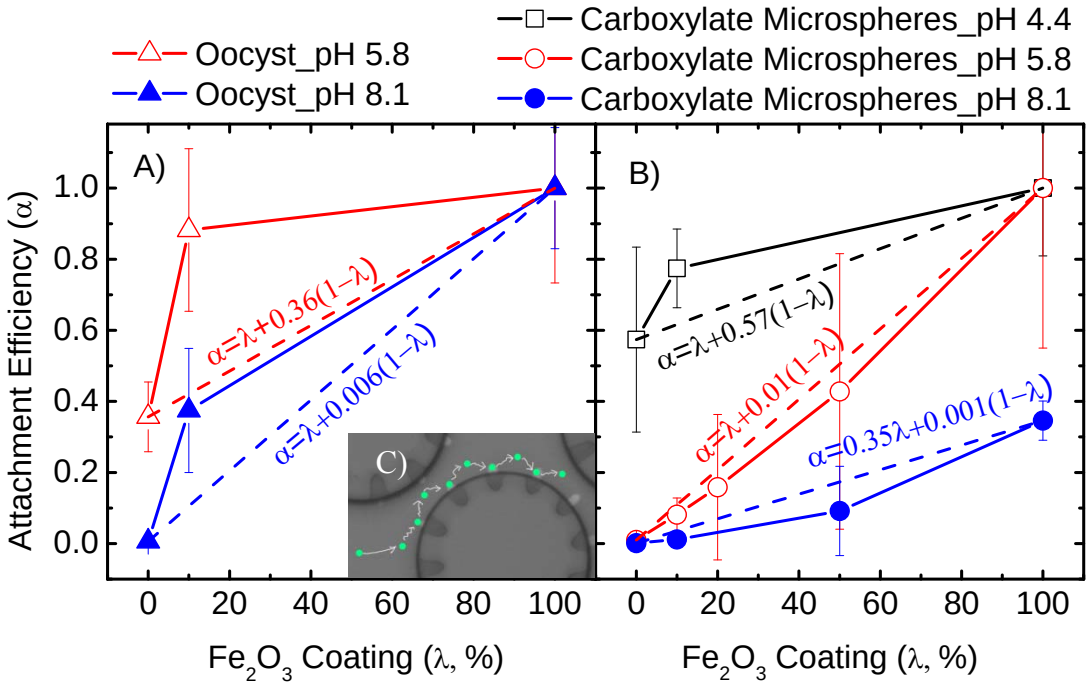

Figure 5.11. Attachment efficiency (α) of oocysts (A) and microspheres (B) on silica collectors coated with 0, 10, 20, 50 and 100% Fe_2O_3. (C) Illustration of "hydrodynamic bump" effect.[22] Experimental solution chemistry: 1 mM NaCl at pH 4.4 (black), 1 mM NaCl at pH 5.8 (red) or 1 mM $NaHCO_3$ at pH 8.1 (blue). Linear velocity = 1.86 mm/s.

We hypothesize that the "hydrodynamic bump" effect also influences colloid transport in the micromodel with patchwise charged heterogeneous collectors, where there were significantly different unfavorable interactions. For example, when the energy barriers between the microsphere and the silica or Fe_2O_3 surface at pH 8.1 were 15000 kT and 4200 kT, respectively, we expect that the presence of a very high energy barrier between the microsphere and silica patches would prevent the colloids from approaching the downstream Fe_2O_3 patches. As a result, η_{total} obtained for microspheres and collectors coated entirely with Fe_2O_3 should be higher than $\eta_{Fe_2O_3}$ for the microsphere attachment on Fe_2O_3 patches of collectors partially coated with Fe_2O_3.

In agreement with the "hydrodynamic bump" effect, at pH 5.8 and 8.1 η_{total} obtained for microsphere attachment on collectors coated entirely with Fe_2O_3 were higher than $\eta_{Fe_2O_3}$ for the microsphere attachment on collectors coated with 10% Fe_2O_3 ($3.4 \pm 1.5 \times 10^{-3}$ vs. $1.2 \pm 0.4 \times 10^{-3}$ at pH 5.8 and $1.2 \pm 0.2 \times 10^{-3}$ vs. $2.0 \pm 1.1 \times 10^{-4}$ at pH 8.1). Because the patchwise model ignores the spatial distribution of charged heterogeneous patches, the model over-predicted the attachment.

However, when the DLVO energy barrier was small, the "hydrodynamic bump" effect was diminished. For example, energy barriers of less than 360 kT were observed for microsphere and silica surfaces at pH 4.4, and for oocyst and silica surfaces at pH 5.8 and 8.1. As shown in Table 5.2, at pH 5.8 and 8.1 for oocysts and pH 4.4 for microspheres, there was a lower η_{total} obtained for collectors coated entirely with Fe_2O_3 than $\eta_{Fe_2O_3}$ for the colloid attachment on collectors coated with 10% Fe_2O_3 ($6.9 \pm 1.8 \times 10^{-3}$ vs. $2.5 \pm 0.2 \times 10^{-2}$ for oocysts at pH 5.8, $8.1 \pm 1.4 \times 10^{-3}$ vs. $2.9 \pm 1.4 \times 10^{-2}$ for oocysts at pH 8.1 and $4.8 \pm 0.9 \times 10^{-3}$ vs. $1.6 \pm 0.2 \times 10^{-2}$ for microspheres at pH 4.4). The increased attachment on Fe_2O_3 patches compared to 100% Fe_2O_3 surface led to an under-prediction of attachment by the patchwise model. Chatterjee et al.[21] used an Eulerian model to simulate particle transport on patchwise charged heterogeneous collectors with a low energy barrier (340 kT at 3 nm). Their model predicted higher particle attachment on charged heterogeneous collector than the patchwise geochemical heterogeneous model did. The authors also noticed significant higher local attachment rates at favorable patches compared to that on a homogeneous favorable surface due to local particle concentration accumulation at the leading edge of the favorable patches caused by the periodic electrostatic interactions. In addition, Abudalo et al.[8] also reported an under-prediction of the patchwise geochemical heterogeneity model for oocyst attachment in charged heterogeneous column.

5.5 Environmental Implications

As shown in Figure 5.11, a small fraction of Fe_2O_3 on patchwise charged heterogeneous collector significantly enhanced oocyst attachment. The results indicate that with the same amount of positively charged surface, the patchwise charged heterogeneous collectors are expected to remove more pathogens than a mixture of positively and negatively charged collectors.

Furthermore, $\eta_{Fe_2O_3}$ for oocysts on charged heterogeneous collectors was even higher than η_{total} for oocyst on 100% Fe_2O_3 collectors. The difference between colloid attachment on 100% Fe_2O_3 surface and Fe_2O_3 patches of patchwise charged heterogeneous collectors implies the importance of periodic electrostatic interactions in colloid transport on charged heterogeneous surface. When a porous media surface has microscopic-scale charge heterogeneity, it is essential to consider spatial distribution of charged heterogeneous patches in the transport model.

Acknowledgements. This work was supported by the National Science Foundation (NSF, CTS-0120978), NSF Career grant #0954501. Partial financial support for CYZ and DHH was provided by the Environmental Molecular Sciences Laboratory (EMSL), a national scientific user facility sponsored by the DOE, Office of Biological and Environmental Research and located at PNNL.

5.6 References

1. Corso, P. S.; Kramer, M. H.; Blair, K. A.; Addiss, D. G.; Davis, J. P.; Haddix, A. C. Cost of illness in the 1993 waterborne *Cryptosporidium* outbreak, Milwaukee, Wisconsin. *Emerging Infectious Diseases* **2003,** *9* (4), 426-431.

2. Fong, T. T.; Mansfield, L. S.; Wilson, D. L.; Schwab, D. J.; Molloy, S. L.; Rose, J. B. Massive microbiological groundwater contamination associated with a waterborne outbreak in Lake Erie, South Bass Island, Ohio. *Environmental Health Perspectives* **2007,** *115* (6), 856-864.

3. Gallay, A.; De Valk, H.; Cournot, M.; Ladeuil, B.; Hemery, C.; Castor, C.; Bon, F.; Megraud, F.; Le Cann, P.; Desenclos, J. C. A large multi-pathogen waterborne community outbreak linked to faecal contamination of a groundwater system, France, 2000. *Clinical Microbiology and Infection* **2006,** *12* (6), 561-570.

4. Agency, U. S. E. P., National Primary Drinking Water Regulations. In 2009; Vol. EPA 816-F-09-0004.

5. Liu, Y.; Janjaroen, D.; Kuhlenschmidt, M. S.; Kuhlenschmidt, T. B.; Nguyen, T. H. Deposition of *Cryptosporidium parvum* oocysts on natural organic matter surfaces: microscopic evidence for secondary minimum deposition in a radial stagnation point flow cell. *Langmuir* **2009,** *25* (3), 1594-1605.

6. Liu, Y.; Kuhlenschmidt, M. S.; Kuhlenschmidt, T. B.; Nguyen, T. H. Composition and conformation of *Cryptosporidium parvum* oocyst wall surface macromolecules and their effect on adhesion kinetics of oocysts on quartz surface. *Biomacromolecules* **2010,** *11* (8), 2109-2115.

7. Liu, Y.; Zhang, C.; Hilpert, M.; Kuhlenschmidt, M. S.; Kuhlenschmidt, T. B.; Nguyen, T. H. Transport of *Cryptosporidium* parvum oocysts in a silicon micromodel. *Environmental Science & Technology* **2012,** *46* (3), 1471-1479.

8. Abudalo, R. A.; Bogatsu, Y. G.; Ryan, J. N.; Harvey, R. W.; Metge, D. W.; Elimelech, M. Effect of ferric oxyhydroxide grain coatings on the transport of bacteriophage PRD1 and *Cryptosporidium parvum* oocysts in saturated porous media. *Environmental Science & Technology* **2005,** *39* (17), 6412-6419.

9. Johnson, J. K.; Schmidt, J.; Gelberg, H. B.; Kuhlenschmidt, M. S. Microbial adhesion of *Cryptosporidium parvum* sporozoites: Purification of an inhibitory lipid from bovine mucosa. *Journal of Parasitology* **2004,** *90* (5), 980-990.

10. Hijnen, W. A. M.; Brouwer-Hanzens, A. J.; Charles, K. J.; Medema, G. J. Transport of MS2 phage, *Escherichia coli*, *Clostridium perfringens*, *Cryptosporidium parvum* and *Giardia intestinalis* in a gravel and a sandy soil. *Environmental Science & Technology* **2005,** *39* (20), 7860-7868.

11. Tufenkji, N.; Dixon, D. R.; Considine, R.; Drummond, C. J. Multi-scale *Cryptosporidium*/sand interactions in water treatment. *Water Research* **2006,** *40* (18), 3315-3331.

12. Tufenkji, N.; Elimelech, M. Spatial distributions of *Cryptosporidium oocysts* in porous media: Evidence for dual mode deposition. *Environmental Science & Technology* **2005,** *39* (10), 3620-3629.

13. Tufenkji, N.; Miller, G. F.; Ryan, J. N.; Harvey, R. W.; Elimelech, M. Transport of *Cryptosporidium oocysts* in porous media: Role of straining and physicochemical filtration. *Environmental Science & Technology* **2004,** *38* (22), 5932-5938.

14. Johnson, P. R.; Sun, N.; Elimelech, M. Colloid transport in geochemically heterogeneous porous media: modeling and measurements. *Environmental Science & Technology* **1996,** *30* (11), 3284-3293.

15. Coston, J. A.; Fuller, C. C.; Davis, J. A. Pb^{2+} and Zn^{2+} adsorption by a natural aluminum- and iron-bearing surface coating on an aquifer sand. *Geochimica et Cosmochimica Acta* **1995,** *59* (17), 3535-3547.

16. Nordstrom, D. K.; Alpers, C. N.; Coston, J. A.; Taylor, H. E.; McCleskey, R. B.; Ball, J. W.; Ogle, S.; Cotsifas, J. S.; Davis, J. A. *Geochemistry, toxicity, and sorption properties of contaminated sediments and pore waters from two reservoirs receiving acid mine drainage*; Highlights of 99-4018A; United States Geological Survey Staff -- Published Research: March 8-12, 1999.

17. Cortis, A.; Harter, T.; Hou, L.; Atwill, E. R.; Packman, A. I.; Green, P. G. Transport of *Cryptosporidium parvum* in porous media: Long-term elution experiments and continuous time random walk filtration modeling. *Water Resources Research* **2006,** *42* (12), W12S13.

18. Song, L.; Johnson, P. R.; Elimelech, M. Kinetics of colloid deposition onto heterogeneously charged surfaces in porous media. *Environmental Science & Technology* **1994,** *28* (6), 1164-1171.

19. Elimelech, M.; Nagai, M.; Ko, C.-H.; Ryan, J. N. Relative insignificance of mineral grain zeta potential to colloid transport in geochemically heterogeneous porous media. *Environmental Science & Technology* **2000,** *34* (11), 2143-2148.

20. Ryan, J. N.; Elimelech, M.; Ard, R. A.; Harvey, R. W.; Johnson, P. R. Bacteriophage PRD1 and silica colloid transport and recovery in an iron oxide-coated sand aquifer. *Environmental Science & Technology* **1999,** *33* (1), 63-73.

21. Chatterjee, R.; Mitra, S. K.; Bhattacharjee, S. Particle deposition onto janus and patchy spherical collectors. *Langmuir* **2011,** *27* (14), 8787-8797.

22. Elimelech, M.; Chen, J. Y.; Kuznar, Z. A. Particle deposition onto solid surfaces with micropatterned charge heterogeneity: the “hydrodynamic bump” effect. *Langmuir* **2003,** *19* (17), 6594-6597.

23. Nazemifard, N.; Masliyah, J. H.; Bhattacharjee, S. Particle deposition onto charge heterogeneous surfaces: convection−diffusion−migration model. *Langmuir* **2006,** *22* (24), 9879-9893.

24. Hogg, R.; Healy, T. W.; Fuerstenau, D. W. Mutual coagulation of colloidal dispersions. *Transactions of the Faraday Society* **1965,** *62*, 1638-1651.

25. Gregory, J. Approximate expressions for retarded van der waals interaction. *J. Colloid Interface Sci.* **1981,** *83* (1), 138-145.

26. van Oss, C. J. Acid--base interfacial interactions in aqueous media. *Colloids and Surfaces a-Physicochemical and Engineering Aspects* **1993,** *78*, 1-49.

27. Janjaroen, D.; Ling, F.; Monroy, G.; Derlon, N.; Mogenroth, E.; Boppart, S. A.; Liu, W.-T.; Nguyen, T. H. Roles of ionic strength and biofilm roughness on deposition kinetics of *Escherichia coli* onto groundwater biofilm grown on PVC surfaces. *Water Research* **2012,** *Submitted*.

28. Plaza, R. C.; Zurita, L.; Durán, J. D. G.; González-Caballero, F.; Delgado, A. V. Surface thermodynamics of hematite/yttrium oxide core−shell colloidal particles. *Langmuir* **1998,** *14* (24), 6850-6854.

29. Auset, M.; Keller, A. A. Pore-scale visualization of colloid straining and filtration in saturated porous media using micromodels. *Water Resources Research* **2006,** *42* (12).

30. Gibb, A. W. M.; Koopal, L. K. Electrochemistry of a model for patchwise heterogeneous surfaces: The rutile-hematite system. *J. Colloid Interface Sci.* **1990,** *134* (1), 122-138.

31. Jubb, A. M.; Allen, H. C. Vibrational spectroscopic characterization of hematite, maghemite, and magnetite thin films produced by vapor deposition. *ACS Applied Materials & Interfaces* **2010,** *2* (10), 2804-2812.

32. Piscanec, S.; Ferrari, A. C.; Cantoro, M.; Hofmann, S.; Zapien, J. A.; Lifshitz, Y.; Lee, S. T.; Robertson, J. Raman spectrum of silicon nanowires. *Materials Science and Engineering C* **2003,** *23*, 931-934.

33. Gao, X.; Chorover, J. In-situ monitoring of *Cryptosporidium parvum* oocyst surface adhesion using ATR-FTIR spectroscopy. *Colloids and Surfaces B: Biointerfaces* **2009,** *71* (2), 169-176.

34. Gao, X.; Chorover, J. Amphiphile disruption of pathogen attachment at the hematite (α-Fe_2O_3)−water interface. *Langmuir* **2011,** *27* (10), 5936-5943.

35. Kosmulski, M., *Chemical properties of material surfaces*. CRC Press: 2001.

36. Gutierrez, L.; Li, X.; Wang, J.; Nangmenyi, G.; Economy, J.; Kuhlenschmidt, T. B.; Kuhlenschmidt, M. S.; Nguyen, T. H. Adsorption of rotavirus and bacteriophage MS2 using glass fiber coated with hematite nanoparticles. *Water Research* **2009,** *43* (20), 5198-5208.

37. Gao, X.; Metge, D. W.; Ray, C.; Harvey, R. W.; Chorover, J. Surface complexation of carboxylate adheres *Cryptosporidium parvum* Öocysts to the hematite−water interface. *Environmental Science & Technology* **2009,** *43* (19), 7423-7429.

CHAPTER 6

CONCLUSIONS

6.1 Conclusion

RSPF cell was used to investigate *Cryptosporidium parvum* oocysts deposition on quartz and NOM surfaces under a wide range of ionic strength. Oocyst attachment efficiency increased with ionic strength indicating that electrostatic interaction and van der Walls interaction controlled oocyst deposition. Microscopic evidence showed that oocyst entrapped in DLVO secondary minimum at 10 mM ionic strength was reversible. Some oocysts were resuspended and others were transfer to primary minimum and deposited irreversibly. However, oocyst attachment efficiencies were higher than zero at ionic strength below critical deposition concentrations (CDCs) predicted by DLVO theory. This was contributed to oocyst surface charge heterogeneity. Oocyst attachment efficiencies were lower than one at ionic strength above DLVO-predicted CDCs, where no DLVO energy barrier existed. In addition, the oocyst electrophoretic mobilities at different ionic strength were analyzed using Ohshima's theory. Ohshima's model assumes that a soft surface is composed of a hard core and an ion-penertrable polyelectrolyte layer. With this model, it is possible to quantify the surface "electrophoretic softness", i.e. $1/\lambda \sim \left(a_p N_p\right)^{-1/2}$, which indicated the the equivalent sphere radius of the polymer segment (a_p) and the density (N_p) of the polymer segment of ocoyst surface macromolecules in the polyelectrolyte layer. The simulated electrophoretic softness was significantly higher than hard particles such as quartz. These phenomena illustrated that oocyst had a "soft" layer of ion-penetrable surface polyelectrolytes which prevented oocyst deposition.

To investigate the role of this "soft" layer on oocyst attachment mechanisms, oocyst surface macromolecules were modified with proteinase K and mixed glycosidases. Surface potential, electrophoretic softness, contact angle, and polarity of untreated and proteinase modified oocysts were characterized. Proteinase K modification decreased oocyst surface potential and increased oocyst surface electrophoretic softness 10 times which suggested lower concentration of glycocalyx within the "soft" layer. Hamaker constant between proteinase K modified oocysts and quartz surface was calculated from contact angle and was 100 times

smaller than that between untreated oocysts and quartz surface. This change of surface properties due to proteinase K modification made oocyst barely deposited on quartz surface under the ionic strength we studied, i.e. 3 mM to 200 mM NaCl. The results indicated that the composition and conformation of oocyst surface macromolecules determined surface electrophoretic properties, i.e. surface potential and electrophoretic softness, and van der Waals interaction, which dominate oocyst deposition.

A 2-D micromodel was developed to conduct real time observation of oocyst transport in porous media and to study the influence of collector charge heterogeneity on oocyst transport. Distribution of attached oocysts in micromodel was correlated to local flow rate. Detachment of oocysts at lower ionic strength or higher pH after attachment experiments in silica micromodel confirmed the revisable entrapment of oocysts in secondary minimum energy well and reemphasized the importance of charge heterogeneity. Fourier transform Infrared Spectroscopic (FT-IR) imaging showed that oocyst surface had a degree of chemical heterogeneity. However, the resolution of FT-IR was not high enough to quantify oocyst surface heterogeneity. Thus, the influence of collector charge heterogeneity on oocyst transport was studied instead. The results showed that a small portion of Fe_2O_3 increased oocyst attachment significantly. Oocyst attached more on Fe_2O_3 surface at pH 8.1than at pH 5.8, which was contradicted to DLVO prediction and indicated different complexations formed between oocyst carboxylate groups and Fe metal centers on Fe_2O_3 surfaces at different pH conditions. Interestingly, the single collector removal efficiency on a Fe_2O_3 patch of a charged heterogeneous collector was 2-3 times higher than that on 100% Fe_2O_3 surface. This indicated a unique effect of periodic electrostatic interactions caused by alternating charged heterogeneous patches.

6.2 Contribution

This research firstly developed a method that can precisely design microscopic-scale patchwise charged heterogeneous collectors in a pore network. Micromodel was a promising and powerful tool to study colloid transport in complex yet well-defined conditions. The results of this research showed that local flow rate and local charge heterogeneity play important role in oocyst transport and need to be considered in transport model.

In addition, this research systematically studied oocyst surface macromolecules, characterized surface properties of oocyst and collector surface, and successfully related those surface properties to attachment mechanisms including charge heterogeneity, van der Waals interaction, and steric repulsion. Especially, this research systematically showed the importance of surface interactions and complexations between oocyst and quartz, NOM, Fe_2O_3 and charged heterogeneous mineral surfaces on oocyst transport. Importantly, this research firstly revealed that the electrophoretic softness of oocyst surface macromolecules was related to van der Waals interaction and steric repulsion between oocyst and collector surfaces.

Last but not the least, this research compared oocyst and microsphere attachment under a wide range of conditions, which include attachment on quartz surface, on Fe_2O_3 surface, on charged heterogeneous mineral surface, on NOM surface, at different pH and ionic strength, and at similar DLVO energy barrier. In general, oocyst attachment was higher than microsphere attachment. The results illustrated that microspheres is a conservative surrogate for oocysts to study oocyst transport.

With the conclusion from this research, a small fraction of positively charged surface in the filter will enhance oocyst removal significantly. Given the same amount of positively charged surface, the patchwise charged heterogeneous collectors will perform better than a mixture of positively and negatively charged collectors. Furthermore, decreasing ionic strength released a small portion of attached oocysts on collectors, while increasing pH released significant amount of attached oocysts on collectors. The filter may function well when the ionic strength of the influent varies but it may fail when the pH varies.

6.3 Future Prospects

This research introduced micromodel as a powerful tool to conduct real time observation of oocyst transport. With this technique, it is possible to design collectors in different shapes, sizes, pore network structures, surface chemicals, and even a combination of these parameters to study oocyst transport in simulated soil environment.

This research quantified the effect of collector surface charge heterogeneity. It is a challenge to quantify oocyst surface charge heterogeneity and its influence on oocyst transport

due to lacking of surface characterization techniques. With the improving of FT-IR imaging and AFM, it is promising to quantify the effect of colloid surface charge heterogeneity.

Another two challenges are to quantify the influence of steric repulsion and physical heterogeneity on oocyst transport. Manipulating the polymer length on microspheres and study their transport may help quantifying the influence of steric repulsion. Fabricating micromodel with different physical heterogeneity is promising to study the effect of physical heterogeneity.

This research showed surface interaction and complexations between oocyst and collector surface were important in oocyst transport. A systematically summary of surface interactions and complexations between oocyst and inorganic or organic surfaces in the subsurface at different solution chemistry is necessary to thoroughly understand oocyst transport.